AUTOMATIC VISUAL RECOGNITION OF BIOLOGICAL PARTICLES

RELATORE: Ch.mo Prof. Ruggero Frezza
Università degli Studi di Padova

CORRELATORE: Ch.mo Prof. Pietro Perona
California Institute of Technology

LAUREANDO: Marc'Aurelio Ranzato

A.A. 2002-2003

UNIVERSITÀ DEGLI STUDI DI PADOVA
DIPARTIMENTO DI INGEGNERIA DELL'INFORMAZIONE
TESI DI LAUREA

AUTOMATIC VISUAL RECOGNITION OF BIOLOGICAL PARTICLES

RELATORE: Ch.mo Prof. Ruggero Frezza
Università degli Studi di Padova

CORRELATORE: Prof. Pietro Perona
California Institute of Technology

LAUREANDO: Marc'Aurelio Ranzato

Padova, 6 aprile 2004

Sommario

Il riconoscimento automatico di corpuscoli tramite l'analisi di immagini trova applicazione in svariati settori come in: aerobiologia, biomedica, geologia, analisi della qualità del prodotto nell'industria. In particolare, questa tesi si focalizza sullo studio di sistemi automatici per il riconoscimento visivo di due tipi di particelle biologiche: corpuscoli che si trovano nelle urine e pollini diffusi nell'aria.

L'analisi microscopica manuale si dimostra spesso inadeguata perché lenta, costosa, imprecisa e non standardizzata. È quindi di interesse lo studio di sistemi automatici per analisi di immagini acquisite al microscopio e, più in generale, il riconoscimento di oggetti in immagini a basso contrasto e risoluzione.

Nel caso delle analisi delle urine, utili per rilevare malattie del tratto urinario e per identificare alcune forme di diabete che non provocano alcun dolore, esistono già alcuni sistemi automatici di analisi. Tuttavia, le loro performance e affidabilità sono suscettibili di un sostanziale miglioramento. Il database a disposizione contiene esemplari di corpuscoli suddivisi in 12 famiglie. La risoluzione di queste immagini varia da 36x36 pixel fino a 250x250 pixel, alcuni esempi si trovano in Figura 1. Talvolta, esiste una forte variabilità in forma, tessitura, contrasto e dimensione tra particelle appartenenti alla stessa classe; così come, alcuni elementi appartenenti a classi diverse possono essere praticamente indistinguibili.

Per quanto riguarda l'altro tipo di corpuscolo oggetto di studio, numerose ricerche dimostrano che alcuni tipi di polline sono l'allergene più comune in ambienti esterni. A causa del grande numero di persone che soffrono di allergie e del fatto che l'individuazione dell'allergene può essere di aiuto nella cura di queste persone, il conteggio dei pollini nell'aria suscita sempre più grande interesse. A tutt'oggi non esiste tuttavia uno strumento di misura automatico. Il dispositivo utilizzato per la raccolta dei pollini nell'aria è costituito da una macchina che viene disposta sul tetto di qualche edificio, si veda Figura 2. Questa ha una piccola apertura attraverso la quale l'aria e le particelle che essa trasporta entrano. Queste vanno a impattare contro un nastro adesivo solidale ad un disco che ruota lentamente. Il conteggio è allora affidato ad esperti che giornalmente ma molto più spesso settimanalmente prelevano il nastro e ne analizzano al microscopio alcune porzioni al fine di contare ed identificare i pollini raccolti. Un esempio di una foto presa con un microscopio ottico e che fa parte del nostro database è riportata in Figura 3. Come si può immaginare, l'individuazione di pollini in tali immagini è un lavoro che richiede un'alta specializzazione, inoltre è molto lento ed impreciso perché il nastro viene analizzato in poche porzioni. Normalmente i

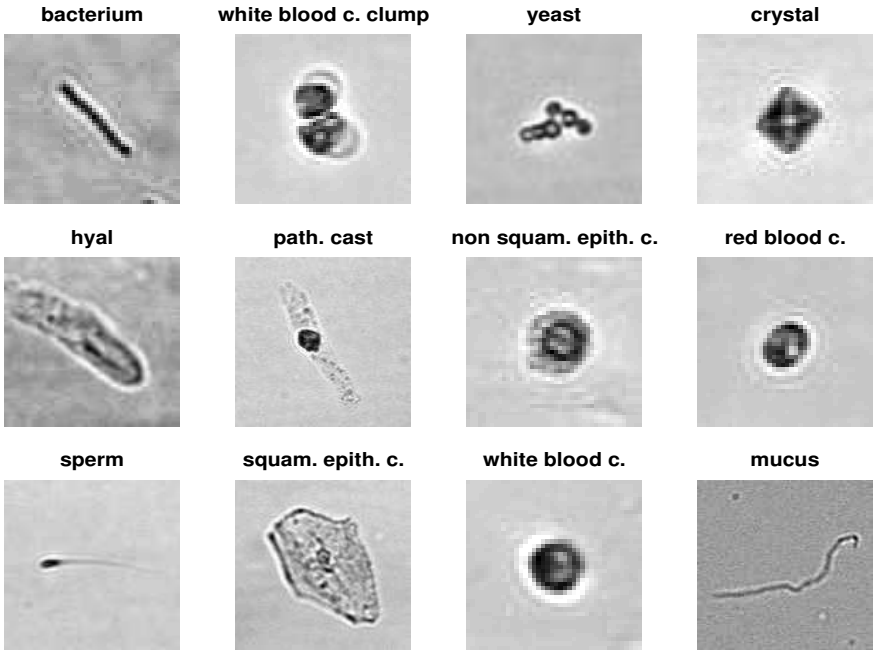

Figura 1: Database di corpuscoli nelle urine: esempi di particelle appartenenti alle 12 categorie.

risultati sui livelli di polline nell'aria vengono riportati nella settimana successiva e quindi il personale medico non può usufruirne per tempo.

Qusto progetto iniziò con la costruzione del database tramite l'utilizzo da parte di un aerobiologo di un software appositamente sviluppato, si veda Figura 4. Grazie ad esso, è stata raccolta per ogni immagine del database una lista, con il genere e la posizione di ogni polline presente. Sulla base di questo, un altro database è stato derivato collezionando per ogni categoria porzioni di immagine contenenti il polline centrato. Esempi delle 22 classi finora collezionate si trovano in Figura 5. Poichè la costruzione di questo database richiede parecchio tempo, si sono collezionate anche immagini di pollini presi direttamente dai fiori. Ciò ha permesso di acquisire più di 1000 campioni appartenenti a sei specie diverse e quindi di far girare su questi degli esperimenti pilota.

Descriviamo ora in termini generali il sistema sviluppato.
Un sistema di riconoscimento si può suddividere in due parti: *rilevamento* e *classificazione*. La prima ha lo scopo di individuare nell'immagine di ingresso punti di interesse attorno ai quali ritagliare una porzione di immagine da mandare al classificatore. La seconda deve stabilire se la particella in primo piano è un corpuscolo di interesse e, in tal caso, deve stabilirne la classe di appartenenza, altrimenti deve scartare il campione. Nel caso delle analisi delle urine il

Figura 2: Dispositivo Burkard utilizzato per la raccolta di pollini nell'aria.

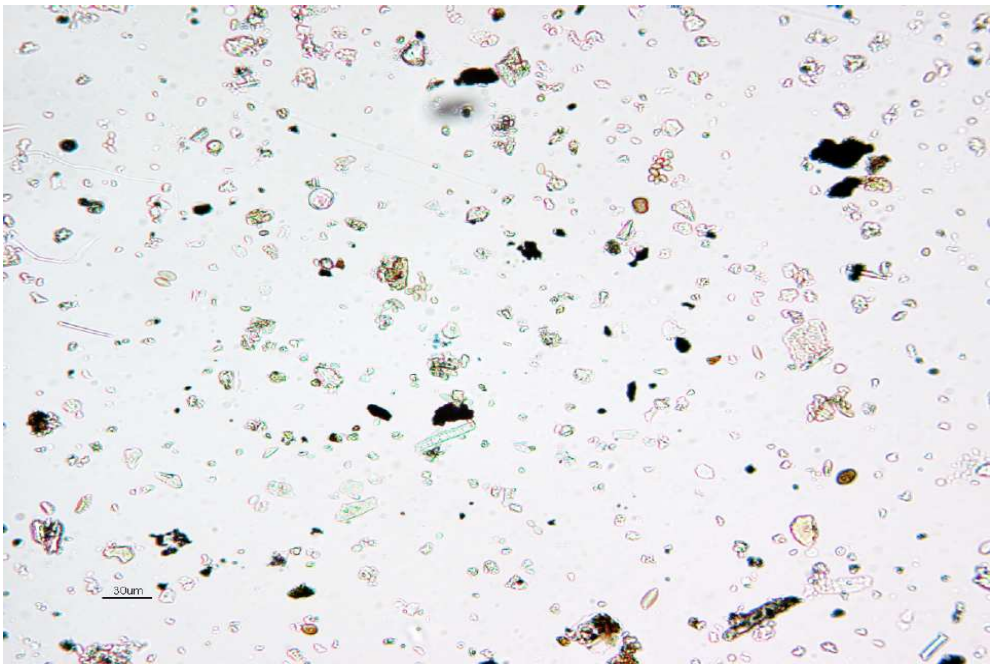

Figura 3: Foto di una porzione di nastro adesivo (lungo meno di mezzo millimetro) con particelle presenti nell'aria di Pasadena.

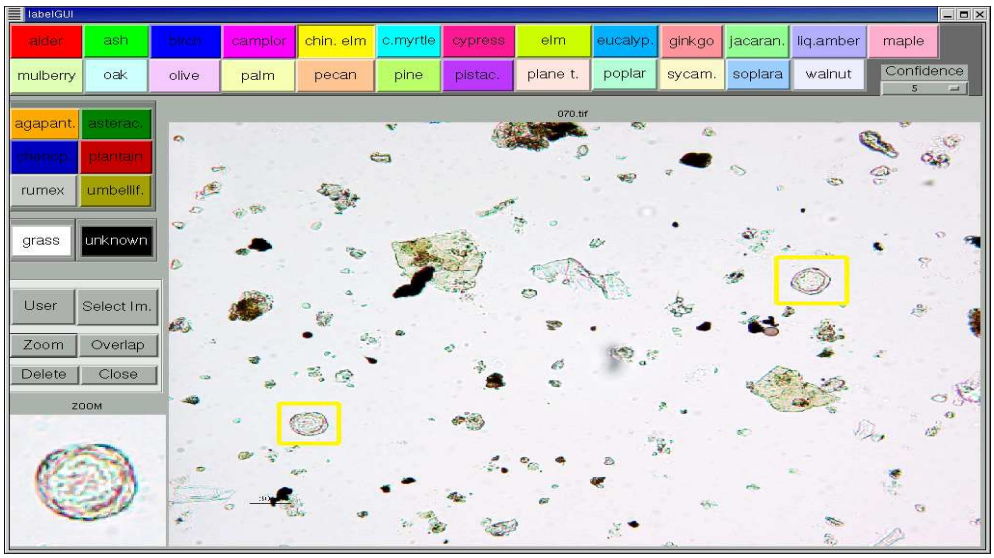

Figura 4: Screen shot del software sviluppato per costruire il database sui pollini. L'aerobiologo, identificato un polline, disegna un riquadro attorno ad esso. Il colore del riquadro è legato alla specie della particella. L'utente ha la possibilità di cancellare e zoomare le porzioni evidenziate, di cambiare il livello di confidenza della classificazione e vedere le precedenti analisi. L'output è una lista con posizione e tipo di ciascun polline trovato.

Figura 5: Esempi di pollini collezionati nel campus di Caltech. Nell'ultima riga ci sono alcuni esempi di altre particelle che sono presenti nelle immagini ma che non sono polline. La risoluzione media si aggira attorno a 50x50 pixel.

rilevamento è semplice perché tutti gli oggetti presenti in una immagine devono essere classificati. Per tale motivo in questo caso non abbiamo dovuto affrontare il problema del rilevamento e le immagini nel nostro database sono già i ritagli esatti degli oggetti di interesse, si veda Figura 3. Invece, nel caso dell'analisi dei pollini il rilevamento deve essere effettuato perché il nastro adesivo colleziona per ore anche polvere, spore e parti di insetti. Abbiamo sviluppato due tipi di rilevatori. Il primo utilizza successivi filtraggi per individuare punti di interesse [20]. Il secondo si basa su operazioni morfologiche. Quest' ultimo pur essendo più lento ha dato i risultati migliori perché è in grado di rilevare con probabilità 9/10 ogni tipo di polline al prezzo di una percentuale di falsi allarmi pari al 1000%.

Una volta che un oggetto di potenziale interesse è stato individuato, dobbiamo estrarre dall'immagine centrata su di esso un qualche tipo di misurazione. I valori estratti, che vanno a formare il *feature vector*, dovrebbero raccogliere tutto il contenuto informativo dell'oggetto. Questi valori sono ricavati da una particolare comprensione delle caratteristiche dell'oggetto o, più in generale, sono una combinazione dei dati di ingresso. Essi non devono essere numerosi perché altrimenti si rischierebbe di rallentare il sistema e di ottenere risultati poco affidabili. Se il *feature vector* non descrive bene i dati di ingresso nessun classificatore potrà dare buoni risultati. In questa tesi, descriviamo due tipi di *feature* derivati dai lavori di Schmid et al. [9] e Torralba et al. [28].
Trovati dei buoni *feature*, la classificazione è concettualmente semplice. In fase di training, il sitema impara a distinguere tra *feature* relativi a immagini appartenenti a diverse classi. In fase di test, una decisione viene presa analizzando il *feature* dell'immagine di test. Sostanzialmente, si va ad assegnare il corpuscolo alla classe il cui modello di training rappresenta meglio il dato di test. Ad esempio, Figura 6(a) mostra due tipi di polline e per ciascuno di questi, due immagini derivate utilizzando una tecnica per l'estrazione di *feature*. Mediando i valori associati ad ogni pixel di queste immagini si ottiene una coppia di valori. In questo esempio cioè, il *feature vector* ha due componenti. Raccogliendo i dati relativi a 100 immagini di ciascuna classe, si ha la distribuzione di Figura 6(b). Se utilizzassimo un classificatore lineare, che divide "opportunamente" lo spazio dei *feature* in piani, si otterrebbe un *error rate*[1] di circa il 15%. Si noti che questo piano deve essere ricavato utilizzando i dati di training.

Nei nostri esperimenti utilizzando *feature* a molte più componenti e diversi tipi di classificatore siamo stati in grado di ottenere un *error rate* del 7.6% sulle dodici classi del database delle urine e del 10.2% su 6 classi di pollini raccolti manualmente dai fiori. La performance è riassunta dalle Figure 7 e 8.

[1] L'*error rate* è definito come il rapporto tra il numero di immagini non correttamente classificate e il totale numero di immagini testate.

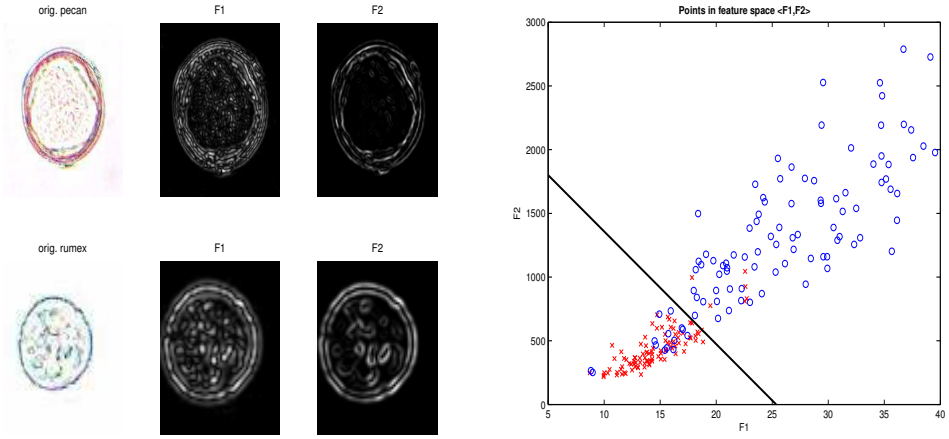

(a) (b)

Figura 6: (a) Colonna di sinistra: due tipi di polline, pecan e romice. Colonna centrale e di destra: processing sulle immagini precedenti, mediando si ottengono dei *feature*. (b) Esempio di classificazione dei due tipi di polline usando *feature* a due componenti: pecan (croci) e romice (cerchi). In questo caso, un classificatore lineare raggiunge un *error rate* di circa il 15%.

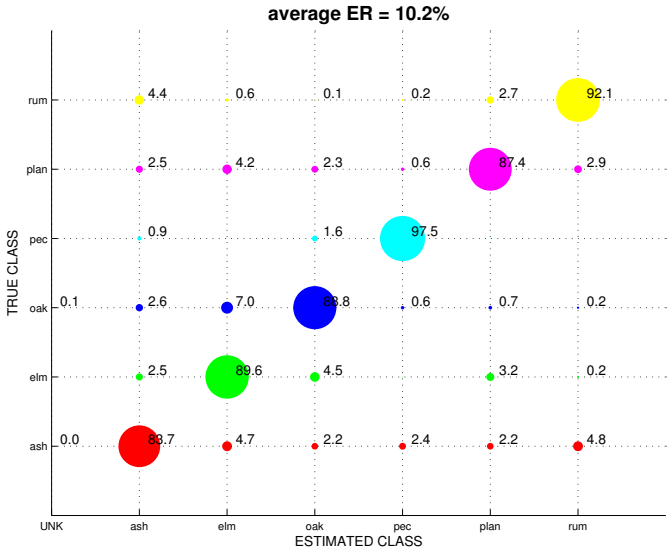

Figura 7: Database dei pollini: matrice di confusione media su 100 esperimenti in cui il 10% delle immagini è stato utilizzato per il test. Ciascuna riga mostra come un corpuscolo di una certa classe viene classificato. Nell'intersezione di riga i con colonna j c'è la percentuale di corpuscoli appartenenti a classe i che sono stati associati alla categoria j.

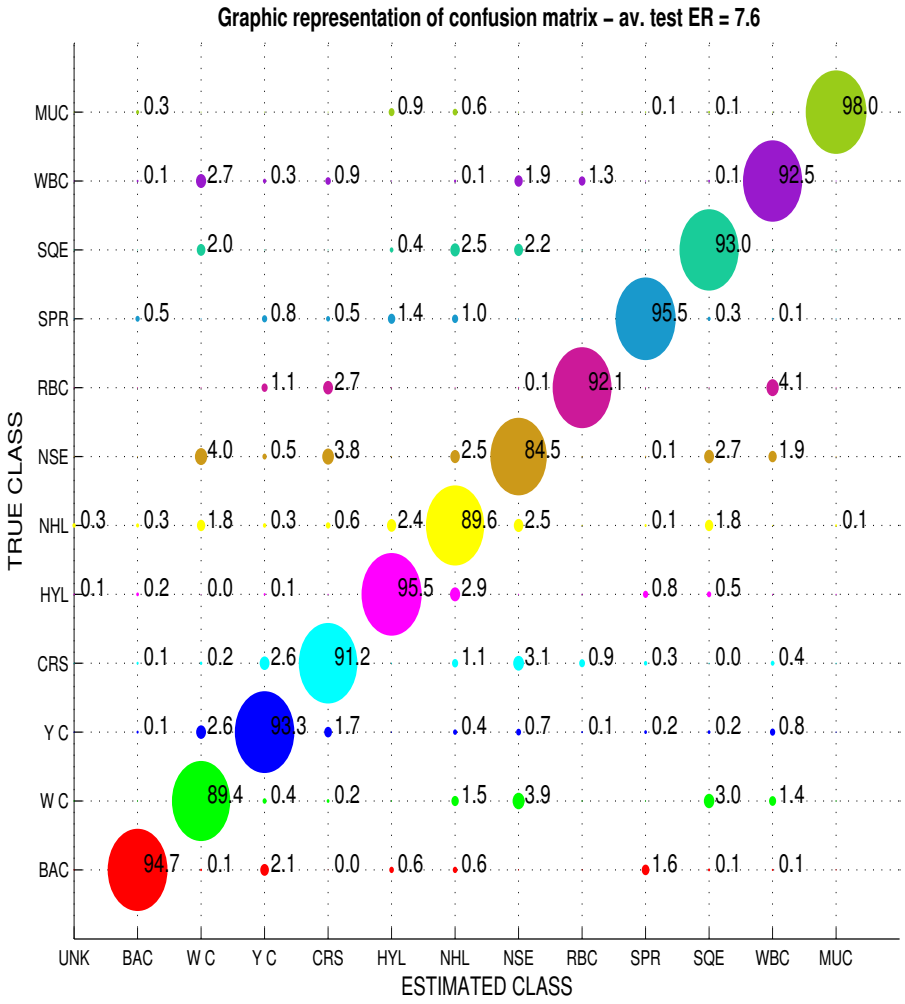

Figura 8: Database delle urine: matrice di confusione media su 100 esperimenti in cui il 10% delle immagini è stato utilizzato per il test.

Questa ricerca si distingue per l'approccio generale utilizzato in classificazione. La tecnica messa a punto consente di classificare molte diverse classi di corpuscoli con la possibilità di aggiornare automaticamente il sistema con nuove categorie. Grazie ai *feature* particolarmente adatti a trattare immagini a bassa risoluzione e contrasto, nessuna segmentazione dell'oggetto di interesse è necessaria. Il sistema descritto è quindi adatto a riconoscere molti tipi diversi di corpuscoli biologici.

In particolare, numerosi passi in avanti sono stati fatti nel riconoscimento dei pollini. Al contrario di altri lavori, il database proposto è composto da immagini prese da un normale e relativamente economico microscopio ottico e non da un microscopio al laser. Questo rende più difficile il riconoscimento ma fattibile la costruzione di uno strumento di misura maneggevole ed economico. In questo lavoro poi si combinano la rilevazione e la classificazione e si sono ottenuti i primi risultati promettenti di quello che potrebbe essere un sistema effettivo di conteggio del livello dei pollini nell'aria.

L'integrazione di alcuni risultati di questo studio può migliorare la performance e l'affidabilità dei sistemi automatici per l'analisi di corpuscoli nelle urine.
Per quanto riguarda il problema del riconoscimento dei pollini, nel prossimo futuro il software sviluppato per costruire il database potrebbe essere modificato per rendere la catalogazione semi-automatica. Questo potrebbe essere il primo passo verso uno strumento completamente autonomo in grado di dare in tempo reale il livello di allergeni nell'aria.

Ringraziamenti

Desidero ringraziare i miei genitori Edda e Francesco per avermi sempre sostenuto durante i miei studi e per essere stati guida sicura e saggia. Altrettanta gratitudine rivolgo ai miei fratelli Elisabetta e Giuseppe perché sono stati un esempio e punto di riferimento nel mio cammino di laurea. Grazie ai preziosi suggerimenti e insegnamenti della mia famiglia, mi è stato possibile ottenere questo ambizioso traguardo.

Ringrazio di cuore il mio relatore Prof. Ruggero Frezza per essersi sempre dimostrato disponibile e fiducioso nei miei confronti e per avermi dato l'opportunità di svolgere la tesi negli Stati Uniti.

Uno speciale ringraziamento rivolgo al Prof. Pietro Perona che mi ha ospitato per sette mesi nel Computer Vision Laboratory presso il California Institute of Technology. La sua guida paziente e illuminata, generosità e creatività sono e rimarranno una pietra miliare nella mia formazione umana e professionale.

Esprimo riconoscenza anche a tutto il gruppo e staff di Computer Vision del Caltech per la loro simpatia, disponibilità e aiuto di ogni tipo: Melissa Slemin, Silvio Savarese, Anelia Angelova, Lihi Zelnik, Pierre Moreels, Michael Fink, Ueli Rutishauser, Fei Fei Li, Marco Andretto, Claudio Fanti, Ulrik Beierholm e Alex Holub.

Dedico un pensiero speciale anche al Prof. Gian Antonio Mian e Prof. Gaudenzio Meneghesso per il loro cordiale supporto e la loro disponibilità, saranno per me sempre un esempio di persone che amano la scienza e il proprio lavoro di ricerca e insegnamento.

Infine, rivolgo un caro saluto a tutti i miei amici e compagni di corso di Padova per aver condiviso con me questi anni di studio e per i bei momenti di spensieratezza passati insieme.

Acknowledgements

I wish to thank my parents Edda and Francesco for their support during my studies and because they have been sure and wise guide throughout my life. I express gratitude also to my siblings Elisabetta and Giuseppe because preceding me with their studies, they were an excellent example and constant reference point. Thanks to the invaluable suggestions and teachings of my family I was able to achieve this ambitious goal.

I wish to express my considerable gratitude to my advisor Prof. Ruggero Frezza for his availability and trust in me and because he gave me the wonderful opportunity to do research in the United States of America.

I am especially grateful to my advisor Prof. Pietro Perona at California Institute of Technology who gave me hospitality for seven months in the Computer Vision Laboratory. His patient and inspired guide, generosity and creativity are a landmark in my human and professional experience.

I thank also all the Computer Vision group and staff at Caltech for their friendliness, availability and help: Melissa Slemin, Silvio Savarese, Anelia Angelova, Lihi Zelnik, Pierre Moreels, Michael Fink, Ueli Rutishauser, Fei Fei Li, Marco Andretto, Claudio Fanti, Ulrik Beierholm and Alex Holub.

I must acknowledge Prof. Gian Antonio Mian and Prof. Gaudenzio Meneghesso's contribution to my educational and professional growth, they will be always an example of people who love science and their work of research and teaching.

I express a last thought for my friends and colleagues at University of Padua because we shared together these years of study and many joyful moments.

Contents

Chapter 1

Introduction

In this thesis, we propose an automatic visual recognition system for biological particles. In particular, we focus on recognition of particles that are found in microscopic urinalysis, and we also deal with the recognition of airborne pollen grains.
Our approach is general, segmentation free, able to achieve a very good performance on many different categories of particles. For these reasons, the system is suitable to be used for recognition of other kinds of biological particles.

In chapter 2, we describe the goal of microscopic analysis in aerobiology and in urinalysis and the usually applied techniques. We conclude this part with an assessment on the need to automate these analyses that will justify this research.
Chapter 3 introduces our databases giving a complete list of available images with a brief description about their characteristics.
The following chapter provides an overview on related work which is a reference point to evaluate the performance of our system. Moreover, we introduce the main stages of a recognition system: detection and classification.
Chapter 5 tackles the problem of particle detection in a given image. We will discuss two approaches having different performances and advantages. The first detector is based on a filtering technique while the second one on morphological operations.
Chapter 6 reviews the features developed for the classifier. These features are derived from previous work of Schmid et al. [9] and Torralba et al. [28]. Thanks to some kind of elaboration, we are able to get from each image a new kind of very informative feature.
In chapter 7, we discuss many classifiers: Bayesian classifiers, a classifier inspired by AdaBoost algorithm and a last one using support vector machines. This chapter is completed by an experimental part which shows the experiments done to tune the system and to compute the global performance.
The following chapter provides an insight about errors done by detector and classifier during the previous experiments.
In chapter 9, we conclude with an extensive analysis of the performance of a complete system, namely detector followed by classifier, for pollen recognition.

The last chapter summarizes the main points of this research. We discuss our contribution in automatic visual recognition of particles and the tasks that will challenge future works.

Chapter 2

Microscopic analysis of biological particles

Microscopic analysis is used in many fields of technology and physics, for example in aerobiology, geology, biomedical analysis, industrial product inspection.
Basically, the input image has a resolution of about 1024x1024 pixels while objects of interest have resolution of about 50x50 pixels. In all these applications detection and classification are difficult, because of the poor resolution and maybe strong variability of objects of interest, and because the background can also be very noisy and highly variable. In this work, we focus on recognition of biological particles and especially on recognition of airborne pollen and on recognition of particles that can be found in urine. Since our approach is general and our performance is very good on many categories of different kinds of corpuscles, we can claim that this research and its results are naturally applicable to other many kinds of biological particles found in microscopic analysis. In this research, we develop a recognition system that is not a specific case study, but it is segmentation free and it can be easily updated in order to deal with new classes.
Focusing in the next sections on airborne pollen recognition and urinalysis, we will explain why and how these analyses are performed, what the problems of manual analysis are, and at the end, we will assess the need to automate this process.

2.1 Measuring airborne pollen level in air

Estimates from a skin test survey suggest that allergies affect as many as 40 to 50 million people in the United States of America. Allergic diseases affect more than 20% of the U.S. population and are the sixth leading cause of chronic disease. In this country, the estimated overall costs for allergic rhinitis in 1996 totaled 6 billion dollars and two years later, the increased absenteeism and reduced productivity due to allergies cost to companies more than 250 million dollars [1]. Moreover, from 1982 to 1996, the prevalence of asthma increased to 97% among women and 22% among men. These statistics are an example that perfectly cor-

responds to the situation and trend in all other countries in the world.
An allergy is an abnormal reaction to an ordinarily harmless substance called *allergen*, [1] [27]. When an allergen is absorbed into the body of an allergic person, the person's immune system views the allergen as an invader and a chain of abnormal reactions begins. The effects of this response are runny nose, watery eyes, itching and sneezing. People with these symptoms are unable to work and even to sleep. The most common allergens are: pollen particles, molds, dust mites, animal dander, foods, medications, insect stings. Pollen grains are clinically the most important outdoor allergens and the most allergenic species are: *American elm*, *paper birch*, *red alder*, *white oak*, *white ash*, *olive*, *mulberry*, *pecan*, *black walnut*, *sycamore*, *grass*, *chenopod*, *rumex*, *plantago*. Note that asthma and allergies can affect anyone, regardless to age, gender, race.

In order to make forecasts and to aid in the diagnosis, treatment and management of allergic diseases, many stations with air sampling equipment are spread in the territory to collect airborne pollen particles.
The most popular device is the *volumetric spore trap*, see Figure 2.1, which draws air into the sampler at a given rate through a little opening. The particles in the air land on an adhesive coated microscope slide attached to a slowly rotating wheel. After a period of sampling, for example one day but most usually one week, the pollen grains caught on the sticky slides are counted under the microscope by simply cutting the long slide into several pieces. The analysis at the microscope is performed by trained observers (aerobiologists) who count and classify pollen grains. This method is slow, expensive, and inaccurate. First of all: the response time is inadequate for many applications. In a typical installation pollen particles are collected during the week on sticky tape. The tape is analyzed only once a week. The results of such analysis are therefore sometimes available one week after the fact, rendering them useless for preparations of medical response in hospitals.
Second, the analysis of one weekly tape takes up to 8 hours of work by a skilled professional, thus, the yearly cost of measuring pollen contents in the air at one location could approach $30,000, too expensive for many institutions and too expensive to allow fine spatial sampling of air pollen contents.
For example, the National Allergy Bureau, section of the American Academy of Allergy, Asthma and Immunology's Aeroallergen Network, is the institution responsible for reporting current pollen count to the media and it has *only* 75 counting stations throughout the US and its members are all *volunteers*; if you check the website of AAAAI [1] the pollen counts are never updated to the last week!
Most importantly: relying on humans produces inaccurate measurements. This for two reasons: first, the process is tedious, it is well documented that the attention of a human operator tends to flag after 30 minutes on a demanding repetitive job. Second, in order to accomplish the task at all, human operators sample coarsely the collected tapes. Measurements are thus accurate for high pollen counts, but inaccurate for low pollen counts, an even more inaccurate as to estimating the concentration of pollen grains over time. It is entirely possi-

Figure 2.1: Burkard volumetric spore trap is used to collect airborne pollen grains and fungi.

ble to miss the presence of a given pollen in the air if the critical time when it was released is not sampled by the operator. Moreover, it is difficult to provide accurate pollen levels for areas not near to a counting station and so the actual counts are useless for most of the physicians.

To summarize, there are many reasons to justify the recent strong interest and the need to automate the count and identification of airborne pollen particles. The manual collection and analysis is not adequate because it is too slow, too expensive, not precise and not able to cover all the territory.

2.2 Urinalysis

Urinalysis can reveal diseases that have gone unnoticed because they do not produce striking signs or symptoms; examples are diabetes mellitus, various forms of glomerulonephritis and chronic urinary tract infections [2]. There are three kinds of urinalysis: macroscopic, chemical and microscopic. The first is direct to visual observation to assess the color and cloudiness. The second one, uses a dipstick to determine pH, specific gravity, content of proteins, glucose, etc. and it is based on the color change of the strip and on its comparison to a color chart. The third analysis, the one of our interest, requires a light microscope and is the most complex. A sample of well-mixed urine is centrifugated in a test tube and then, a drop of sediment is poured onto a glass slide for the examination. Using low magnification, a well-trained expert identifies crystals, casts, squamous cells and other "large" objects. After another adjustment of the microscope to get

a higher magnification, the expert can count the number of smaller objects like bacteria and red blood cells.

Particles in urine can be classified into 12 categories, they are: red blood cells, white blood cells, bacteria, hyaline casts, pathological casts, crystals, squamous epithelial cells, non squamous epithelial cells, yeasts, white blood cell clumps, sperm and mucus. The microscopic analysis is very useful and generally required because it is non-invasive and it gives several indications about disease progress and therapeutic efficacy, [5].

However, this kind of analysis if manually done is intrinsically not precise, time consuming and expensive. There is no standardization in the process of taking a volume of fluid, there is no reliability of the result because the experts may have a different training and experience and last but not least, this work is annoying because repetitive and difficult. The difficulty relies on the strong similarity among some categories of particles and in the variability existing also among corpuscles belonging to the same family.
Moreover, this process is slow and expensive for hospitals.

For these reasons, an automatic recognition system is required in several situations above all when many specimens have to be analyzed. Some systems for automatic recognition of particles in urinalysis are currently sold. An interesting machine using computer vision approach is made by IRIS, a company in the field of biomedical analysis. This company also provided us the urine database.

Our interest in urinalysis is justified because the manual analysis is not efficient in terms of precision, cost and time and because the automatic recognition can be still improved. In the next chapter, we will describe IRIS system and its very good performance but we will highlight also its main flaws.
Other systems using different techniques, such as analysis of particle refraction when these particles are hit by a laser beam, have also drawbacks because of their suboptimal performance and the difficulty to verify analysis outcomes.

2.3 Conclusion

Both aerobiology and urinalysis need automation.
First, manual analysis is slow. For instance, the pollen level in the air is usually given in the following week and so, physicians have available this information when by this time it is too late. Second, manual analysis requires very skilled experts with a high cost for the community and the institutions. Third, because this kind of work is repetitive and difficult, results may be not accurate. Experts' results depend on their experience, their subjective judgment, their way to set up the system. There is a need of standardization in the measurements that can be achieved only with an automatic system.

On the other hand, today there is no completely automatic system to detect and identify pollen particles and the machines for urinalysis have a lot of margin of improvement.

Besides, visual recognition of particles in microscopic images and more generally, recognition of small object categories in images with poor resolution and contrast is a field of research which has never been studied deeply but nonetheless, has many challenging problems to tackle and can find several applications.

Chapter 3

Database

This chapter describes the databases we used in our work.

A company in biomedical analysis, IRIS, provided us the database of cells in urine; these particles are: red blood cells, white blood cells, bacteria, hyaline casts, pathological casts, crystals, squamous epithelial cells, non squamous epithelial cells, yeasts, white blood cell clumps, sperm and mucus. These are twelve categories, samples of this database can be found in Figure 3.1. The resolution is variable and goes from 36x36 up to 250x250 pixels with $0.68 \mu m/pix$.
Table 3.1 shows the number of images in each class of urine database.

CLASS	NR. OF SAMPLES
1. bacteria	1000
2. w. blood c. clumps	1000
3. yeast	1000
4. crystal	1000
5. hyal casts	1000
6. path. casts	860
7. non squam. epith. c.	999
8. red blood c.	1000
9. sperm	1000
10. squam. epith. c.	1000
11. white blood c.	1000
12. mucus	546

Table 3.1: Number of images in each category of urine database

The other database is a collection of pictures of airborne pollen particles taken with the volumetric spore trap (see par. 2.1) and pictures of pollen grains collected manually from flowers, so called "pure" pollen particles. Two example of these pictures are given in Figure 3.2. These images have a resolution of 1024x1280 pixels with $0.5 \mu m/pix$.

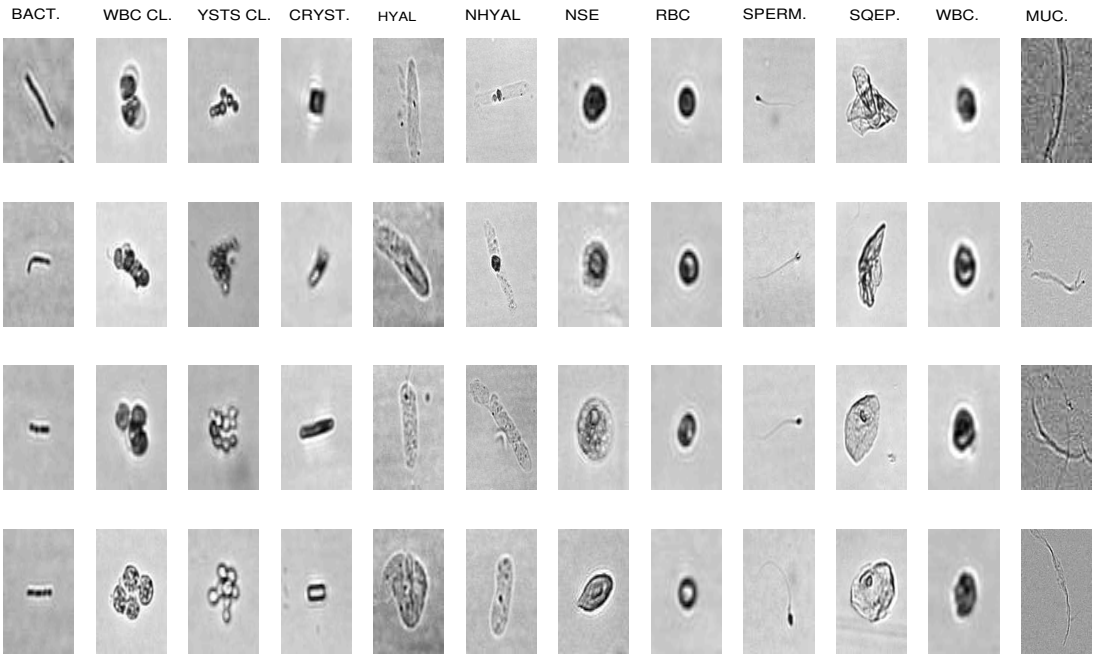

Figure 3.1: Urine database: samples belonging to the twelve categories.

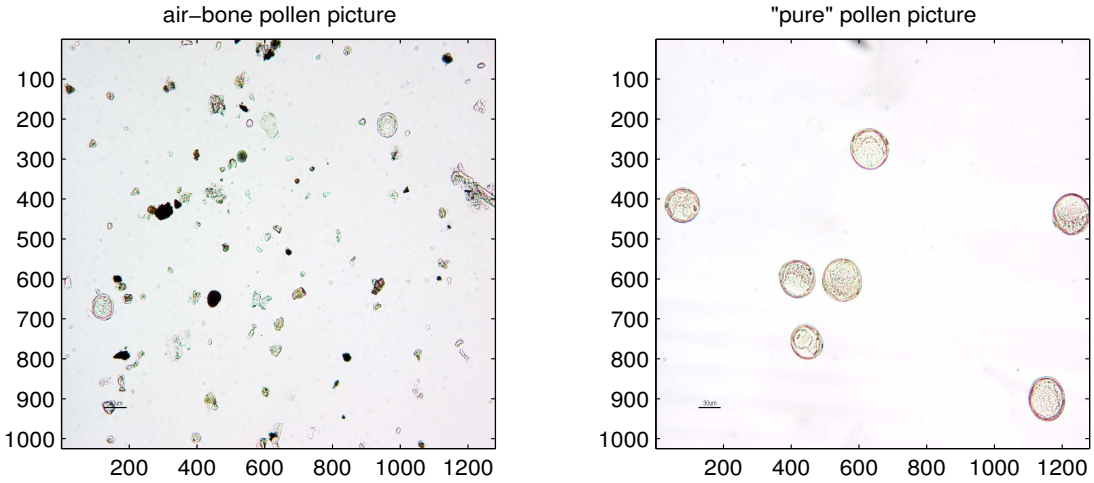

Figure 3.2: Left side: picture of tape containing particles that are present in the Pasadena air. Right side: picture of "pure" pollen particles.

In order to build this database, we started developing a software for enabling human operators to manually collect a large training set, consisting of about 1000 samples of grains of pollen for each of 32 species which are found in Pasadena's area. For this purpose we built a Matlab graphical user interface (see Figure 3.3) with which we have already collected up a number of samples summarized in Table 3.2. Thanks to this software, we have a reference list which stores for each image the position and the genus of each pollen identified by some expert. Given this information, we derived two databases of patches centered on pollen particles: the first one collects airborne pollen grains (see Figure 3.4), the second one "pure" pollen grains. Our database has images with "pure" pollen particles because of their easier and faster labeling and because in this way it is simpler to retrieve a large number of samples which are useful to run pilot experiments (see par. 7.5.2).

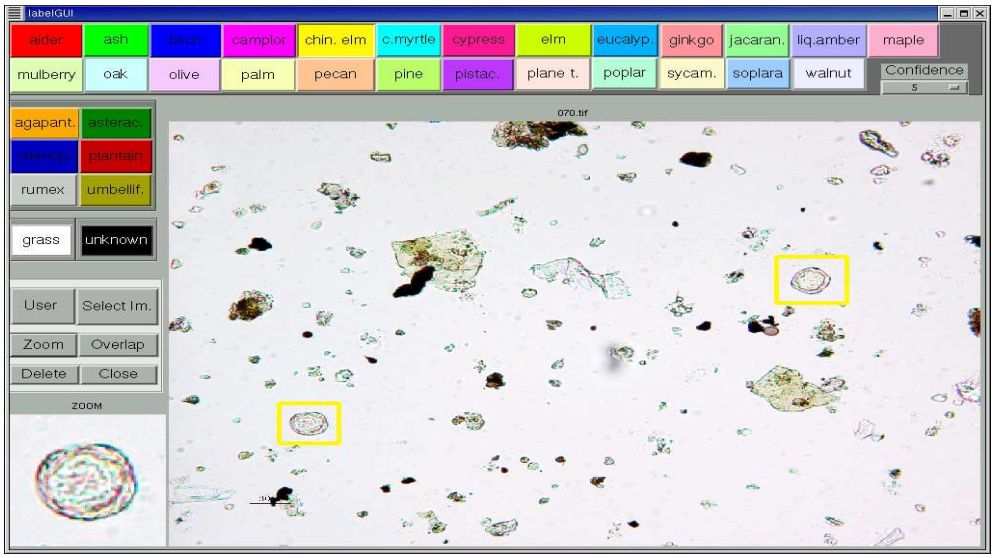

Figure 3.3: Screen shot of software for labeling pollen grains. The expert has to identify pollen particles in the image and to select around them boxes. The color of the box is related to the pollen genus. The user can remove and zoom boxes, view the previous work and change the confidence of his classification. The output is a list with position and genus of each identified pollen.

Figure 3.4: Examples of pollen grains collected in Caltech campus. In the last row, there are other particles that are similar to pollen grains and that are found in the acquired images. The average resolution is about 50x50 pixels.

CLASS	"PURE"	AIR SAMPLER MACHINE
ash	1282	75
chin. elm	1916	124
oak	1479	66
pecan	1212	5
plantain	1549	0
rumex	1014	0
birch	342	0
cypress	188	37
eucalyp.	280	2
grass	285	2
olive	309	11
pistac.	314	0
walnut	235	18
pine	99	43
liq. amber	113	21
alder	78	13
asteraceae	0	6
c. myrtle	127	2
chenopod	0	20
ginkgo	0	3
mulberry	0	38
palm	0	18
plane t.	0	10
poplar	0	5
sycamore	0	16
umbellif.	0	4
unknown	49	23
total	*10871*	*562*

Table 3.2: Pollen database: patches (pollen grains) extracted from 299 sticky tape images and 778 images having only "pure" pollen grains.

Chapter 4

Overview on related work

The aim is to build a system for automatic recognition of particle categories. Furthermore, we are interested in a general approach enabling us to work with several kinds of corpuscles which are found in microscopic analysis. In this way, it is easy to add new classes to the already considered set and, no new customized reprogramming is required.

Generally, input images of a such system have resolution of nearly 1024x1024 pixels, while the objects to which we are interested on have square bounding box with side between 30 and 200 pixels. The average side is around 60 pixels, then, the system has to handle objects with low resolution. Its output is the number of detected particles in each category.

The automated analysis proceeds in two parts: *detection* and *classification*, an outline is shown in Figure 4.1.

In the detection stage the system will select those parts of the image which are likely to contain a particle of interest, for example a pollen. This process is akin to visual attention in humans: most of the computation is devoted to the most promising areas of the image.
The second stage, that is classification, consists of taking image portions which contain a visual event associable to a particle of interest, and attributing such event either to one out of a number of known species or, to an "unknown object" grab-bag category.

In urinalysis detection is not a problem, because in the pictures of stream (see next section for a detailed description) all particles have to be analyzed. Once that overlap among cells is avoided, all objects in the image will be classified. Moreover because of the tipical low concentration of particles in the fluid, particles are quite well distributed on the original image. Detection for urinalysis is not a great task. For this reason, our urine database is a collection of patches with particles already well centered; whereas in pollen recognition, detection is still crucial, because the input images of the system are pictures of sticky tape.
A given section of tape has accumulated airborne particles for many hours. Such an image contains hundreds of particles like: pollen grains, dust, insect parts, etc. The detection process should quickly flag the location of those particles that

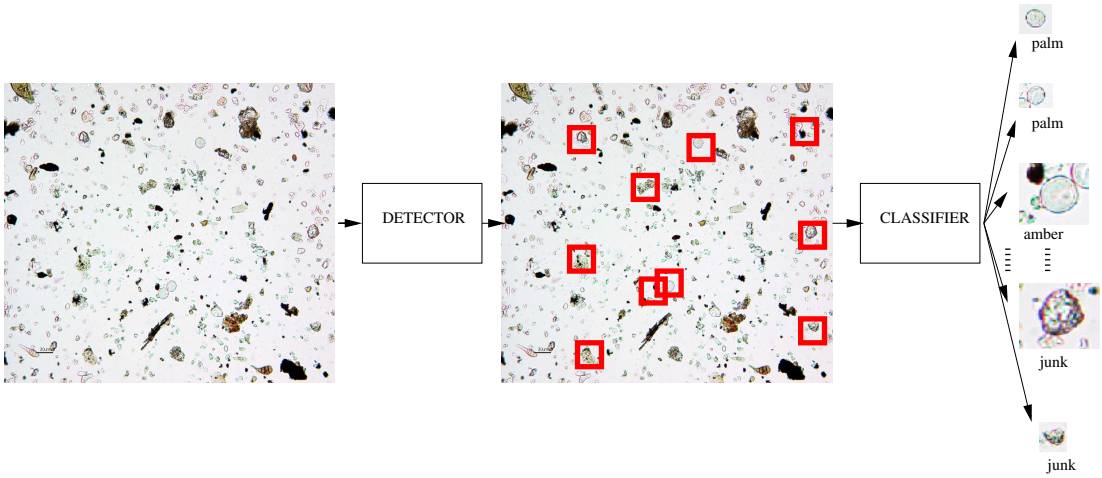

Figure 4.1: Outline of recognition system. Detector finds interesting points in the input image and gives back to the classifier a certain number of patches. For each patch, the classifier establishes the class to which the object in foreground belongs.

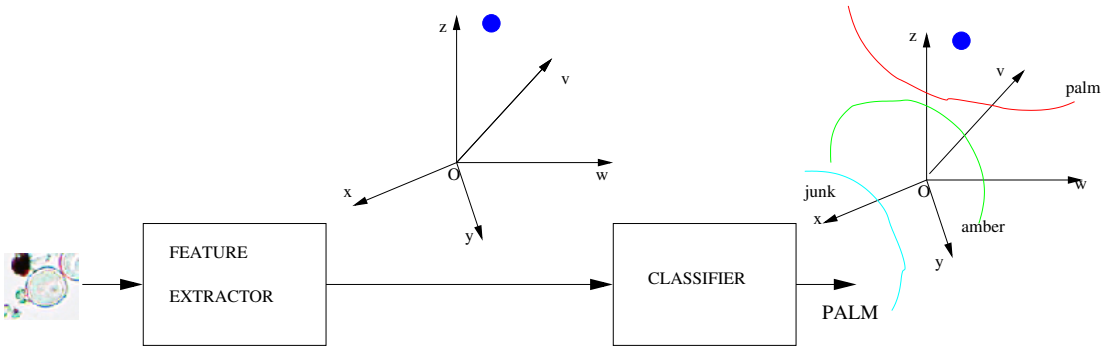

Figure 4.2: Outline of classifier: the system extracts from the input patch a set of features. In the training period, the system learns how to divide the feature space. In the test phase, the system assigns a class to the input image looking at the region where the test feature falls.

have at least a small chance of being pollen particles. At this stage the number of false rejects, i.e. pollen particles that are not selected, must be extremely low because some species can have low counts and we have to take into account also classifier mistakes.

Classification of both urine particle patches and pollen patches has to establish if the particle is of interest, in which case the class will be also identified, otherwise, it has to be discarded.
This is a visual *pattern recognition* problem, whose solution is conceptually simple. Given a signal s belonging to a class k, $k = 1, \cdots, K$, the main stages of classification are:

1. a number of features are extracted from the original signal to form the *feature vector* $x \in \mathbb{R}^D$, that is the image transformed into a *pattern*.

2. a decision function must be determined:

$$\begin{aligned} r : \mathbb{R}^D &\to 1, \cdots, K \\ x &\mapsto r(x) \end{aligned} \tag{4.1}$$

   In many cases, a discriminant function $g(x, k)$ is used:

$$r : x \mapsto \max_{k \in 1, \cdots, K} g(x, k)$$

   This can be regarded as a *trained pattern classifier*, an outline of a classification system is shown in Figure 4.2.

It is well-known, that in the pattern recognition the crucial step is designing informative features: if our features do capture the peculiarities of the appearance of our objects, then, almost any classifier will perform a competent job (Duda and Hart, [13]).

The task of classification even if conceptually simple, is practically a hard challenge. The classifier has to handle images with very low resolution and often poor contrast.
In addition, pollen identification is difficult because [27]:

- there is a large number of look-alike categories
- each genus of plant has many species (strictly speaking, we are classifying among genera)
- high winds may carry unusual kinds of pollen
- pollen shape and texture can be corrupted by previous impacts
- pollen shape depends on its orientation on slide; most frequently are seen in the equatorial position, in which they all appear as ovoid

- "apparently trees do not read literature and insist upon producing pollen grains with the same number of sides as some of other pollen kinds" [27]

Urine particle classification is difficult because:

- some cells are semi-transparent, i.e. casts and mucus
- almost all categories have high variability in shape, texture and size; for example, there is no defined shape and size for clumps, crystals can be square, rectangular or hexagonal, white cells can have a nucleus or a uniform texture
- there is a smooth transition between particles belonging to different categories and even human experts do not agree in the classification of some casts or blood cells; for example, a "big" red blood cell is completely not distinguishable from a "small" white blood cell.

To summarize, the system for automatic visual recognition of particles is composed by a detector and a classifier. The detector is simply achieved in urinalysis, because all objects in foreground are objects of interest while in pollen recognition the detector has to deal with a lot of non-pollen particles. The detector must have an extremely low missed-detection rate. The classification of patches passed by the detector, is similar in both cases. In both situations in fact, the classifier handles images with poor resolution and contrast, and there is a strong variability *between* classes, but sometimes just a little variability *within* some categories.

In the next sections, we will present approaches developed by other research groups in the field of visual recognition of particles or, more generally, visual recognition of small objects in images with low contrast and resolution.
We will start describing IRIS urine analysis system that is somewhat our reference point for the urine project, then, we will see another approach due to Dahmen et al. [11]; for this last method, we had enough details to make a program based on that research and so we can make a direct comparison between this technique and our method. Finally, we will focus on the detection problem and we will present the work of Burl et al. [8] about the identification of volcanoes in Venus surface, and we conclude introducing a technique for pollen recognition [24] and another technique for its identification, [14].

4.1 IRIS urine analysis system

Thanks to the courtesy of IRIS, we will refer to [5] and to many discussions with scientists from IRIS to describe their system. However, we have available only few information about the machine they are selling and we will be able to show only an outline of their technique.

The *iQ200 Automated Urinalysis System* is a bench-top analyzer able to perform chemical and microscopic analysis. The former one is focused on the determination of color, gravity and composition of urine. The latter one is used to analyze the sediment, this is useful in the diagnosis of renal and urinary tract diseases. Each kind of analysis is performed by two different but connected modules. The goal of the module for particle recognition is to overcome the limitations of manual microscopy: lack of standardization and precision, risk of biohazard, slow processing and high costs because it requires highly trained technologists. This analyzer is able to classify and quantify 12 particle categories (the same ones of our urine database) based on a visual recognition system.

In Figure 4.3, you can see an outline of this module. They take from a given specimen $2\mu L$ of centrifugated urine, they make a very thin flow through a channel and then, they take 24 pictures per second with a CCD digital camera coupled with a microscope. In this way, they get around 500 images with resolution 1024x1280 and 0.68 $\mu m/pix$. Given a frame, they are able to detect patches centered on particles by morphological operations or simply by the application of a threshold. Note that they mechanically avoid the overlap among particles by regulating the thickness of the flow. Then, they extract from each patch features that take into account: the image size, the contrast of particle in foreground with respect to the background mean, the shape of the cell and its texture. Given these features from each patch, they train a neural network to make a decision in test. They claim that on our database their system has a very good performance with an error rate[1] of nearly 5%. In the every day use of their system with the data of their customers, they state the classifier has an error rate of about 10%. A specimen is processed in nearly 1 minute and their system allows a continuous load with a maximum of 55 samples.
They claim that the hard tasks for this system are:

- to handle low contrast particles because they perform masking operations to determine some features like shape and size; for this reason, the most not correctly classified classes are Mucus and Casts

- to handle unknown particles

This last point requires a special comment. In urine, there are corpuscules of unknown origin which have never been studied and which are not of interest in the actual analysis. All these particles should be collected in an artifact class which collects also images out of focus or not well segmented. However, they state that this class fills all the feature space and makes classification quite difficult. For this reason, they have chosen the "abstention" rule: when the outcome of the system has a low confidence they discard the image and put it on the artifact class. In this way, they show to the user images with high confidence and reliability for the twelve categories of interest with possibility to check mistakes (the patches

[1]The error rate is the ratio between the number of not correctly classified test images and the total number of tested images; its value allows to assess the performance of a classifier.

are stored in the memory of two computers positioned under the bench). There is still the problem that the artifact class captures also a lot of particles belonging to other categories. In our database, we have not available patches belonging to the artifact class.

We observe that a segmentation-free approach could solve the problem of misclassification among low contrast categories and boost the performance of the system. To take into account features based on shape, interest points can be extracted from a given patch. Our method is based on the first principle and achieves a very low error rate in these categories, is much simpler, is more easily updated with new classes even if it has a slightly higher global error rate.

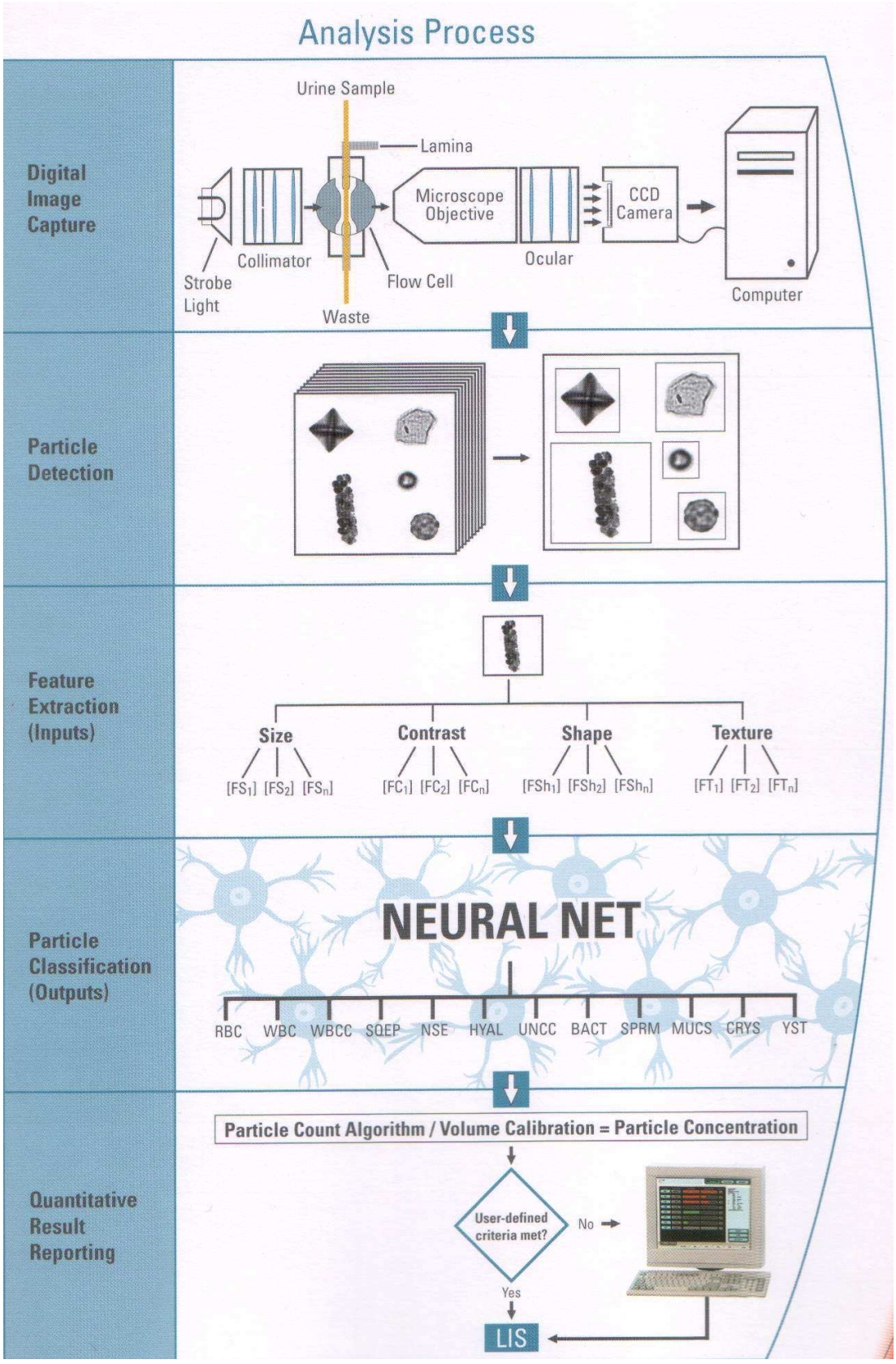

Figure 4.3: Outline of IRIS system for visual recognition of particles in urine (courtesy of IRIS), see par. 4.1.

4.2 Fourier Mellin Transform

The approach formulated by Dahmen et al. [11] is general and segmentation free like the system we are describing in this thesis. Their idea to extract features that are invariant with respect to shift, rotation and scale is powerful because it allows to obtain the same measurement from cells that are found in different positions, orientations and scales.
They aim to classify three different kinds of red blood cells (namely, *stomatocyte, echinocyte, discocyte*) in a database of grayscale images with resolution 128x128 pixels. Given an image, they extract Fourier Mellin based features that are invariant with respect to 2D rotation, scale and translation. Then, they model the distribution of the observed training data using Gaussian mixture densities. Using these models in a Bayesian framework they are able to perform the test and to achieve an error rate of about 15%.

Let be $f[x, y] \in \mathbb{R}^{N \times N}$ a 2D discrete image, its discrete Fourier Transform is defined as

$$F(u, v) = \frac{1}{N} \sum_{j=0}^{N-1} \sum_{k=0}^{N-1} f[j, k] e^{-\frac{2\pi i(uj+vk)}{N}} \tag{4.2}$$

with $i = \sqrt{-1}$ and $u, v = 0, 1, ..., N-1$. It can be easily shown that the amplitude spectrum A of $F(u, v)$ is invariant with respect to translation, inverse invariant with respect to scaling and variant with respect to rotation. By transforming the rectangular coordinates (u, v) of $A(u, v)$ to polar coordinates (r, θ) and by using logarithmic scale for the radial axis, image scales and rotations become shifts in the log-polar representation $\hat{A}$ of A. If you compute the amplitude spectrum B of the Fourier Transform of $\hat{A}$, you can extract features which are invariant with respect to rotation, scale and translation. Moreover, $\hat{A}$ is real valued, thus B is symmetric and you can consider the values that fall in window of size for example 25x12 pixels (the origin will fall in the middle of a longer side of this window). They reduce the dimensionality of the space to d using a linear discriminant analysis (we suppose they apply and we applied in our implementation Fisher's discriminants, [6] [23]).
For example, in our implementation of their system using our urine database we sampled the images to a common resolution of 90x90 pixels[2]. So, reshaping the image in a column vector we decrease the feature space dimension from 8100 to 300 thanks to the symmetry of Fourier Mellin transform and to the windowing operation, then we achieve a further reduction projecting the data along directions given by Fisher linear discriminants and thus, we work in a final 11 dimensional feature space.
In Figure 4.4, we show the Fourier Mellin Transform of a bacterium image. Note that in order to change the coordinates from rectangular to log-polar you have

[2]Note that when an image has a resolution smaller than 90x90 pixels we add a frame with values equal to the estimated background mean.

to apply the inverse mapping and interpolate the values. If (x, y) and (r, θ) are the coordinates in the cartesian system and in the polar one respectively, then

$$\begin{cases} r = \sqrt{x^2 + y^2} \\ \theta = \arctan y/x \end{cases} \quad \begin{cases} x = r\cos\theta \\ y = r\sin\theta \end{cases} \tag{4.3}$$

Given a grid of (r, θ) values, the correspondences in (x, y) are computed and the values in these points are taken (generally with interpolation).
With reference to Figure 4.4, the plot on the upper left corner is obtained automatically by Matlab command *cart2pol*, instead the plot on the upper right corner is a mesh of the data computed by inverse mapping. You can also notice the symmetry of the Fourier Mellin Transform in the lower right corner; the box superimposed shows the window of features that will be extracted.

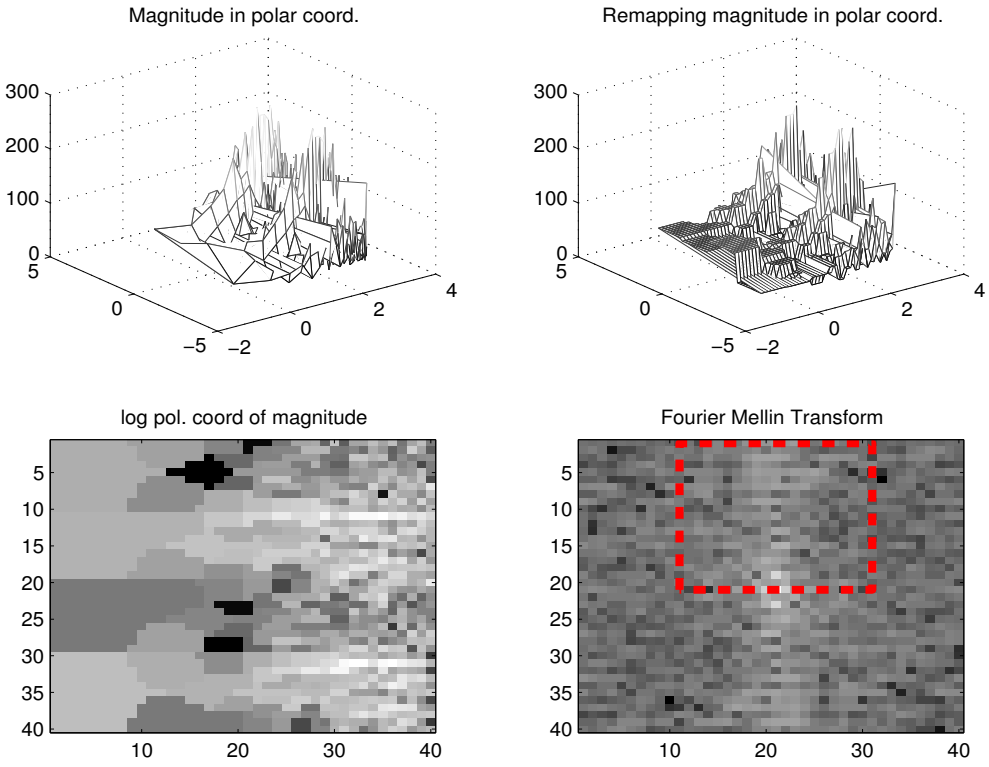

Figure 4.4: Operations involved in the computation of Fourier Mellin Transform: example taken from a bacterium image. Upper left corner: mesh of "cart2pol" command to Fourier Transform of the image; upper right corner: mesh obtained by inverse mapping; lower left corner: magnitude of Fourier Transform in log-polar coordinates; lower right corner: Fourier Mellin Transform.

Once a Gaussian mixture model is estimated for each class, to classify an observation $x \in \mathbb{R}^d$ the Bayesian decision rule is applied

$$x \mapsto r(x) = argmax_k p(k)p(x \mid k) \tag{4.4}$$

where $p(k)$ is the *a priori* probability of class k, $p(x \mid k)$ is the *class conditional* probability for the observation x given class k and $r(x)$ is the classifier decision.

The results of this technique on our database are quite good with an error rate of about 21% for the classification of the 12 categories of urine database, see Figure 4.5.
This performance is consistent with the one achieved by the authors on their database, error rate of 15% on three classes. Using the same data, our technique is able to halve this error rate (see par. 7.5.2).

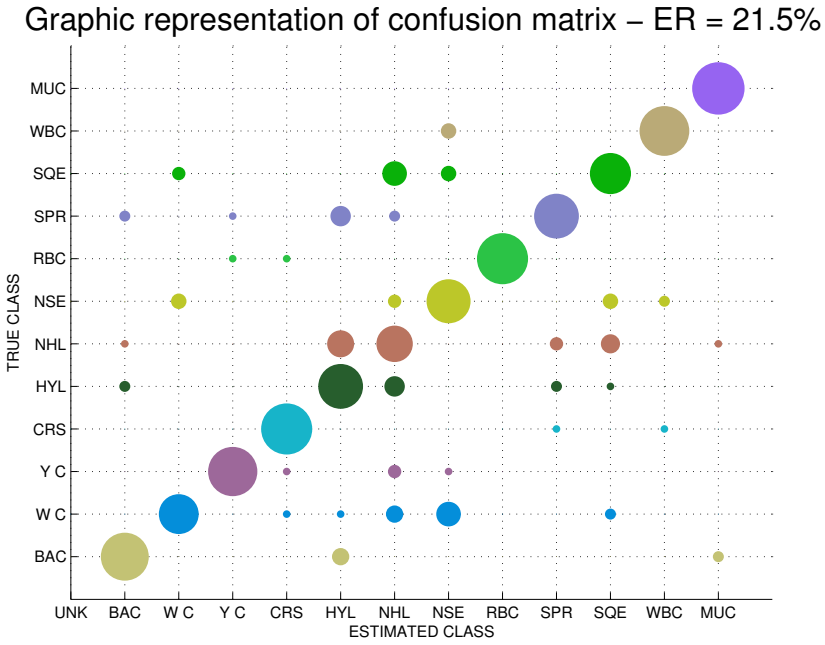

Figure 4.5: Confusion matrix of the classifier using features derived by Fourier Mellin Transform. This result has been achieved thanks to our implementation of the method described by Dahmen et al. [11], see par. 4.2. Each row indicates how a given class of corpuscles was classified. The training is done taking 500 images in each category.

This method is particularly interesting because it is able to achieve a good performance with quite simple features and it does not require any segmentation. On the other hand, the performance is still not acceptable for any real application and not comparable with commercial systems.

4.3 Detection of small objects

In this section we will refer to the research of Burl et al. [8] about the identification of volcanoes in Venus surface. A tipical image, of their database is shown in Figure 4.6. Their database had many thousands of 1024x1024 images derived

from the successful Magellan mission to Venus of NASA-JPL (1989). Their task was to identify in this large database the volcanoes by an automatic vision system. We are referring to this work because the detection of these small objects in such a big image is similar to the detection of pollen grains in a picture of sticky tape piece.

As we did to build the pollen database, through a graphical user interface they labeled examples in a certain number of images. Applying a suitable matched filter and looking for the maximum values in the cross-correlation image they find interest points. Given an interest point, they consider a patch of $k \times k$ pixels centered on it and they use principal component analysis (or discrete Karhunen-Loeve transform [16]) to reduce the space dimension. Finally, the classification is achieved using the quadratic classifier, that is they model the two classes (volcano and not-volcano) with gaussian densities and then, in test they apply Bayes' rule

$$p(\omega_i \mid y) = \frac{p(y \mid \omega_i)p(\omega_i)}{p(y \mid \omega_1)p(\omega_1)p(y \mid \omega_2)p(\omega_2)} \tag{4.5}$$

where y is the observed feature vector and ω_i is the i-th class.

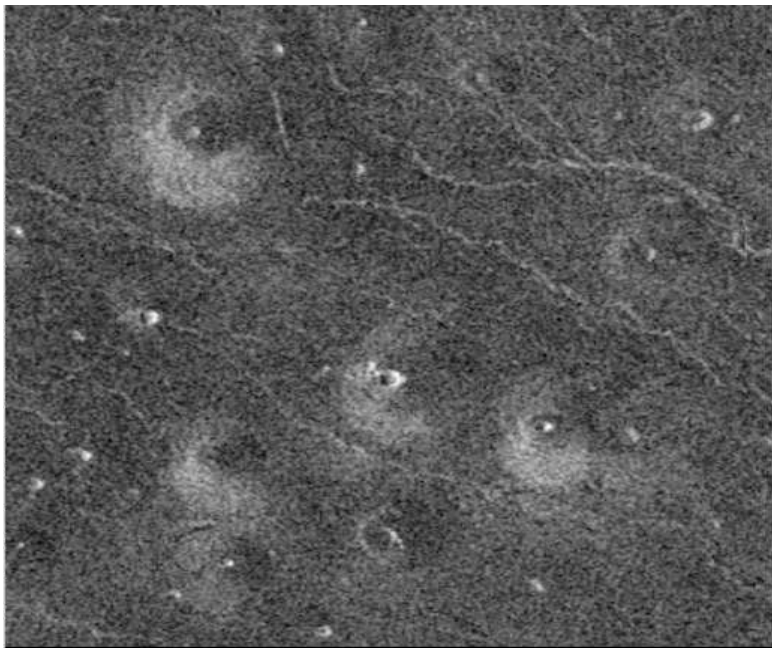

Figure 4.6: This image shows a 30Km×30Km region on Venus containing a number of small volcanoes.

The main common aspects between this research and our research are:

- method to build the database (we are referring to the pollen database)
- the philosophy of the detector for which we allow a high number of false alarms to get an high detection rate

- the classifier philosophy because there is a modeling of training data and then a decision based on Bayes' rule

On the other hand, the main differences are:

- their classifier works in a binary case (only two classes)
- their detector handles images with a lot of gaussian noise, instead our (pollen database) images have only much more variability in the background
- our categories can have less variability in size but generally, have more variability in shape and texture

4.4 Using SEM and 3D data for pollen recognition

We describe here a research developed mainly by Ronneberger [24] at Freiburg University in collaboration with the weather service of Germany and Swiss.
In their work, they highlight that by using fluorescence microscopy instead of the common translucent one it is easy to discriminate between biological and non-biological material. Moreover, they observe that an expert has to analyze a pollen grain on different planes to be sure of his classification. For these reasons, they take with the highest available quality 3D data of pollen grains by a laser scanning microscope.
Given a database in which each pollen is represented by a stack of images (one image for each scanned plane), they compute some gray-scale invariants to avoid object-specific programming. These invariants are kernels (i.e. multiplication of two gray values belonging to pixel at a certain distance) evaluated and summed over all angles or over all the shifts. Finally, they use support vector machines to classify.
Their database has a collection of 26 species of "pure" pollen particles for a total of 385 corpuscules. They assessed the performance with the the technique "leave-one-out", that is, they performed 385 tests on each pollen taking for training the rest of images in the database. They achieved an error rate of 8%.

The main weak points of this work are:

- it is not feasible, a laser scanning microscope is very expensive and not suitable for a real-time and low-cost instrument
- the method is cumbersome because it requires a 3D analysis
- their database is very small and so their performance is not reliable
- "pure" pollen grains are much less variable in appearance and size than pollen particles captured by air sampler machine (see chapter 8 for an experimental prove).

4.5 Pollen identification with Paradise network

In [14], the authors describe two methods of pollen identification in images taken by optical microscope.
This work is one of the first attempts to automate the process of pollen identification using optical microscope. Indeed, several researches were done using scanning electron microscope (SEM) and good results were achieved, [29] [18] [22] [19]. But, SEM is expensive, slow and absolutely not suitable for a real-time application.

Their first method is a model based approach and it assumes that pollen grains have a "double edge" in the exine. Thus, a "snake" (a proper spline) is used to detect the presence of this edge. Since not all pollen grains show the double edge property and since the achieved performance is not so good we do not go in further details.

The second approach uses the so-called "Paradise Network". Several small templates which are able to identify important features in the object, are generated and then linked together to form a certain number of patterns. This scomposition is repeated in test and the system looks for the best matching between the pollen and non-pollen patterns. The network is able to recognize nearly 80% of pollen as pollen and misclassify 4% of the debris as pollen.

This work is interesting, because they use images acquired with the common equipment, namely volumetric spore trap and the optical microscope. On the other hand, their performance is still not acceptable for any practical application and is referred to a system that receives as input already segmented images of pollen or junk particles. Moreover, they limit their study only to pollen particles with a double edge in the exine.

4.6 Conclusion

In the previous chapter we explained the need for an automatic system for particle recognition as opposed to the manual analysis done by highly trained experts.
In this chapter, an overview was given on researches focused on automation of microscopic analysis.

In the urinalysis case, even if there is already a good system for automatic particle recognition, it can be still improved using segmentation free approach and trying to build a more flexible system able to extend the classification to new categories.

Pollen recognition is still manually done. The attempts to use SEM give good but useless results because no cheap, portable and real-time instrument can adopt this technology. On the other hand, no research was able to find good performance in detection and classification using optical microscope images of sticky tape pictures.

All these considerations justify our interest and research in automatic visual recognition of biological particles.

Chapter 5

Detector

Detection is the first stage of a recognition system. Given an input image with a lot of particles, it aims to find key points, which have at least a little probability to be a corpuscle of interest. Once that one of these points is detected, a patch is centered on it and then, it is passed to the classifier in the next stage. It is extremely important to detect almost all the objects of interest when they are rarely found in images and their number is low, as it typically happens in pollen detection.

In our research, we need to detect points only in pollen database. This database was labelled by human experts and a reference list has been built with information about genus and position of pollen particles sampled from air and now in images.
Thus, we evaluate performance by measuring how well our automatic detector agrees with the set of reference labels. A *detection* occurs if the algorithm indicates the presence of an object at a location where a pollen exists according to the reference list. Similarly, a *false alarm* occurs if the algorithm indicates the presence of an object at a location where no pollen exists according to the reference list [8].
The overall performance can be evaluated computing:

$$\text{perc. of detection} = \frac{\text{nr. of detected interest particles}}{\text{nr. of particles of interest}} * 100 \tag{5.1}$$

$$\text{perc. of false alarms} = \frac{\text{nr. of detected particles which are not of interest}}{\text{nr. of particles of interest}} * 100 \tag{5.2}$$

More precisely, we consider a box centered on the detected interest point. We say that there is a matching between this box and the expert's one, if

$$\sqrt{(x_{c1} - x_{c2})^2 + (y_{c1} - y_{c2})^2} \leq \alpha \sqrt{\frac{A_1 + A_2}{2}} \tag{5.3}$$

where x_{ci}, y_{ci} are the coordinates of the box centroid, A_i is the area of the box and α is a parameter to be chosen. In our experiment, we chose α equal to $1/\sqrt{2}$.

This value and parameter are the same ones we used in the software we developed to label pollen grains. In that situation, eq. (5.3) is used to establish when two expert's boxes overlap and if this condition is satisfied then, the software removes the old box because there is too much overlap and we interpret the old box as a mistake. Analogously for the detector, if the same condition holds, we say that there is a matching between the automatically detected box and the expert's one.

Typically, a detection system has some parameter to tune. When one parameter is varied then, also the false alarm and detection percentages change. Thus, by varying at each time a threshold, we can compute a sequence of percentages. The resulting curve is known as receiver operating characteristic (ROC) curve.

In the following sections, we will describe two detectors and we will assess their performance thanks to ROC curves.

5.1 Detector based on difference of Gaussians

This detector is based on a filtering approach [20] [21].
The outline of this system is shown in Figure 5.1; an example of the involved computations using an image of pollen database is shown in Figure 5.2.

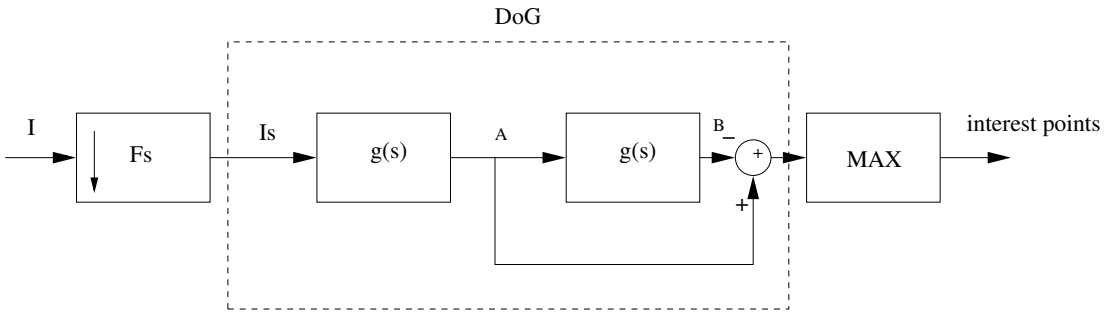

Figure 5.1: Outline of detector based on DoG computation.

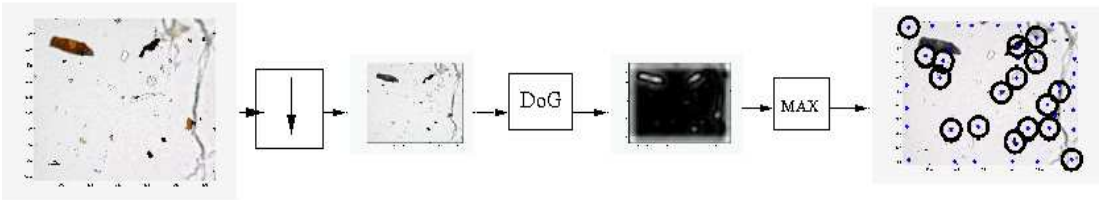

Figure 5.2: Example of computations done by DoG detector for an image of pollen database.

The input image is converted in gray level values and sampled with a sample frequency F_s. Then, it is filtered two times with a Gaussian kernel with a certain standard deviation σ to produce images A and B. Finally, we extract interest points looking for the maxima and minima in the image $A - B$.

In Figure 5.3, we show the plots of Gaussian kernel and difference of Gaussian (DoG) kernel and their DFT in the 1-D case.
The goal of the sampling stage is to make the smallest pollen appear a little blob of few pixels. This automatically removes dust particles smaller than pollen grains and reduces the amount of computation. With a proper choice of the variance of the Gaussian kernel σ, the output image will have a peak in correspondence of round shaped objects with a certain size. Figure 5.4 shows a synthetic example in which two filters with DoG kernels having different σ are applied to an image. When σ is low, the output image has a narrow peak in correspondence of the little blob of the input image. When σ is high, the peak is in correspondence of the largest blob. The variance of the Gaussian kernel allows to select the size of the interest objects.
In order to detect how good a point of extremum is in the output image, we fit around it a paraboloid. The vertex of this paraboloid gives the exact position of the interest point and its curvature is a measure of its quality. If this value is too low then, it is likely that this extremum is generated by a strip shaped object or by an object that is smaller than the one we are looking for. If this value is high then the object in that position is round and it has a size that fits the size of our target.

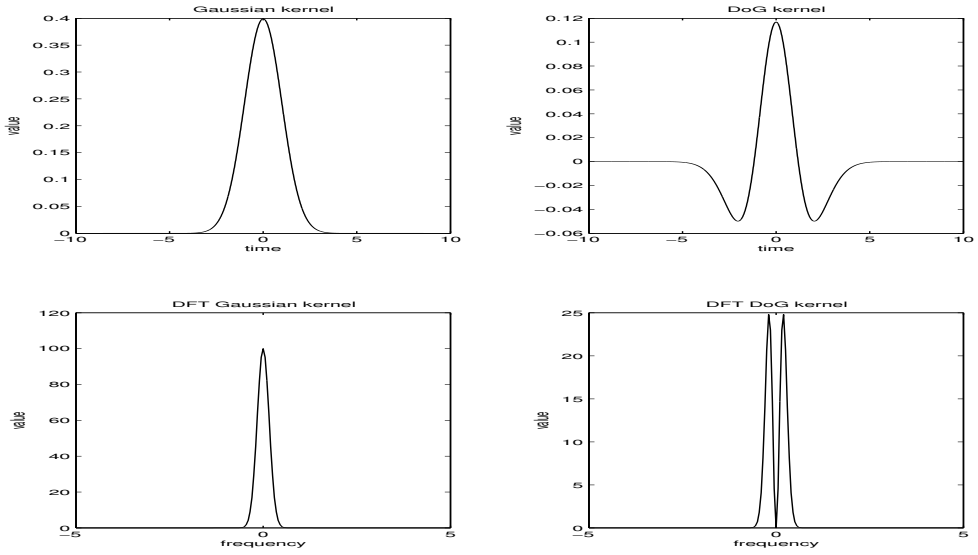

Figure 5.3: First row: basic kernels, namely Gaussian kernel and the equivalent kernel of the whole system. Second row: DFT of previous kernels.

We run experiments on database of pollen particles captured by air sampler machine. The ROC curves are shown in Figure 5.5. Each ROC is drawn for many values of the sample frequency. Because we are considering a set of values also for σ we have a family of curves. For example, with sample frequency equal to 12 and σ equal to 8 we are able to detected nearly 90% of pollen grains with 1000% of false alarms.

We observe that the previous evaluation is quite optimistic because in these

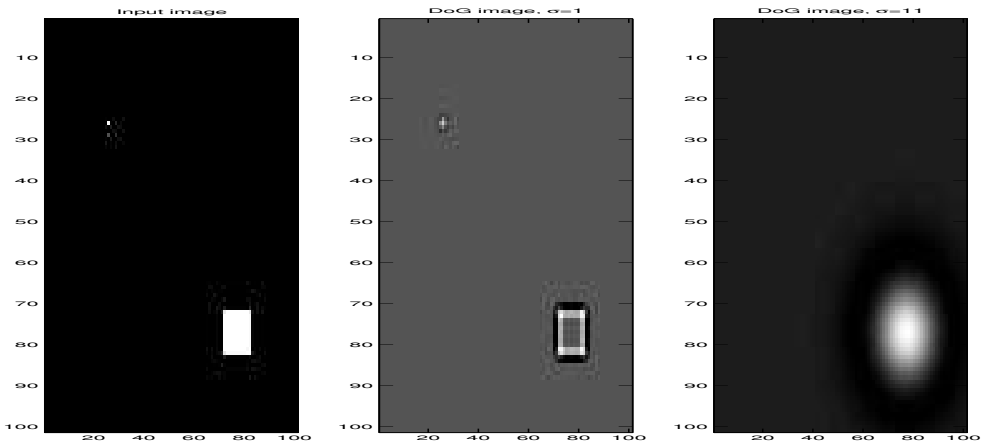

Figure 5.4: This example shows how the choice of scale σ is related with the dimension of objects of interest. The first image has a little blob of 1 pixel in the upper left corner and a larger one of 10 pixel diameter in the lower right corner. The second image shows a good peak in the position of the smaller blob, σ was chosen equal to 1. The third image shows a good peak in the position of the larger blob, σ was chosen equal to $8\sqrt{2}$.

experiments we kept the size of patches constant. The classifier needs patches tightly centered on the object because around it there are other particles that can change the values of our features. This was confirmed when we tried to classify these detected patches because we achieved poor results. Thus, we should take into account additional errors for the necessary operation of box to object adaptation.
Moreover, in the previous experiment we used a square box of side 200 pixels because the biggest pollen, namely pine, has these dimensions. On the other hand, most of pollen grains can be bounded by a box of side 50 pixels. Then, it is likely that we had some matches by chance. Because our boxes are quite big and we admit some overlap between them, these patches may give a match even if the interest point is not on a pollen but in some point near it.

5.2 Morphological detector

This detector is based on morphological operations on the gray level image like: edge detection, dilation, erosion, opening, closing. The need to adapt the size of the boxes around objects, (see previous section), encouraged us to try this new method.

We now describe the main operations involved. Given an image we make a conversion to normalized[1] gray level values and then,

1. we compute the edges applying "canny" edge detector and we get a binary image

[1] After the normalization the background mean is equal to 0 and the minimum value is -1.

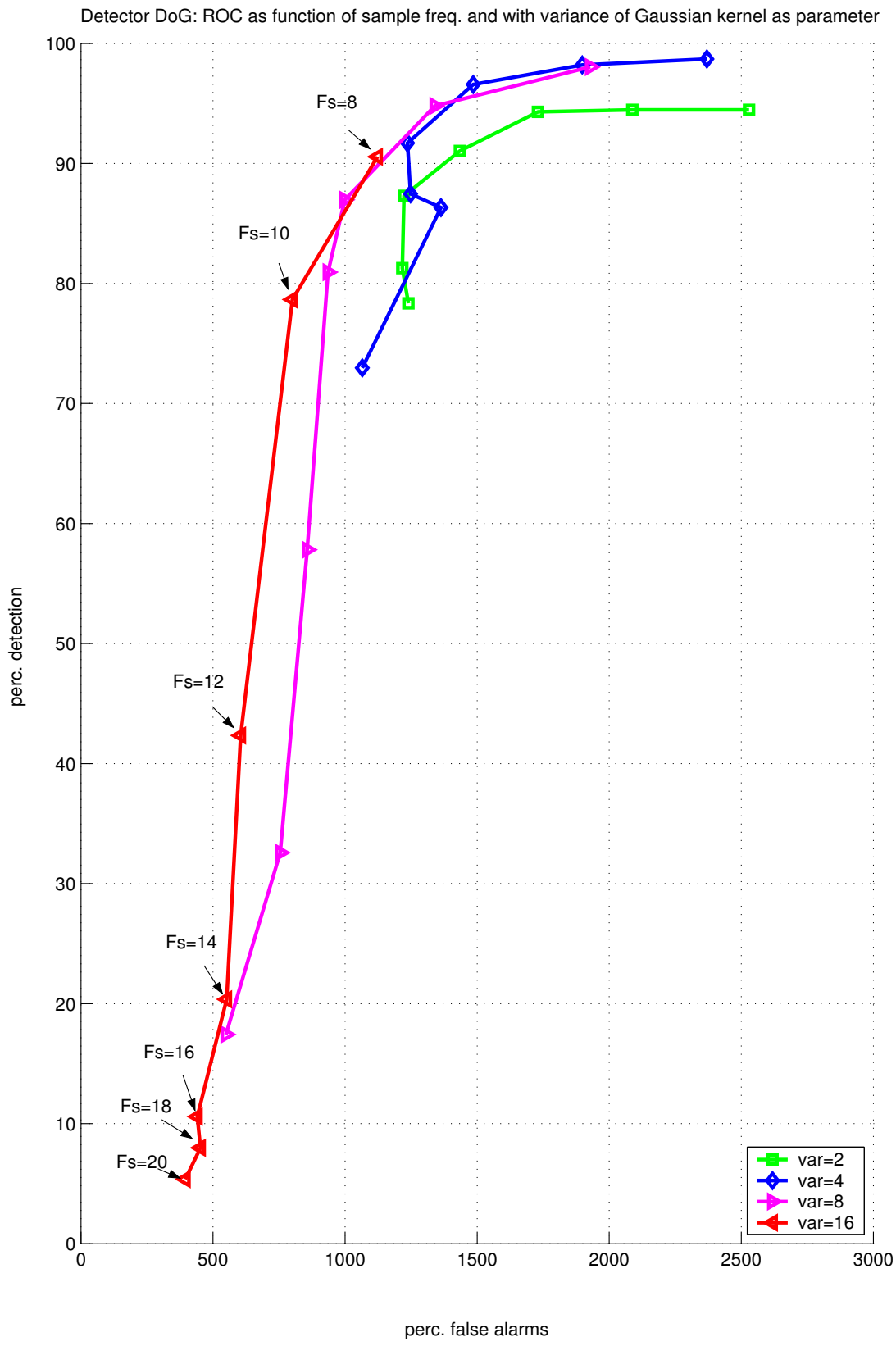

Figure 5.5: ROC curves for detector using DoG.

2. we make 4 dilation with a disk of radius 1 pixel
3. we fill the holes
4. we label the regions and compute a mask: a region is kept if the following conditions are satisfied
   - its area is bigger than a threshold, *ThresAm*
   - the ratio between major and minor axis of ellipse fitting the region is less than a threshold, *ThresAx*
   - the mean of gray values that in the original image fall inside the region is between two thresholds, *ThresMeanL* and *ThresMeanH*
5. we make 2 closing with a disk of radius 1
6. we make 1 dilation with a disk of radius 1
7. we compute a new mask applying the same tests of point 4
8. we make 2 closings and 1 opening with the same disk of radius 1
9. we fill the holes
10. we compute a new mask based on the previous one taking only the regions that satisfy the following tests:
    - area must be between thresholds, *ThresAm* and *ThresAM*
    - the ratio between major and minor axis of ellipse fitting the region is less than a threshold, *ThresAx*
    - the mean of gray values that in the original image fall inside the region is between two thresholds, *ThresMeanL* and *ThresMeanH*
    - the ratio between the area of the region and its bounding box must be grater than threshold *ThresExt*

These series of operations were found experimentally. However we can find some justifications for the tests done to select good regions. No pollen is too dark or too bright (see thresholds *ThresMeanL* and *ThresMeanH*), is too big or too small (see thresholds *ThresAm* and *ThresAM*), is too elongated (threshold *ThresAx*) or U-shaped (threshold *ThresExt*).

In Figure 5.6, Figure 5.7 and Figure 5.8, you can see the operations involved in the mask computation, the regions found and the patches that will be sent to the classifier.

We show in Figure 5.9 ROC curves drawn varying one threshold each time and keeping to default values the other parameters. These curves are computed taking more than 70 images with 236 pollen grains.

We run a last experiment with a choice for these thresholds inspired by the previous ROC curves, see Table 5.1, and we achieved the result in Table 5.2.

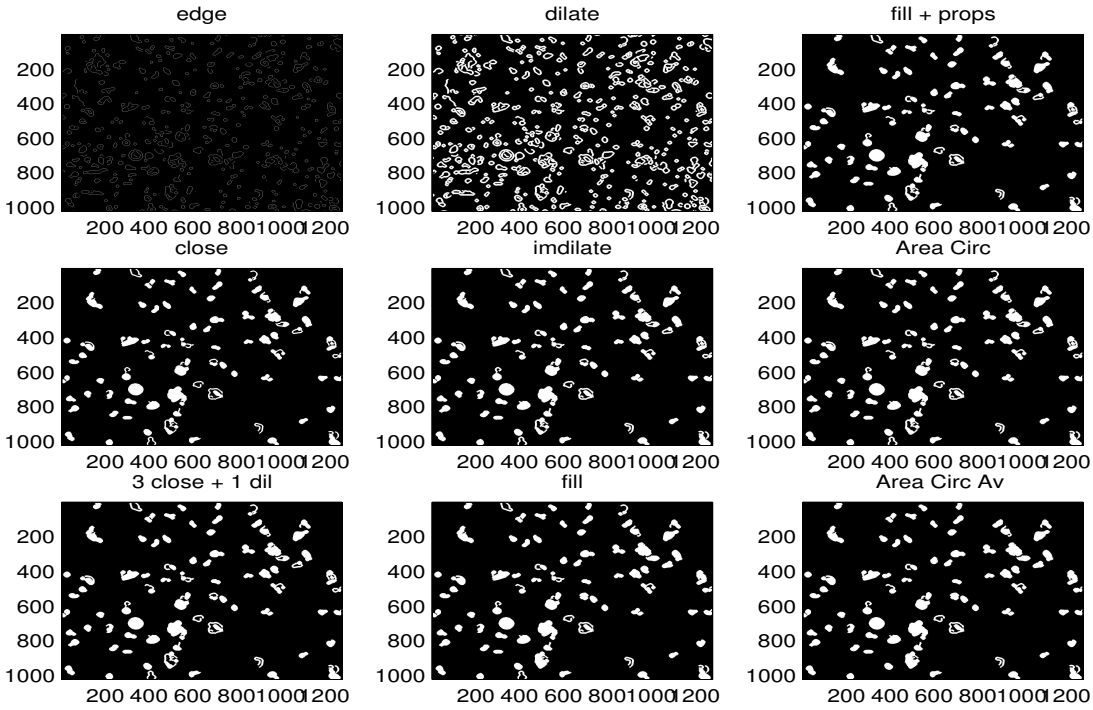

Figure 5.6: Masks and morphological operations computed by morphological detector.

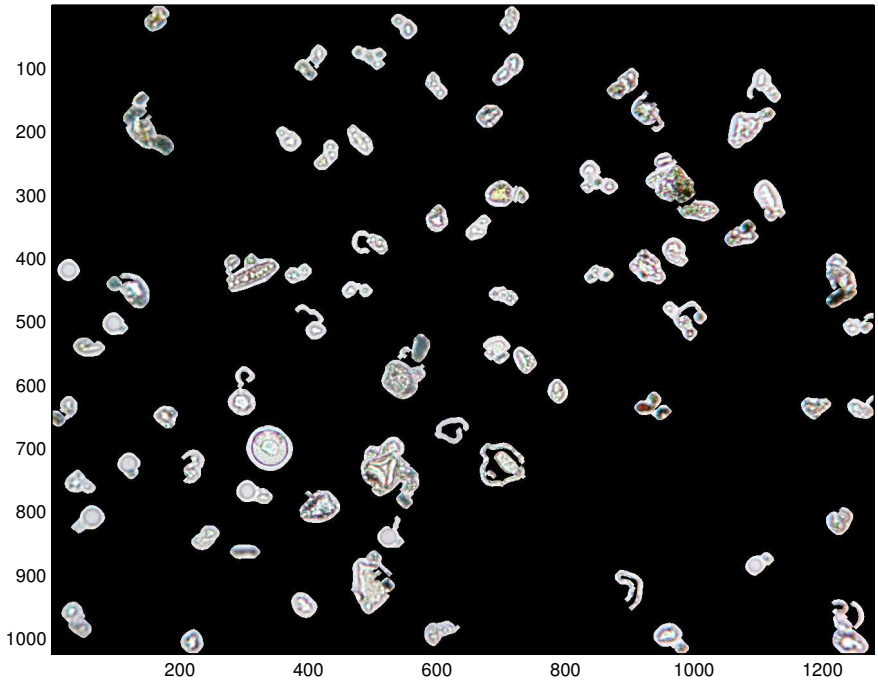

Figure 5.7: Original image with mask superimposed.

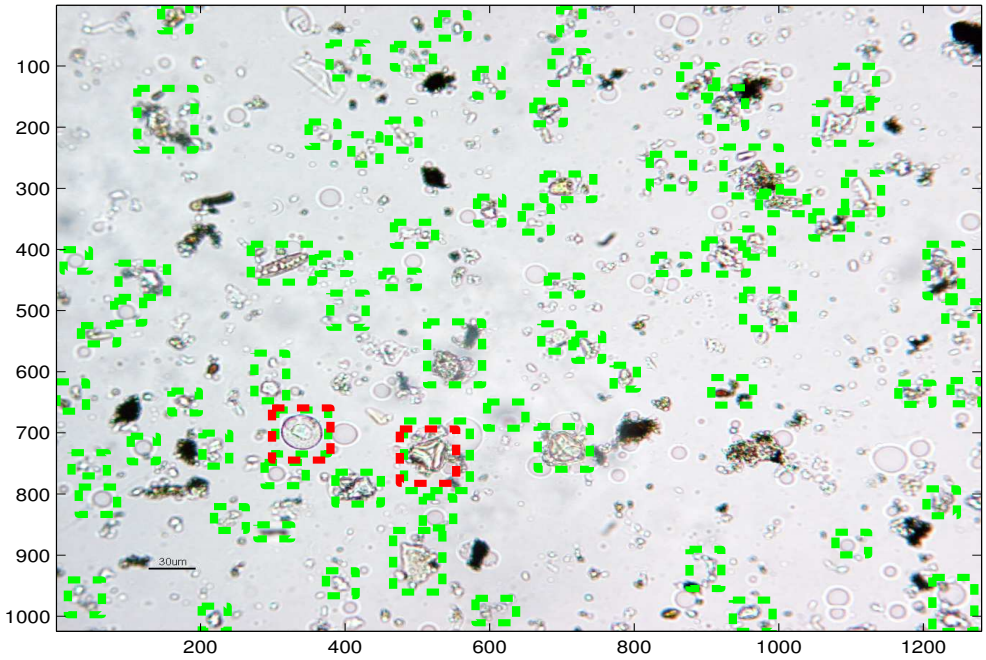

Figure 5.8: Original image with boxes automatically detected by our algorithm (green) and by the expert (red).

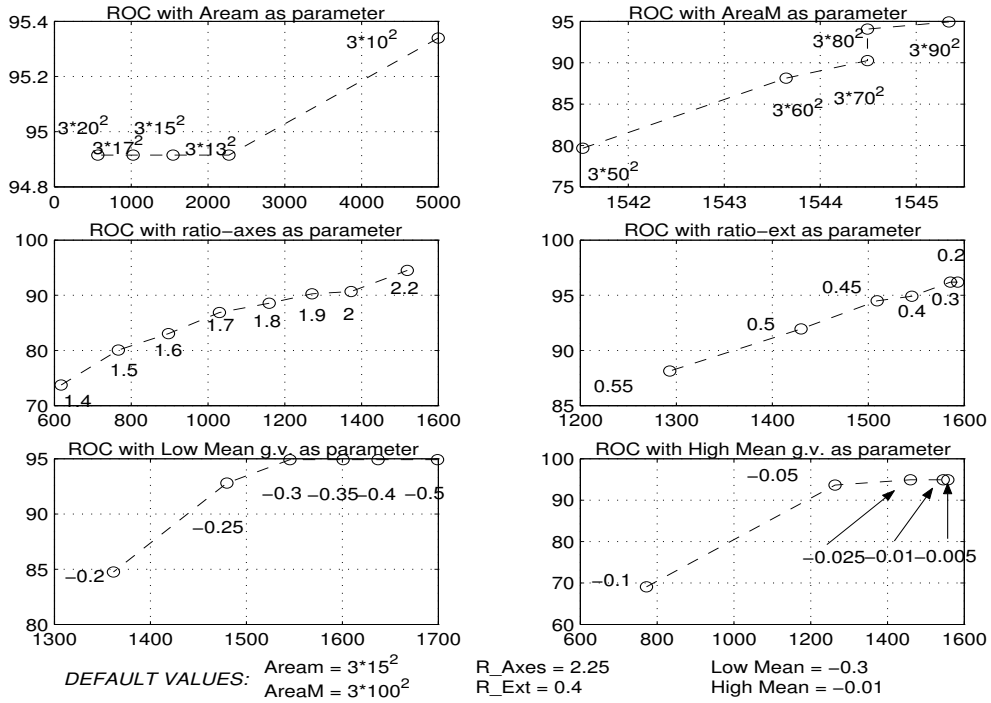

Figure 5.9: ROC curves of morphological detector.

The performance is quite good and promising. The worsening when considering the full data set may be caused by a different kind of preparation of slides (the collection of images in our database took 4 months and some adjustment was done) and to the average smaller number of pollen particles per image in the other part of database.

parameter	*value*
ThresAream	$3 * 17^2$
ThresAreaM	$3 * 80^2$
ThresExt	0.4
ThresAx	2.2
ThresMeanL	-0.3
ThresMeanH	-0.025

Table 5.1: Final choice of parameters in morphological detector.

performance	*71 images / 236 pollens*	*299 images / 562 pollens*
perc. detection	93%	87%
perc. false alarms	956%	1400%

Table 5.2: Performance of morphological detector

This detector is able to find pollen particles with a very high probability and to do a good segmention of these particles (see chapter 8). Its main disadvantages are:

- slowness because all morphological operations are made on the image with the original resolution
- high customization, this detector is likely not suitable to detect other kinds of particles

Chapter 6

Feature extraction

In order to recognize an object in an image, it must be extracted some kind of measurements from it. These values should express the characteristics and all the information contained in the image. Moreover, we have to look for the smallest set of values with these good properties in order to speed up the recognition and to achieve more reliability. This combination of input data is called feature and it is based on some understanding of the particular problem being tackled or by some automatic procedures, [6]. It is the heart of the classification system. If the features extracted are not representative of input images, then, no classifier will be able to do a good job.

In this chapter, we describe two different kinds of feature. The first one, is based on the research of Schmid et al. [9]. The latter one is derived from a work of Torralba et al. [28], in which they aim to discriminate between scenes containing man-made objects and scenes with natural objects. In the next chapter, we will show the very good results of classifiers using these two sets of features.

6.1 Local Jets

In [9], the problem of matching an image in a large data set was addressed. In this method, from each interest point found in a image (using Harris' detector) a set of local gray-value invariants were computed. Our features are based on these invariants, originally studied by Koenderink et al. [17].

We want to extract from each image pixel a set of values, which are invariants with respect to shift and rotation. For example, we aim to acquire the same measurements from two images with the same rotated and shifted bacterium. Furthermore, we want to get the same values when the same object is at different distance from the camera, property referred as *scale invariance*. Even though we are not interested in specific object recognition, the scale, shift and rotation invariance is important in our classification task. With this kind of features, we are able to cluster together the measurements of images belonging to a certain class because we acquire the same measurements, no matter the position and the orientation of the cell and these values are robust against little variations in size.

Let be $I(x, y)$ an image with spatial coordinates x and y. We define *local jet* of order N the convolution of image I with the derivatives with respect to $\overbrace{(x, \cdots, y, \cdots)}^{N \text{ times}}$ of a Gaussian kernel with standard deviation σ. We indicate these local jets with $L_{i_1 \cdots i_n}$, $i_k \in \{x, y\}$. The subscripts refer to the kind of Gaussian kernel derivation. Note that the convolution of I with a derivative of Gaussian kernel is equal to the convolution of Gaussian kernel with the same derivative of I.
In order to obtain invariance with respect to shifts and rotations, linear (or more precisely a differential) combinations of local jets are computed. Our set of invariants is limited to 9, that is to a combination of third order derivatives. These invariants are[1]:

$$\begin{aligned}
I_0 &= I \\
I_1 &= L_x^2 + L_y^2 \\
I_2 &= 2L_xL_{xy}L_y + L_x^2L_{xx} + L_y^2L_{yy} \\
I_3 &= L_{xx} + L_{yy} \\
I_4 &= L_{xx}^2 + L_{yy}^2 + 2L_{xy}^2 \\
I_5 &= L_{xxx}L_y^3 - L_{yyy}L_x^3 + 4L_{xyy}L_x^2L_y - 4L_{xxy}L_xL_y^2 \\
I_6 &= L_{xxy}L_y^3 - L_{xyy}L_x^3 + L_{xxy}L_x^2L_y - L_{xyy}L_xL_y^2 \\
I_7 &= L_{xyy}L_y^3 - L_{xxy}L_x^3 + L_{xxx}L_yL_x^2 - L_{yyy}L_xL_y^2 + 2L_{xxy}L_xL_y^2 - 2L_{xyy}L_x^2L_y \\
I_8 &= L_{xxx}L_x^3 + L_{yyy}L_y^3 + 3L_{xxy}L_x^2L_y + 3L_{xyy}L_xL_y^2
\end{aligned} \tag{6.1}$$

In order to deal with scale changes, these 9 invariants are computed at different scales. At each stage a blurred image (with a Gaussian kernel) is considered as starting point to derive the invariant images. In our experiments, we considered 4 scales that is, we compute invariants using the original image, its blurred version, the blurred version of this last version and so on for another stage. Totally, given an image we build a stack with $9 \times 4 = 36$ images. Figure 6.1 shows an example of this images of invariants using synthetic data: impulse (11x11 pixels) in first and second row, square and rhombus (100x100 pixels) in third, fourth and fifth, sixth row respectively; the gray level values are (approximately) proportional to the invariants values. Figure 6.2 shows all the 36 invariants for a bacterium image.

Till now, we have followed the same approach of [9] to extract from pixels feature vectors. We now introduce a new stage that is, we apply some non-linearities.
Given an image of invariants, we compute the background mean from the border (a ten pixel wide frame) and we split the image in three derived images: the positive and negative part and the absolute value with respect to the background

[1]The first invariant is the average luminance, the second one is the square of the gradient magnitude, the fourth one is the Laplacian.

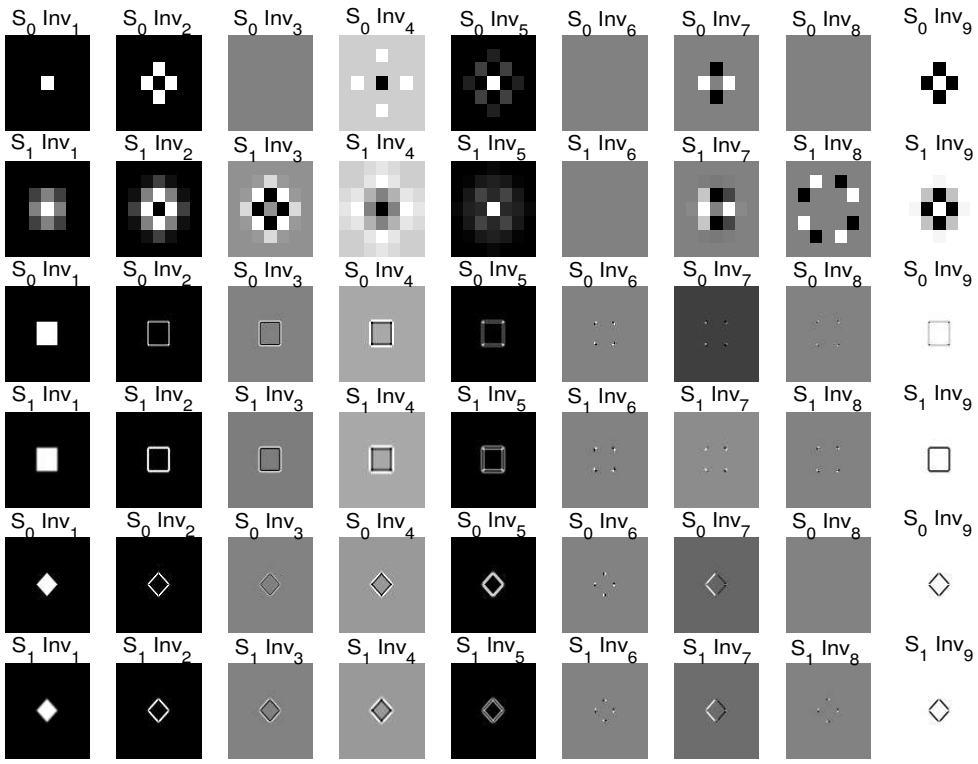

Figure 6.1: Invariants at scale 0 and 1 for synthetic data: impulse (11x11 pixel image), square and rhombus (100x100 pixel image). Note that some asymmetries are due to the approximation used to represent a value in gray-level and the rotation of the square in the rhombus is not perfect due to the poor resolution used.

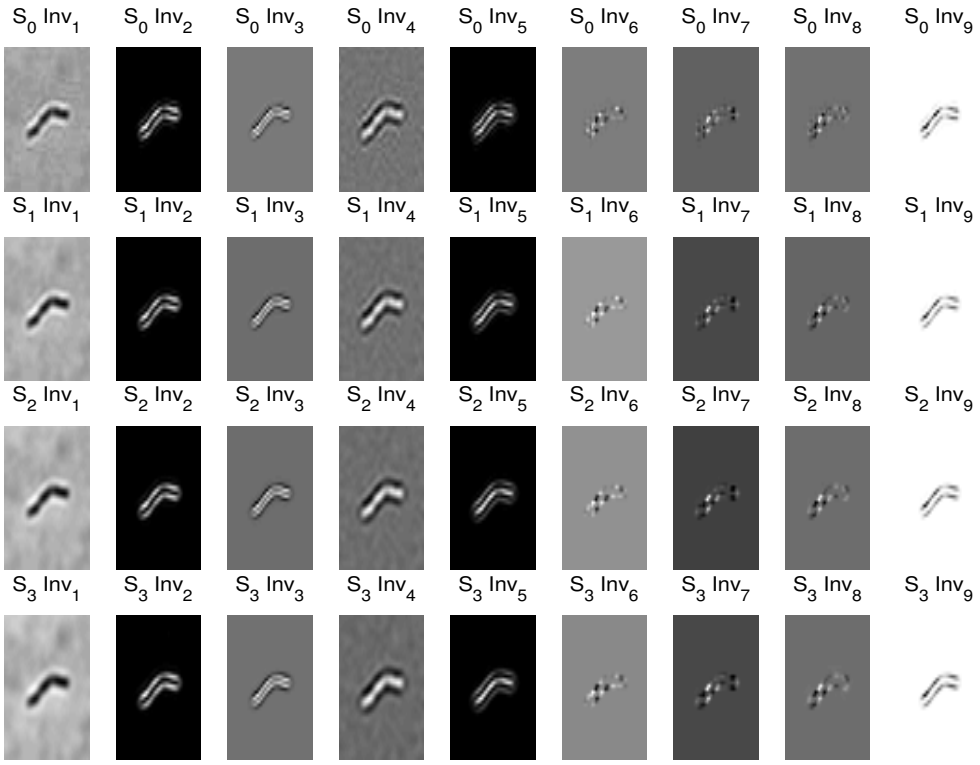

Figure 6.2: Example of invariants at scale $[0, \cdots, 3]$ for an image of bacterium.

mean. Thus, each image gives 36 images of invariants that are splitted in 108 images thanks to this method.
Finally, we make an average of all the pixel values in each of the 108 planes and we get from each image a single feature vector with 108 components.

Just to have an idea of how much these features are able to separate our particles, consider Figure 6.3. Here, we have taken only 100 images from each of two pollen categories and we have extracted features with only two components (without non-linearity application). However, the separation between the data is already quite good.

We found experimentally that the applications of these non-linearities boosts the performance of the classifier. For example, when we trained the system on the first 500 images of each class of urine database and we did not apply the nonlinearities, we achieved an error rate of 18%. When we applied also the nonlinearities, the error rate decreased to 12%.

6.1.1 Decreasing the dimensionality

In training, we aim to model the distribution of feature vectors belonging to all the images of a certain class with a mixture of Gaussians (MoG) or with support vector machines (SVM) (see par. 7.1, 7.4). However, it is not possible to

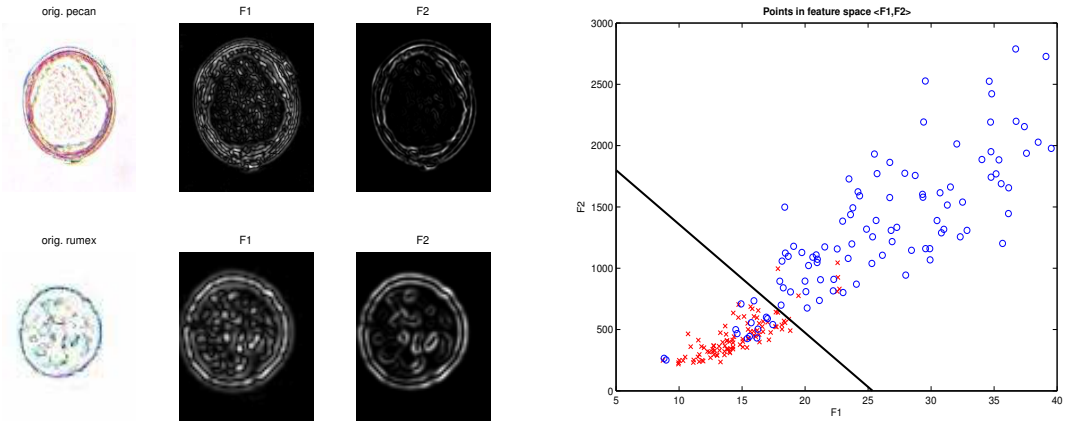

(a) (b)

Figure 6.3: (a) Left column: two kinds of pollen grains, pecan and rumex. Central and right columns: processing on previous images in order to get from each image a feature vector with two components. (b) Example of classification: points in feature space for pecan and rumex pollen, cross and circle respectively. A linear classifier is able to reach an error rate of about 15%.

work in a 108 dimensional feature space because the number of parameters grows very quickly with the space dimensions. For example, in Table 6.1 you can find these relations as a function of the choice of covariance matrix structure and as a function of the number of components in MoG.

	SPHERICAL	DIAGONAL	FULL
nr. param.	$N(D+1)+N-1$	$2ND+N-1$	$N(D+\frac{D(D+1)}{2})+N-1$

Table 6.1: Number of parameters in MoG using N components in a D dimensional feature space as a function of the covariance matrix structure.

For instance, if $D = 108$ and $N = 2$ then, we should estimate $220, 433, 11989$ parameters in accordance to the chosen covariance matrix structure. On the other hand, a common rule of thumb says that you need at least 3 or 4 points to estimate a single parameter. Since our database has not a so huge number of images we have to reduce the dimension of feature space.

In order to reduce the feature space dimensionality we could apply PCA [16] [6]. Experimentally, we found that linear discriminants analysis works better than PCA. Particularly, given the whole set of training feature vectors we compute Fisher's Linear Discriminants (FLD) [6] [23].

We now introduce this technique. Suppose for simplicity to have data $\boldsymbol{x} \in \mathbb{R}^D$ belonging only to two classes C_1 and C_2. We want to find the vector $\boldsymbol{w}$ such that the projected data

$$y_n = \boldsymbol{w}^T \boldsymbol{x}_n \tag{6.2}$$

are optimally separated. The mean vectors of the two classes are

$$\boldsymbol{m}_1 = \frac{1}{N_1} \sum_{n \in C_1} \boldsymbol{x}_n \qquad \boldsymbol{m}_2 = \frac{1}{N_2} \sum_{n \in C_2} \boldsymbol{x}_n \tag{6.3}$$

where N_i is the number of items in class i-th.
Then, we define

$$\begin{aligned} m_k &= \boldsymbol{w}^T \boldsymbol{m}_k \\ s_k^2 &= \sum_{n \in C_k} (y_n - m_k)^2 \end{aligned} \tag{6.4}$$

Fisher's discriminants maximize a function which is in the two-class problem,

$$\frac{(m_2 - m_1)^2}{s_1^2 + s_2^2} \tag{6.5}$$

that is, we are trying to maximize the distance between the means of the projected clusters and minimize the spread of the projected data. While PCA seeks the sub-space that best *represents* the data, FLD seeks the sub-space that maximizes the *separability* between the classes.
The generalization of FLD to several classes follows the same reasoning. It turns out that if you have K classes you can have no more than $K-1$ directions where to project the data. For example, if we think to work with the 12 categories of urine database, we should have the constraint to reduce the feature space dimension from 108 to less than 12. In order to reduce the feature space dimensions without any constraint, we split randomly the data of each class in a proper number of sub-categories [2].

6.2 Image and Power Spectrum Principal Components

We describe a feature extraction based on principal component analysis (PCA), [16] [6].
Given data in a N dimensional space, the goal of PCA is to find a D dimensional subspace such that the projected data are the closest in L_2 norm (mean square error) to the original data. This means that we are looking for the subspace which gives the best *representation* of the original data. This subspace is spanned by the eigenvectors of the data covariance matrix having the highest corresponding eigenvalues. Often the full covariance matrix can not be reliably estimated from

[2] We tried also to divide each cluster applying *k-means* algorithm [6] and estimating a MoG but without any meaningful improvement.

the number of example available, but the approximate highest eigenvalue basis vectors can be computed using singular value decomposition (SVD). Thus, if Σ is the covariance matrix of the data, its SVD decomposition is

$$\Sigma \stackrel{svd}{=} USV^T \tag{6.6}$$

where if $\Sigma \in \mathbb{R}^{N\times N}$, then $U \in \mathbb{R}^{N\times N}$, $V \in \mathbb{R}^{N\times N}$ and $UU^T = I$, $VV^T = I$. S is a diagonal matrix with the elements on the diagonal (the singular values) in descending order. The first columns of U are the eigenvectors with the highest eigenvalues and can be used as basis for the original data.
In our specific case, let be $i(x, y)$ the intensity distribution of the image along spatial variables x and y with $x, y \in [1, N]$. Let be $\boldsymbol{i}$ the values of image pixels rearranged in a column vector, then the covariance matrix is $\Sigma = E[(\boldsymbol{i}-\boldsymbol{m})(\boldsymbol{i}-\boldsymbol{m})^T]$ with $\boldsymbol{m} = E[\boldsymbol{m}]$. If we call image principal components IPC_n the eigenvectors of Σ (computed by singular value decomposition) and $IPC_n(x, y)$ the same eigenvectors reshaped into a matrix $N\times N$, then we can write the following decomposition,

$$i(x, y) = \sum_{n=1}^{P} v_n IPC_n(x, y) \tag{6.7}$$

with $P \leq N^2$ and v_n the coefficients used for describing the image $i(x, y)$ in this new basis. Obviously, v_n is the projection of the image along the direction given by IPC_n.
Figure 6.4 shows 36 IPCs (with the highest corresponding eigenvalues) computed from the first 500 images of each class belonging to the urine database. In our experiments we used always less than 10 IPCs and you can note from Figure 6.5 that the first components are the most important in the data representation. Before any computation, we subtract the background mean estimated from the border of the image (a frame 10 pixels wide) in order to normalize the data with respect to the background brightness.

If we compute the discrete Fourier transform (DFT) $I(k_x, k_y)$ of an image, we can approximate its power spectrum with the squared magnitude of I:

$$R(k_x, k_y) = |I(k_x, k_y)|^2 \tag{6.8}$$

with

$$I(k_x, k_y) = \frac{1}{N^2} \sum_{x=0}^{N-1} \sum_{y=0}^{N-1} i(x, y) e^{-j\frac{2\pi}{N}(xk_x+yk_y)} \tag{6.9}$$

and $f_x = k_x/N$, $f_y = k_y/N$ spatial frequencies. The power spectrum encodes the energy density for each spatial frequency and orientation over the whole image. PCA applied to power spectra gives the main components that take into account the structural variability between images.
First, we normalize the power spectrum with respect to its variance for each

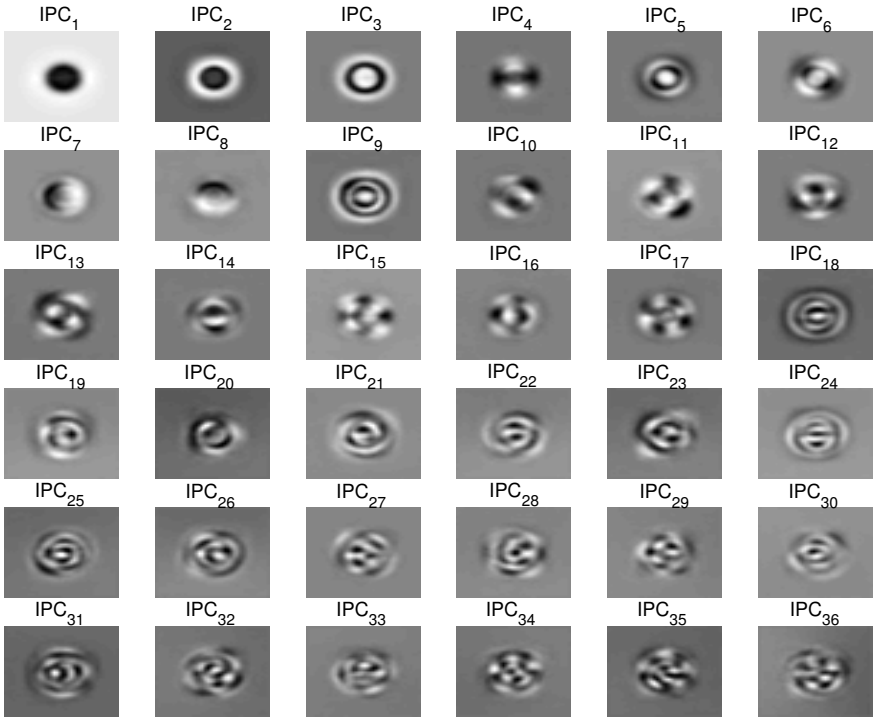

Figure 6.4: First IPCs derived collecting 500 images from each class in urine database. Each image was normalized to a common resolution of 40x40 pixels, thus the space dimension is 1600 and there are 1600 IPCs and singular values.

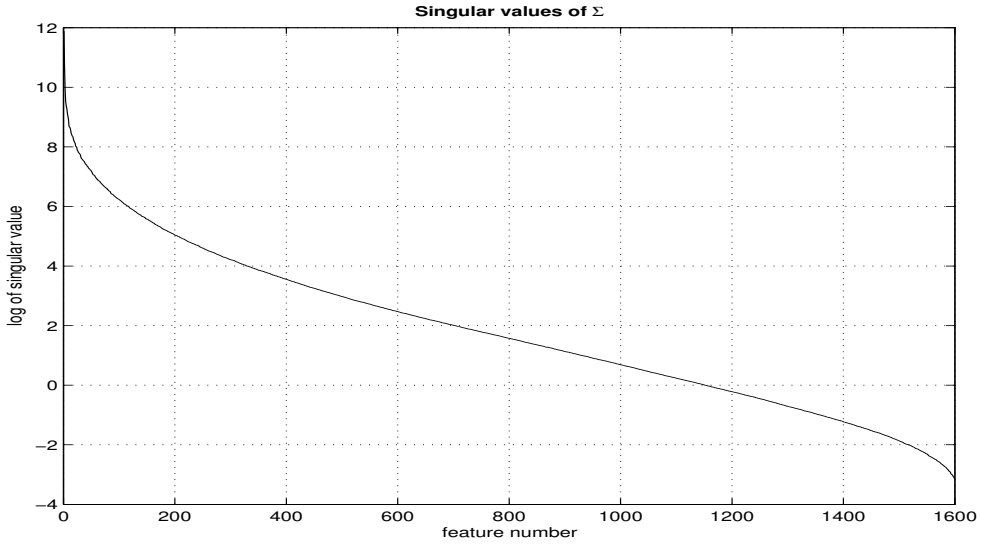

Figure 6.5: The singular values corresponding to IPCs indicate the importance of each component in representing the data.

spatial frequency: $R^*(k_x, k_y) = R(k_x, k_y)/std[R(k_x, k_y)]$, with $std[R(k_x, k_y)] = \sqrt{E[(R(k_x, k_y) - E[R(k_x, k_y)])^2]}$. Then, we apply PCA as done before for the image, we find the spectral principal components (SPCs) and we decompose the normalized power spectrum in

$$R^*(k_x, k_y) = \sum_{n=1}^{P} u_n SPC_n(k_x, k_y) \tag{6.10}$$

Figure 6.6 shows the SPCs (with the highest corresponding eigenvalues) computed from the first 500 images of each class belonging to the urine database.

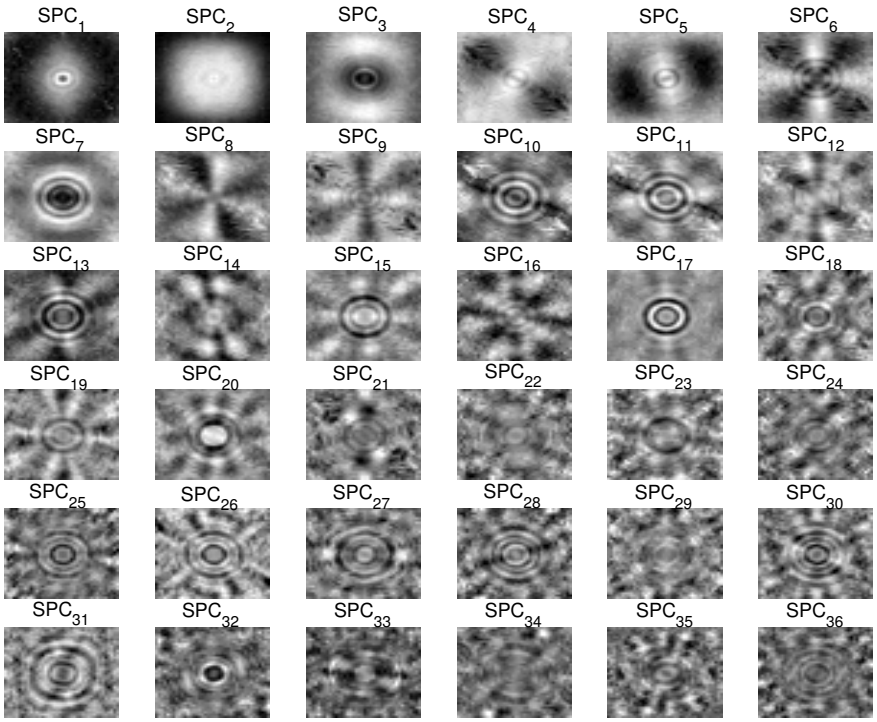

Figure 6.6: First SPCs derived collecting 500 images from each class in urine database. Each image was normalized to a common resolution of 40x40 pixels.

Till now, we have described the basic approach as presented in [28]. In our research, we added a new step.
After the normalization of the image with respect to the background mean that makes this mean equal to zero, we split the image in three derived images: the first one is its positive part I^+, the second one its negative part $I^-$and the third one the absolute value I^a. This operation is equivalent to the application of three non-linear functions that are selective of high, low and mid-range responses. Then, we apply for each of these derived images the PCA and we get IPC_+, IPC_-, IPC_a. A set of these principal components are shown in Figure 6.7 and are computed from the same data used to calculate the basis shown in Figure 6.4.
It is experimentally proved that the classification is improved when this splitting

is done; evidently, particles belonging to different categories behave differently with respect to this operation. Note that the split in positive, negative and absolute value parts can be done very efficiently. We are adding complexity only in training stage because we double the number of PCA required (from two to four).
With this trick, we decrease the error rate from nearly 19% to 16% with reference to the classification of urine database.

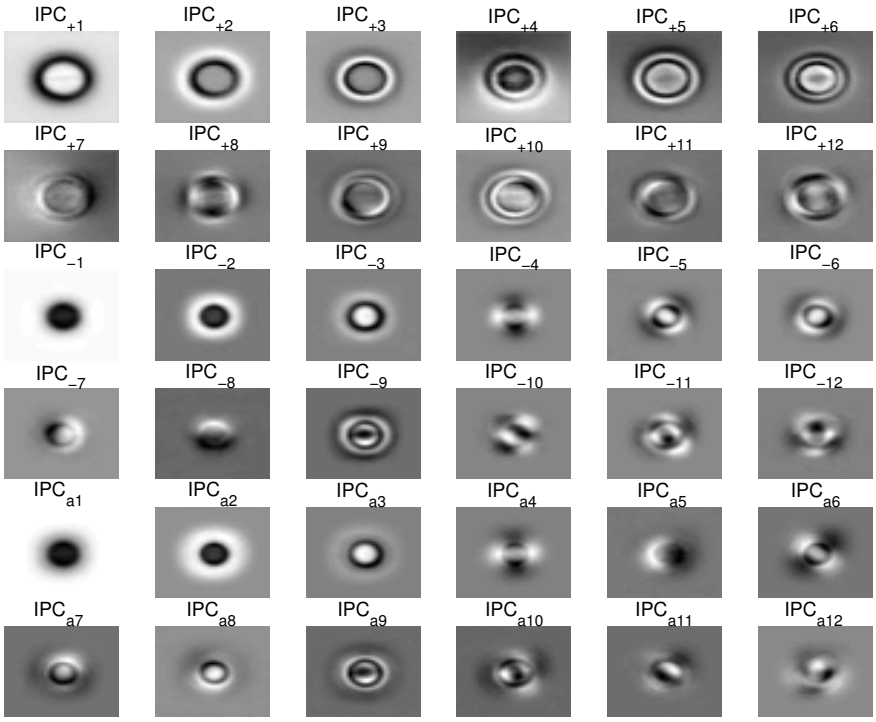

Figure 6.7: First 12 IPC_+, IPC_-, IPC_a derived collecting 500 images from each class in urine database. Each image was normalized to a common resolution of 40x40 pixels.

If we consider the first N_1^i,N_2^i,N_3^i,N^s coefficients computed by the projection of I^+ along IPC_+, I^- along IPC_-, I^a along IPC_a and R^* along SPC we get a feature vector from each image

$$\boldsymbol{f} = [v_{11}, \cdots v_{1N_1^i}, v_{21}, \cdots v_{2N_2^i}, v_{31}, \cdots v_{3N_3^i}, u_1, \cdots u_{N^s}] \tag{6.11}$$

where v_{ij} is the projection of the image I^i along j-th IPC_i for $i \in \{+, -, a\}$.

How do we choose values for N_1^i, N_2^i, N_3^i, N^s? In preliminary experiments, we found that the nearly same performance can be achieved considering

$$\begin{aligned} N_1^i &= N_2^i = N_3^i \\ N^s = 3N_j^i, &\qquad \text{for } j = 1, 2, 3 \end{aligned} \tag{6.12}$$

and applying Fisher's linear discriminants to the whole set of principal components in order to reduce the dimension of feature space to $N = N_1^i + N_2^i + N_3^i + N^s$. In the next chapter, we will only consider the first option because of its simplicity.

6.3 Interpretation

The two sets of features described in this chapter are similar, in spite of the different techniques used to compute them. Features based on PCA give the average information content of the signal at frequencies higher and higher when it is considered the projections on eigenvectors with smaller and smaller eigenvalues. Similarly, features based on invariants give the global amount of information at different bands when it is taken the average of these invariants at different scales. This is proved experimentally. The implementation of classifiers based on these features skipping the non-linearity application gave nearly the same performance, with an error rate of 20% on the twelve categories of urine database.
The application of non-linearities boosts the performance; in particular, it nearly halves the error rate of classifier using the features based on local jets.

Chapter 7

Classification

Classification is the last stage of a recognition system. Given a patch with - hopefully - one centered object, a feature vector is extracted from the image. In training, the system learns how to distinguish among features of images belonging to different categories. In test phase, according to the test image feature, a decision is made. If the object in the image is considered a particle of interest, then its class is also identified, otherwise it is discarded because the measurement does not match any training model.

This chapter begins with the description of training and test stage of a Bayesian classifier using Gaussian mixture models. This classifier gave the best performance with an error rate of 7.6% on urine database and 10.2% on "pure" pollen database.
However, following sections present slightly different approaches. First, two ways of combining both kinds of features already presented in the previous chapter will be discussed. Second, a customized version of AdaBoost.M1, an algorithm to boost the performance of any classifier, will be defined. Finally, a classifier based on support vector machines (SVM) will be introduced.

This chapter will conclude with experiments to optimize the system and some final experiments covering all the data set.

7.1 Mixture of Gaussians

This classifier is the simplest and the most powerful system we developed. With the only exception of the classifier using SVM, all the other classifiers are based on it.

We now describe its two main stages: training and test.

7.1.1 Training

In training phase, we can model the distribution of feature vectors belonging to a certain class with a mixture of Gaussians (MoG) [6]. If the number of categories is K, then we have to estimate K MoGs. The estimation is done

applying expectation maximization (EM) algorithm [6].
Generally, our aim is to estimate the *class-conditional distribution* $f(\boldsymbol{x} \mid C_k)$, that is the probability density function (pdf) of the data, given our knowledge that they belong to a certain class C_k. In order to simplify the notation we now make implicit the class condition. However, it is a straightforward generalization to consider it.
The mixture model decomposes the pdf of the data $f(\boldsymbol{x})$ in a linear combination of M component densities $f(\boldsymbol{x} \mid j)$ in the form

$$f(\boldsymbol{x}) = \sum_{j=1}^{M} f(\boldsymbol{x} \mid j) P(j) \tag{7.1}$$

The mixing parameters $P(j)$, also called *priors probabilities*, satisfy the constraints

$$\sum_{j=1}^{M} P(j) = 1 \tag{7.2}$$

$$0 \leq P(j) \leq 1 \tag{7.3}$$

moreover, the conditional probability density functions verify

$$\int f(\boldsymbol{x} \mid j) d\boldsymbol{x} = 1 \tag{7.4}$$

An important property of mixture models is that they can approximate any continuous pdf to arbitrary accuracy with a proper choice of number of components and parameters of the model.
In our system, we use mixture of Gaussians. Thus, we have to choose the number of components and the structure of their covariance matrix. The best choice of parameters is found experimentally. We make use of a package for MATLAB called NETLAB in which there are functions to estimate the MoG by the application of EM algorithm.

The goal of training is to build for each class a model of the distribution of the feature vectors belonging to the class images. This model is achieved using MoG and it describes the pdf of the class feature vectors.

7.1.2 Test

Given a test image, we compute its feature vector $\boldsymbol{f}$. Then, we apply the Bayes' rule.
We are interested on the probability of the class C_k given the test data $P[C_k \mid \boldsymbol{x}]$, because we want to apply the following decision rule:

$$x \mapsto r(x) = argmax_k P[C_k \mid \boldsymbol{x}] \tag{7.5}$$

The extension of Bayes' rule to continuous conditions assure that

$$P[C_k \mid \boldsymbol{x}] = \frac{f(\boldsymbol{x} \mid C_k)P[C_k]}{f(\boldsymbol{x})} = \frac{f(\boldsymbol{x} \mid C_k)P[C_k]}{\sum_{j=1}^{M} f(\boldsymbol{x} \mid C_j)P[C_j]} \tag{7.6}$$

where f is pdf and P is probability. So, in hypothesis of equal distribution for the class probabilities, $P[C_k] = 1/K$ for $k = 1, \cdots, K$, we can simplify

$$P[C_k \mid \boldsymbol{x}] = \frac{f(\boldsymbol{x} \mid C_k)}{\sum_{j=1}^{M} f(\boldsymbol{x} \mid C_j)} \tag{7.7}$$

Moreover, we can observe that $\max P[C_k \mid \boldsymbol{x}]$ is obtained for the same k of $\max f(\boldsymbol{x} \mid C_k)$ because the factor $\sum_{j=1}^{M} f(\boldsymbol{x} \mid C_j)$ is constant for all j. The term $f(\boldsymbol{x} \mid C_k)$ is called *likelihood* because it is a conditional probability density function with implicit dependence on the model parameters. Because our decision rule looks for the maximum of this term, it is referred as *maximum likelihood* decision rule.

We also add to this framework a test. When we train, we collect for each class its resolution mean and standard deviation, m_{r_k} and σ_k. Then in test, we compute the likelihood of the test data given the class C_k only if the following condition holds:

$$r \in [m_{r_k} - N\sigma_k, m_{r_k} + N\sigma_k] \tag{7.8}$$

where, r is the resolution of the test image and N is a parameter to be chosen; in our experiments we chose $N = 3$.
This test is mainly done to save time avoiding useless computation. If an image resolution is out of the range of every class, then it is not classified and put in an *unknown* class.

7.2 Combination of features

We will show in the experimental part that the previous classifier using features based on principal component analysis and on local jets gives good results with an error rate below 15% on urine database. In this section, we present two methods to combine these features.
If you look at the confusion matrices of the classifier working with these features (see Figure 7.14 and Figure 7.15), you can notice a certain correlation among misclassifications which suggests dependence between the two kinds of feature.

However, we can simplify the problem of feature combination assuming *independence* between the two sets. If we do not make any hypothesis between these features we have to solve the more general problem of combination of experts' response.

7.2.1 Independence hypothesis

Given an image, we apply the two techniques described in the previous chapter to extract features based on principal component analysis $\boldsymbol{x}_1$ and on local jets $\boldsymbol{x}_2$. In hypothesis of independence between these two vectors, we can write the class conditional density function as

$$f(\boldsymbol{x}_1, \boldsymbol{x}_2 \mid C_i) = f(\boldsymbol{x}_1 \mid C_i) f(\boldsymbol{x}_2 \mid C_i) \tag{7.9}$$

Thus, as we did in the previous section, we look for the maximum likelihood of the test image feature to make a decision and thanks to eq. (7.9), we can write

$$P[C_i \mid \boldsymbol{x}_1, \boldsymbol{x}_2] \text{ is proportional to } f(\boldsymbol{x}_1 \mid C_i) f(\boldsymbol{x}_2 \mid C_i) \tag{7.10}$$

To summarizee, with reference to the classifier using MoG we make two separate trainings using the two set of features and two separate tests. Then, we multiply the class conditional densities and we choose the class with highest value.

7.2.2 Without hypothesis

This approach was suggested by the good performance achieved modeling data with MoG. We now do not make any assumption on features.
We divide the training set into two sets. The first one is used to train separately the classifier using the two different kinds of features and so to get $f(\boldsymbol{x}_i \mid C_j, \theta_n)$, where $\boldsymbol{x}$ is a feature vector and θ_n is the model used. We refer to model as the technique for feature extraction, namely the method based on PCA or local jets. Then, for each image of the second training set we compute the vector

$$(P[C_1 \mid data, \theta_{pca}], \cdots, P[C_1 \mid data, \theta_{lj}], \cdots) \tag{7.11}$$

and we model with a MoG these probability vectors of all the images belonging to each class.

In test, given an image we compute the two feature vectors and the vector of probabilities of eq. (7.11). Then, we make a decision by computing the maximum likelihood of this vector in the last training model.

In this way, we take into account the performance of each classifier and implicitly we give more weight to the "expert's" response with better performance in the given class (even if in test we do not know the true class to which the particle belongs).

The drawback of this method, is that it requires a lot of training data because it needs to build MoG models. Because our data set is quite small, the parameter estimation cannot be very precise and thus, the performance is not improved (see the experimental section).

7.3 Boosting

We studied the multi-class extension of AdaBoost called "AdaBoost.M1", [26] [15].
Given a weak learner, let be X the set of input data and Y the set of the possible labels for the samples in X. The learner receives examples (x_i, y_i), with $x_i \in X$ and $y_i \in Y$. These examples are chosen randomly according to some fixed but unknown distribution P on $X \times Y$. The goal is to learn to predict the label y given an istance x. We assume that the sequence of N training examples is $(x_1, y_1), ..., (x_N, y_N)$. At each iteration or round, the weak learner generates hypothesis which assigns to each istance one of the K possible labels. At the end, the boosting algorithm presents an output hypothesis $h_f : X \to Y$ with lower error rate. It is required that each weak hypothesis has prediction error less than $1/2$[1].
We define for any predicate p, $\vdash p \dashv$ to be 1 if p holds and 0 otherwise.
We summarize the general algorithm in pseudo-code in Figure 7.1.

Let's try to boost the performance of the classifier described in par. 7.1 with reference to the previous algorithm.
We have to decide how to provide our classifier with the distribution $\boldsymbol{p}$ at each round. We could go inside EM algorithm and modify the weights of the sum in the log-likelihood computation. However, it seems simpler to extract from each class set a number of images proportional to the class weight. Note that in this way, $\boldsymbol{p}$ becomes a distribution over the classes and not any more over the single training images. This method has also another drawback because the MoG estimation needs a lot of examples to find convergence. So, we have to reduce the number of training images belonging the best classified categories and on the other hand, to keep a sufficient number for the MoG estimate. Thus, our implementation of AdaBoost.M1 is a slightly different version.

We choose the weights in a way that allows to the worst classified class to train on all the maximum number of images while the best classified class has available a minor number of images; however this number is sufficient for the estimate of parameters in the MoG. In particular, at each round the minimum weight is decreased if the class is still the best classified, while the maximum weight is always equal to the maximum if the class is still the worst classified. We show the pseudo-code of this customized version of AdaBoost.M1 in Figure 7.2.

In the experimental section, we will show that this method is able to achieve a slightly better performance than the one of the basic classifier.

[1]The error-correcting output code technique [25] has not this constraint but it is slightly more difficult. Our classifier has an error rate below 15% and so, this constraint is not a problem.

ALGORITHM AdaBoost.M1

Input:

- sequence of N examples $< (x_1, y_1), ..., (X_N, y_N) >$ with labels $y_i \in Y = \{1, ..., K\}$
- distribution D over the examples
- weak learner algorithm
- integer T specifying the number of iterations

Initialize the weight vector: $w_i^1 = D(i)$ for $i = 1, ..., N$.

DO for $t = 1, 2, ..., T$

1. Set
$$\boldsymbol{p}^t = \frac{\boldsymbol{w}^t}{\sum_{i=1}^N w_i^t}$$
2. Call weak learner, providing it with the distribution $\boldsymbol{p}^t$; get back the hypothesis $h_t : X \to Y$.
3. Calculate the error of $h_t : e_t = \sum_{i=1}^N p_i^t \vdash h_t(x_i) \neq y_i \dashv$.
4. Set $\beta_t = \frac{e_t}{1-e_t}$.
5. Set the new weights vector to be
$$w_i^{t+1} = w_i^t \beta_t^{1-\vdash h_t(x_i) \neq y_i \dashv}$$

Output the hypothesis
$$h_f(x) = arg \max_{y \in Y} \sum_{t=1}^{T} (log \frac{1}{\beta_t}) \vdash h_t(x_i) = y_i \dashv$$

Figure 7.1: Pseudocode of algorithm AdaBoost.M1.

ALGORITHM AdaBoost.M1 customized version

Input:

- sequence of $N = M * K$ examples $< (x_1, y_1), ..., (x_N, y_N) >$ with labels $y_i \in Y = \{1, ..., K\}$
- distribution D over the examples
- classifier
- integer T specifying the number of iterations
- learning ratio l

Initialize the weight vector: $w_k^1 = D(k) = M$ for $i = 1, ..., k$.

DO for $t = 1, 2, ..., T$

1. Call classifier, providing it with w_k^t images for each class; get back the hypothesis $h_t : X \to Y$.
2. Calculate the overall error rate e_t.
3. Set $\beta_t = \frac{e_t}{1-e_t}$.
4. Let be ER_k the error rate for class k and $MER = arg\max_{k \in Y} ER_k$.
   Set the new weight vector to be
   $$w_k^{t+1} = w_k^t \beta_t^{1-ER_k/MER}$$
   Let be $MW = arg\max_{k \in Y} w_k^{t+1}$ and $mw = arg\min_{k \in Y} w_k^{t+1}$, then rescale the weights between $l \times mw$ and MW.

Output the hypothesis
$$h_f(x) = arg\max_{y \in Y} \sum_{t=1}^{T} (log\frac{1}{\beta_t}) \vdash h_t(x_i) = y_i \dashv$$

Figure 7.2: Pseudocode of modified version of algorithm AdaBoost.M1.

7.4 Support Vector Machines

The support vector machine (SVM) approach does not attempt to model the distribution of features but it works directly on them.
Let us start considering the simplest case of a *linear machine* trained on *separable data*, [10] [7]. The training input data are a set of labeled features $\{\boldsymbol{x}_i, y_i\}$, $i = 1, \cdots, l$, $y_i \in \{-1, 1\}$, $\boldsymbol{x}_i \in \mathbb{R}^d$. Suppose we have some hyperplane which separates the positive from the negative examples. The points $\boldsymbol{x}$ which lie on the hyperplane satisfy $\boldsymbol{w} \cdot \boldsymbol{x} + b = 0$, where $\boldsymbol{w}$ is the normal to the hyperplane. Let be d_+ and d_- the shortest distance from the separating hyperplane to the closest positive and negative example respectively. For the linearly separable case, the support vector algorithm looks for the separating hyperplane with the largest *margin*, defined as $d_+ + d_-$. Thus we can write that each training point satisfy:

$$\begin{aligned} \boldsymbol{x}_i \cdot \boldsymbol{w} + b \geq +1, \quad & \text{for } y_i = +1 \\ \boldsymbol{x}_i \cdot \boldsymbol{w} + b \leq +1, \quad & \text{for } y_i = -1 \end{aligned} \tag{7.12}$$

that is,

$$y_i(\boldsymbol{x}_i \cdot \boldsymbol{w} + b) - 1 \geq 0 \ \forall i \tag{7.13}$$

Choosing a proper scale for $\boldsymbol{w}$ and b, we can have points for which the equality in eq. (7.13) holds and $d_+, d_- = 1/\|\boldsymbol{w}\|$; these points are called *support vectors*. Their removal would change the solution and they live in the hyperplanes $H_1 : \boldsymbol{x}_i \cdot \boldsymbol{w} + b = +1, H_2 : \boldsymbol{x}_i \cdot \boldsymbol{w} + b = -1$. No training point falls between them.
It can be shown that in order to find $\boldsymbol{w}$ and b, we have to solve a quadratic optimization problem. Once these parameters are found, given a test point $\boldsymbol{x}$, we simply determine on which side of the decision boundary $\boldsymbol{x}$ lies and assign the corresponding class label.

If the training data are not separable, we have to introduce positive *slack* variables ξ_i, $i = 1, \cdots, l$ in the previous equations which become:

$$\begin{aligned} \boldsymbol{x}_i \cdot \boldsymbol{w} + b \geq +1 - \xi_i, \quad & \text{for } y_i = +1 \\ \boldsymbol{x}_i \cdot \boldsymbol{w} + b \leq +1 + \xi_i, \quad & \text{for } y_i = -1 \\ & \xi_i \geq 0 \forall i \end{aligned} \tag{7.14}$$

Thus, for an error to occur, the corresponding ξ_i must exceed unity, so $\sum_i \xi_i$ is an upper bound on the number of training errors. It can be shown [7] that the quadratic programming problem can be solved introducing a new user defined parameter C in order to assign the desired penalty to errors. An interpretation

of C and support vectors is that only support vectors exert a force on the decision sheet and C is an upper bound on this force.

Because a support vector machine only realizes a linear classifier, non-separable data are projected in a very high dimensional feature space in which the data become separable, and this means that in the original feature space the classifier becomes highly non-linear.
The only way in which training data appear in the optimization problem is in the form of dot products, $\boldsymbol{x}_i \cdot \boldsymbol{x}_j$. Then, we can map the data in another (generally higher dimensional space) H using the function Φ:

$$\Phi : \mathbb{R}^d \mapsto H \tag{7.15}$$

Now, the training depends only on the data through dot products in H, i.e. on $\Phi(\boldsymbol{x}_i) \cdot \Phi(\boldsymbol{x}_j)$. Moreover, we are interested to find a *kernel function* K such that $K(\boldsymbol{x}_i, \boldsymbol{x}_j) = \Phi(\boldsymbol{x}_i) \cdot \Phi(\boldsymbol{x}_j)$ in order to use only a function.
The most powerful and simple kernels are:

- **linear**: $K(\boldsymbol{x}_i, \boldsymbol{x}_j) = \boldsymbol{x}_i \cdot \boldsymbol{x}_j$
- **polynomial** of order p: $K(\boldsymbol{x}_i, \boldsymbol{x}_j) = (\boldsymbol{x}_i \cdot \boldsymbol{x}_j + 1)^p$
- **Gaussian radial basis function** (RBF) of parameter σ: $K(\boldsymbol{x}_i, \boldsymbol{x}_j) = e^{-\|\boldsymbol{x}_i - \boldsymbol{x}_j\|^2/2\sigma^2}$

In Figure 7.3, you find a simple example of binary classification using these kernels for different values of their parameters.

Finally, we have to discuss how to use this algorithm to solve a multiclass classification problem [12][2]: we use *error-correcting output codes* technique.
Each class is assigned a unique binary string of length n called *codeword*. Then, n binary functions are learned, one for each bit position in these binary strings. During training for an example of class i, the desired outputs of these n binary functions are specified by the codeword for class i. New values $\boldsymbol{x}$ are classified by evaluating each of the n binary functions to generate an n-bit string s. This string is then compared to each of the k codewords, and $\boldsymbol{x}$ is assigned to the class whose codeword is closest[3] to the generated string s.

The error-correcting code should satisfy the two properties:

- each codeword should be well-separated in Hamming distance from each of the other codewords
- each bit-position function should be uncorrelated with the functions to be learned for the other bit positions

For our experiments we derived the error-correcting code by T. Dietterich's collection of code matrices [3], see Figure 7.4.

We did not implement SVM algorithm but we downloaded [4] a software in Matlab written by Anton Schwaighofer (2002). Its main features are:

[2]We could apply this method also to AdaBoost algorithm.
[3]In our experiments, we use Hamming distance.

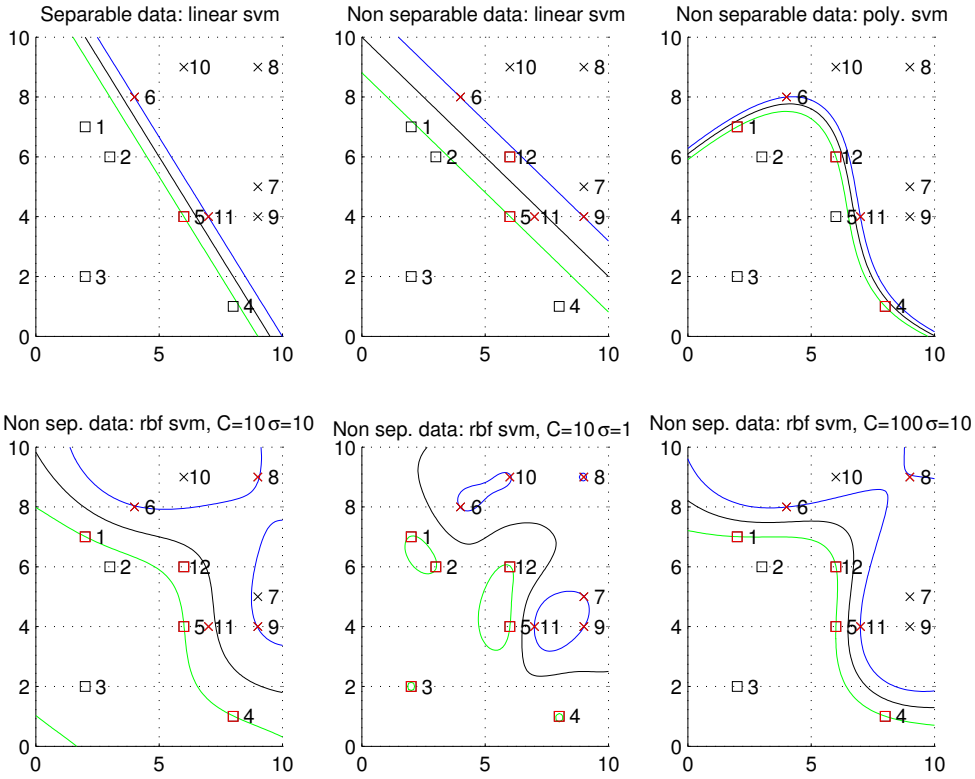

Figure 7.3: Example of classification using SVM for separable and non-separable synthetic data with different choices of kernel. Support vectors are drawn in red. The decision boundary is more shattered for high values of degree of polynomial kernel, low values of σ in RBF kernel, high values of C. A balance between generalization and performance in training set has to be found.

```
*****************************************************************************************************
*                                                                                                   *
*  1 0 1 0 1 1 0 1 1 1 1 1 0 0 1 0 1 0 1 1 1 1 0 0 0 1 0 0 0 1 1 0 0 0 1 0 0 1 1 1 0 1 0 1 1 0 1  *
*  0 1 0 1 1 0 1 0 0 1 0 0 1 0 1 1 0 0 1 0 0 0 0 1 1 1 1 1 0 1 1 1 0 1 1 0 1 0 1 0 0 0 0 1 1 1 1  *
*  1 1 0 1 0 1 1 0 0 0 1 0 1 1 0 0 0 1 0 1 0 0 1 0 1 0 0 1 1 0 1 0 1 0 0 0 0 0 0 1 1 1 1 1 1 0 0  *
*  0 0 1 0 0 0 0 1 1 0 0 1 0 1 0 1 1 1 0 0 1 1 1 1 0 0 1 0 1 0 1 1 1 1 0 0 1 1 0 0 1 0 1 1 1 1 0 0  *
*  0 0 1 1 0 0 0 1 0 1 0 1 1 1 0 1 0 0 0 0 1 0 0 1 1 0 1 1 1 1 1 1 0 0 0 1 0 1 0 1 1 1 1 0 0 0 0 0  *
*  1 1 0 0 0 1 1 0 1 1 1 0 0 1 0 0 1 0 0 1 0 1 0 0 0 0 0 0 1 1 1 1 0 1 1 0 0 1 1 0 1 0 0 0 0 0 0  *
*  0 1 0 0 1 0 1 0 1 0 0 0 0 0 1 1 1 1 1 0 0 1 1 1 0 1 1 0 0 0 1 0 1 0 0 0 1 1 0 1 0 1 1 0 0 1 0  *
*  1 0 1 1 1 1 0 1 0 0 1 1 1 0 1 0 0 1 1 1 1 0 1 0 1 1 0 1 0 0 1 1 1 1 0 0 0 0 0 0 0 0 1 0 0 0 0  *
*  1 1 1 1 1 0 1 1 0 0 1 0 1 0 0 1 1 1 0 0 0 0 1 0 0 1 1 0 0 1 0 1 0 1 1 1 0 1 0 0 1 1 0 1 0 0 0  *
*  0 0 0 0 1 1 0 0 1 0 0 1 0 0 0 0 0 1 0 1 1 1 1 1 1 1 0 1 0 1 0 0 0 0 1 1 1 0 0 1 1 0 0 1 0 0 0  *
*  1 0 0 0 0 0 0 0 1 1 1 1 0 1 1 1 0 0 1 0 1 1 0 0 1 0 1 1 1 0 0 1 1 1 0 1 0 0 1 0 0 1 1 1 0 0 0  *
*  0 1 1 1 0 1 1 1 0 1 0 0 1 1 1 0 1 0 1 1 0 0 0 1 0 0 0 0 1 0 0 0 1 0 0 1 1 1 1 1 0 0 1 1 0 0 1  *
*                                                                                                   *
*****************************************************************************************************
```

Figure 7.4: Error-correction codes used in SVM experiments to solve the multi-class classification problem: 12 classes, codewords with 47 bits.

- Except for the QP solver, all parts are written in plain Matlab.
- Extension to multi-class problems via error correcting output codes is included.

7.5 Experiments

We divide this last section into two parts. First, we describe the method to tune the parameters and then, we show the final results.

7.5.1 Tuning

We describe which parameters must be optimized and the optimization method. We will refer to the urine database because the reasoning is the same for the pollen database.

MoG

The classifier using MoG, no matter the kind of feature used, needs to be optimized with respect to the choice of:

1. dimension of the feature space after application of Fisher's Linear Discriminants
2. number of components in each mixture
3. structure of the covariance matrix of each component
4. initial condition for EM algorithm used to estimate the mixture

In order to achieve the best reliable (and hopefully also the best) result, we procede with a systematic method. The urine database has available twelve classes and nearly one thousand images for each category. Mucus class has only 546 images, Nhyal 860 and NSE 999. We want to work during this optimization with the same number of images in test and training for each class. Then, we divide the total number of available images in all classes in two set: the first 500 will be used for only training purposes while the complementary set for only test. From the former set, we extract randomly 30 images in order to build a validation set. All training models will be shown in the following pages, are done on the rest 470 images of training set and the evaluation of the performance is done on the validation set. Then, when optimal parameters are found, a final test is done on 30 randomly chosen images of the test set.

As you can see from the curves of error rate (see Figure 7.5 and following ones), the performance is strongly dependent not only on the number of parameters used in the MoG (see Table 6.1) but also on the kind of parameters. For example, in previous simulations we found that even if you keep constant the number

of parameters, the error rate sometimes increases if you choose to increase the dimension of the space instead of increasing the number of Gaussians in the mixture. For this reason, we run a lot of simulations for different values of the feature space dimension. While this value is maintained constant, several numbers of components are tried for different structures of covariance matrix (spherical, diagonal and full).

In order to estimate a parameter we need at least 3 points. In training we use 470 images and so we should stop our search when we reach a number of 150 parameters. On the other hand, our analysis wants to be exhaustive and so we try to perform simulations up to 300 parameters. However, when we run simulations with spherical covariance matrix, there are usually more then ten Gaussians (the maximum value was 25). Unfortunately, EM sometimes does not find convergence for a so high number of Gaussians even if the number of parameters is acceptable. Indeed, we checked the starting number of points assigned to each Gaussian by "k-means" algorithm and not surprisingly we found that some Gaussian has only few points (less than ten) and it is likely that these functions easily collapse in a single point or they can give rise to local minima in the error function which may give poor representations of the true distribution. Our assessment is strengthened by some warning (probability of data given the model nearly zero) of EM program and by the results of our test on the validation set.
As you can see, for example, in Figure 7.5 there are some irregularities in the trend of spherical covariance matrix because for a high number of Gaussians EM doesn't find a model for one or two classes (giving an acceptable global error rate but for those categories the error rate is 100%!).

When we run experiments for the combination of classifiers we avoid these situations stopping the program at a lower number of Gaussians in the spherical case because we are looking for a stable system and we need a reasonable estimate of $P[C_j \mid data, mod_i]$.

The classifier using features based on PCA needs to work with dimensions of space multiple of six because each IPCs is splitted in three parts and we require to get the same number of dimensions coming from image and spectrum principal analysis[4]. For this reason, the following experiments are done for a number of dimensions equal to 12, 18 and 24.
The same argument is applied to the combination of classifiers.

The combination of classifiers modeling their outcomes needs a special care. Here, we have two trainings. In previous studies we found that a good MoG for the second training (dummy test to model outcomes) has two spherical Gaussians in each MoG. We use this model to optimize the first training and then with these good values we run another simulation to find good parameters for the second training. This new analysis confirms the previous results.
We chose to run the first training on 470 images per class (the full data training set) and then to select from this set 170 images to perform the second training.

[4] A justification for this choice is given at the end of par. 6.2.

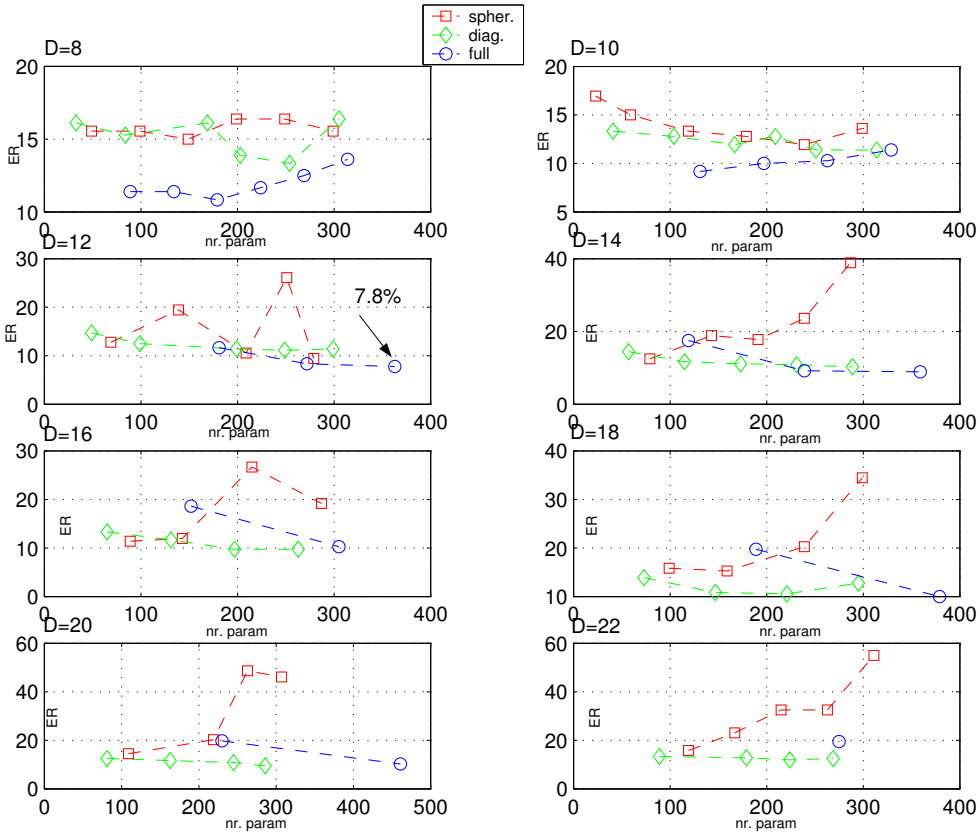

Figure 7.5: Classifier using MoG and feature based on local jets: ER as a function of the parameter number for different choices of feature space dimensions and structure of covariance matrix.

features	gauss.	dimens.
local jets	4 full	12
PCA	3 full	12
comb. feat. (indep.)	6 diag.	18
experts' combination	2 full	18

Table 7.1: Best parameters found for MoG in urine database.

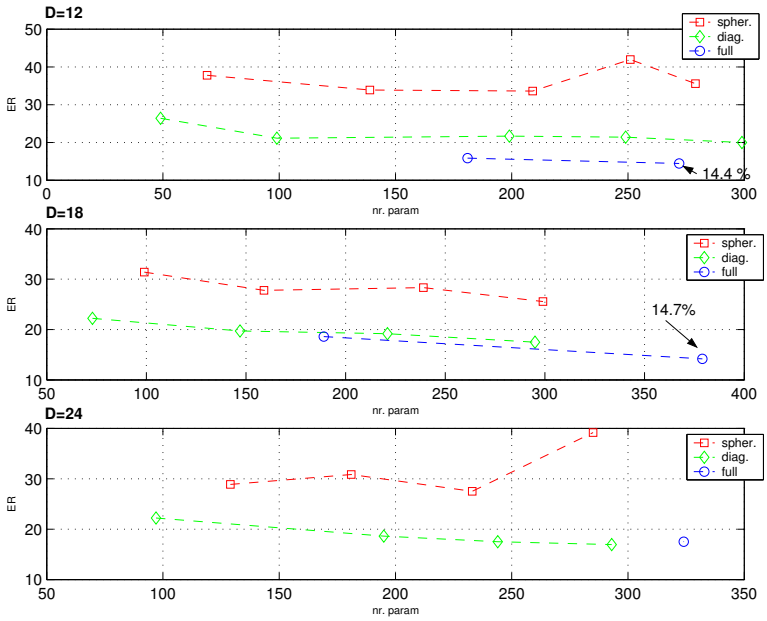

Figure 7.6: Classifier using MoG and feature based on image and spectrum principal components: ER as a function of the parameter number for different choices of feature space dimensions and structure of covariance matrix.

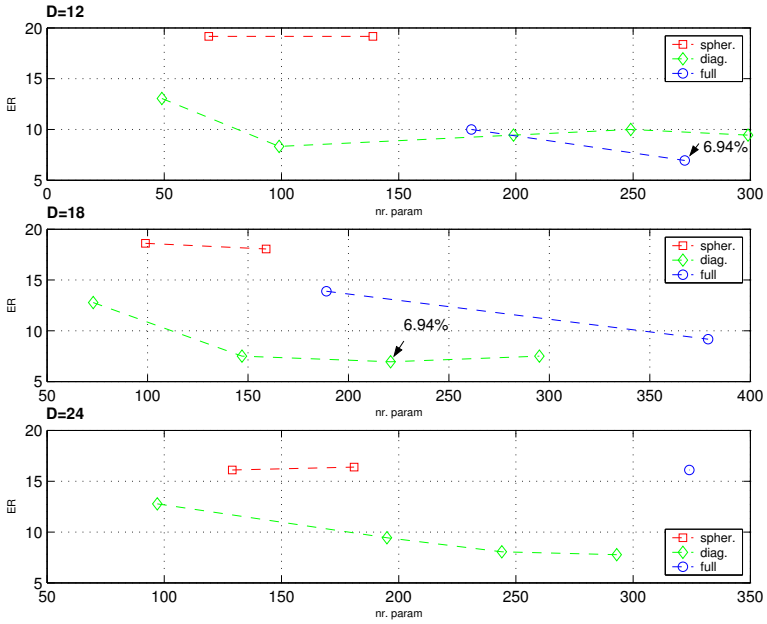

Figure 7.7: Classifier using MoG and combination of feature in independence hypothesis: ER as a function of the parameter number for different choices of feature space dimensions and structure of covariance matrix.

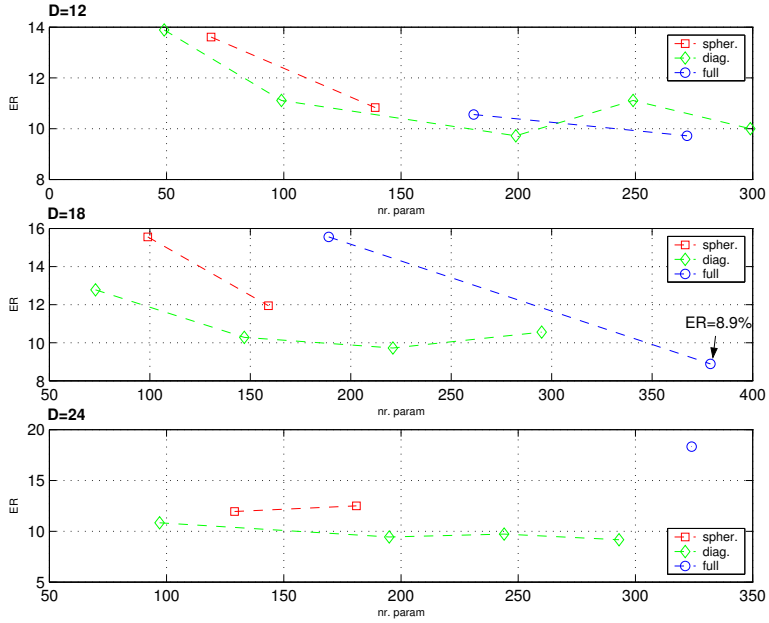

Figure 7.8: Classifier using MoG and making a combination of experts' response, first training: ER as a function of the parameter number for different choices of feature space dimensions and structure of covariance matrix.

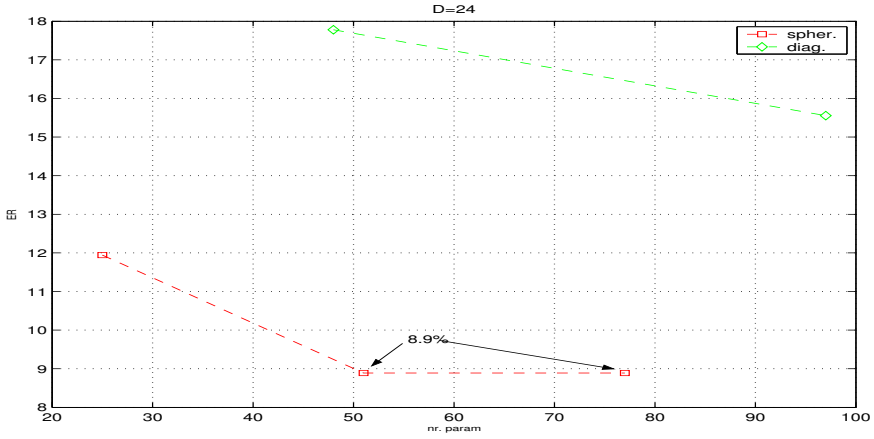

Figure 7.9: Classifier using MoG and making a combination of experts' response, second training (or modeling of results in dummy test): ER as a function of the parameter number for different choices of feature space dimensions and structure of covariance matrix.

The last set of experiments has the goal to find the optimal initial conditions for EM. Our program calls some functions of NETLAB package to estimate the MoG; we use "gmm", "gmminit" and "gmmem". The first routine uses the Matlab function "randn" (generator of normally distributed random numbers), the second one calls "randn" and "rand" (generator of uniformly distributed random numbers). The initial state of these two functions is a vector with two components for "randn" and with 35 components for "rand". So, for each mixture (that is for each class model) we have to find three vectors. We run one hundred experiments for each classifier leaving initial conditions free. At each iteration, we stored these vectors and the performance on the validation set. At the end, we force the initial state to that value which gave the lowest ER on the validation set.
Obviously, the number of Gaussians, kind of covariance matrix and number of space dimensions are the ones found in the previous simulations.
We show the results of these experiments in the form of scatter plots. At each iteration in which a different initial condition was chosen, a training model was estimated and the test was done on 30 images per class randomly extracted from the training set, test set and validation set. You can note the generally stronger correlation between the test and validation error rate versus test and training error rate.

In the classifier which combines the experts' outcomes, as you can see in Figure 7.12 (a similar situation happens also in Figure 7.11), there is no dependence of the performance on the initial conditions of the random number generator. We should not be surprised about it since we chose the maximum number of iteration of EM equal to one thousand and in this classifier we have to estimate the parameters of only two spherical Gaussians. For the classifier using feature based on image and spectrum principal components, three states are possible.

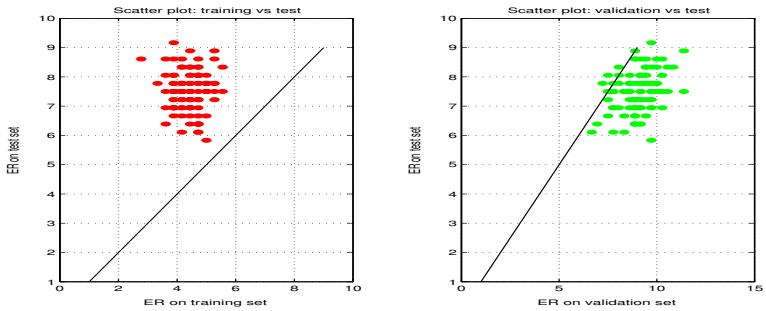

Figure 7.10: Classifier using MoG and feature based on local jets: each point in each scatter plot shows the error rate; 100 experiments were run with different initial conditions of random number generator.

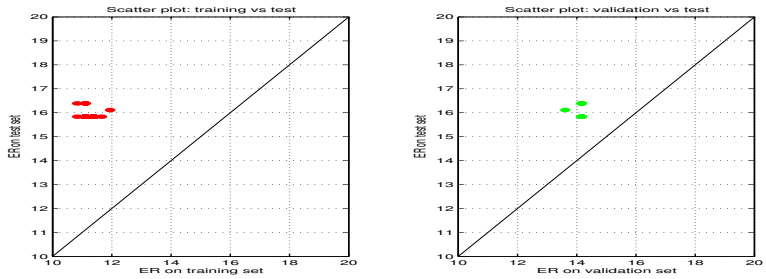

Figure 7.11: Classifier using MoG and feature based on image and spectrum principal components: each point in each scatter plot shows the error rate; 100 experiments were run with different initial conditions of random number generator (a lot of points are overlapped).

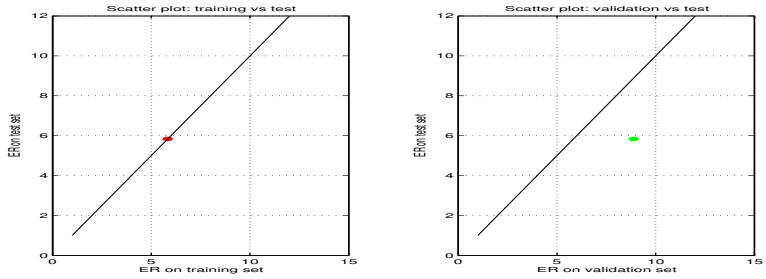

Figure 7.12: Classifier using MoG and making a combination of experts' response: each point in each scatter plot shows the error rate; 100 experiments were run with different initial conditions of random number generator (all points are overlapped).

AdaBoost

We considered 500 images from each class and extracted randomly 20 of them for validation. The complementary set is used for the final test. In Figure 7.13, the training, validation and test error rates are shown at each round. Then, we combined the 10 hypothesis in the final one as suggested in the pseudocode of Figure 7.2.

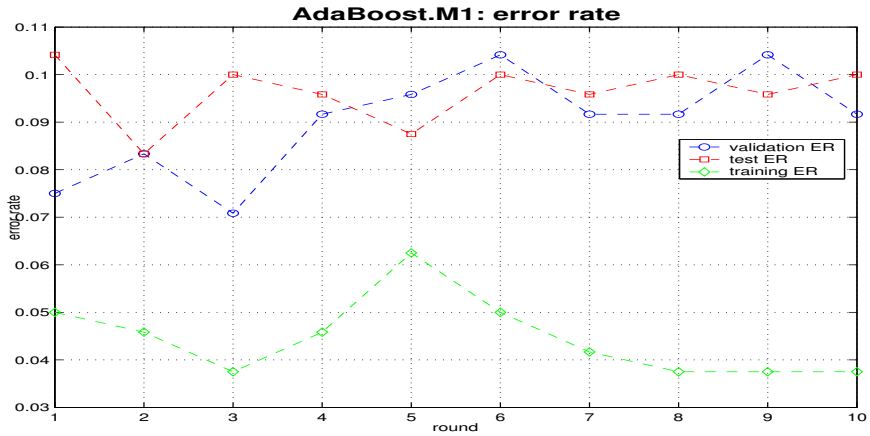

Figure 7.13: AdaBoost.M1: test, validation and training error rate as a function of the number of rounds. Training done on 480 images, each test on 20 images (randomly chosen).

SVM

The parameters we aim to find are:

1. kernel type
2. number of dimensions of feature space after reduction with Fisher's Linear Discriminants
3. parameter C
4. parameter of kernel, i.e. degree of polynomial kernel or width of Gaussian radial basis function

From our first experiments, it turns out that RBF kernels is able to achieve a lower error rate than polynomial kernel. So, we will refer only to the results of RBF kernel.

We summarize the results in Table 7.2 and following. The experiments are done taking 500 images for each class and extracting (only once) 30 images for validation purpose.

σ	D 10	D 12	D 14	D 16	D 18	D 20	D 22
0.25	10.83	11.67	12.78	15.00	16.94	19.17	20.28
0.5	9.17	**8.89**	9.17	9.44	10.56	10.00	10.83
1	10.83	10.83	10.00	10.56	11.67	10.56	11.11
1.5	11.39	11.11	11.39	12.22	12.78	11.94	12.22
2	11.94	12.22	12.50	13.06	13.06	13.33	13.89
3	14.17	13.61	13.61	14.44	14.17	15.00	14.44
4	15.28	14.72	15.28	15.00	15.83	15.83	14.72
5	16.11	15.56	15.56	16.11	16.39	16.11	17.22
10	18.33	16.94	18.61	18.61	18.33	18.89	18.33
15	20.28	18.33	18.33	18.89	19.44	19.44	20.28
20	22.50	19.44	20.00	20.56	20.83	21.11	21.94
50	26.11	23.06	24.44	25.28	27.22	28.33	28.89

Table 7.2: SVM with RBF kernel and penalty of errors $C = 1$: error rate as a function of the width σ and dimension D of feature space. The best performance is highlighted in thick black letters.

σ	D 10	D 12	D 14	D 16	D 18	D 20	D 22
0.25	12.50	12.78	12.50	15.28	16.39	18.33	19.44
0.5	10.83	10.00	**8.61**	9.44	9.44	8.89	10.28
1	10.00	10.56	9.72	9.72	9.44	**8.61**	9.17
1.5	11.39	10.83	11.39	10.56	11.67	10.00	9.72
2	11.39	11.67	11.39	11.39	12.22	10.83	10.83
3	11.67	11.39	11.94	11.94	12.22	11.67	11.94
4	11.94	11.94	12.22	13.33	12.78	12.22	12.22
5	11.94	10.28	9.44	10.28	11.39	11.11	10.56
10	12.78	11.39	11.67	11.94	12.78	12.78	13.06
15	13.33	13.06	12.78	13.89	14.17	13.89	14.72
20	14.44	14.44	14.72	14.72	14.72	14.44	15.28
50	20.56	18.06	18.89	18.89	19.44	20.00	20.56

Table 7.3: SVM with RBF kernel and penalty of errors $C = 5$: error rate as a function of the width σ and dimension D of feature space. The best performance is highlighted in thick black letters.

σ	D 10	D 12	D 14	D 16	D 18	D 20	D 22
0.25	10.56	11.39	11.94	11.67	13.61	13.33	16.11
0.5	13.33	10.28	10.00	10.56	12.78	11.11	11.39
1	10.83	10.28	11.39	9.44	8.89	9.72	9.17
1.5	10.00	9.72	9.44	9.44	10.83	8.89	9.17
2	10.28	8.89	10.00	10.28	10.56	**8.61**	9.72
3	10.28	10.00	11.11	11.67	10.28	10.56	9.72
4	11.11	10.83	12.22	13.06	11.11	10.83	10.83
5	11.67	11.39	11.94	12.50	11.67	11.94	11.94
10	12.22	12.50	11.39	12.50	12.78	13.61	13.06
15	13.89	13.06	13.33	12.78	14.17	14.44	15.00
20	15.00	14.72	13.33	12.50	14.44	14.44	15.00
50	15.83	16.67	17.78	18.33	18.89	18.89	19.00

Table 7.4: SVM with RBF kernel and penalty of errors $C = 20$: error rate as a function of the width σ and dimension D of feature space. The best performance is highlighted in thick black letters.

σ	D 10	D 12	D 14	D 16	D 18	D 20	D 22
0.25	12.78	12.22	12.50	14.17	15.56	18.61	19.17
0.5	12.22	10.28	9.44	10.83	10.28	10.83	10.28
1	10.28	10.00	9.72	9.72	10.56	9.17	**8.61**
1.5	10.28	10.28	10.83	9.17	10.56	9.17	9.72
2	10.56	10.00	9.72	10.00	9.44	9.72	9.72
3	9.72	10.28	11.39	9.72	10.83	9.44	10.00
4	10.83	10.83	11.94	10.28	10.56	10.28	10.28
5	11.39	10.83	11.39	11.67	11.94	10.00	11.39
10	12.22	12.22	12.50	11.94	12.78	12.50	12.78
15	13.33	12.50	12.78	13.61	12.78	13.89	13.89
20	14.17	13.89	14.72	15.00	13.89	15.00	14.44
50	16.94	16.11	16.39	16.39	17.22	18.61	18.89

Table 7.5: SVM with RBF kernel and penalty of errors $C = 50$: error rate as a function of the width σ and dimension D of feature space. The best performance is highlighted in thick black letters.

σ	D 10	D 12	D 14	D 16	D 18	D 20	D 22
0.25	11.67	11.67	14.17	15.00	16.11	18.89	18.89
0.5	8.89	8.89	10.28	10.28	11.11	11.11	11.67
1	8.06	8.33	7.50	7.50	8.33	8.89	8.89
1.5	7.50	7.78	7.50	**5.83**	8.06	6.67	8.61
2	6.94	7.50	7.78	6.94	6.67	6.39	7.78
3	7.50	8.61	7.50	8.06	7.22	7.50	7.50
4	8.61	8.06	7.78	8.06	8.06	7.22	7.50

Table 7.6: SVM with RBF kernel and penalty of errors $C = 100$: error rate as a function of the width σ and dimension D of feature space. The best performance is highlighted in thick black letters.

7.5.2 Final experiments

We show the final results for urine and pollen database. In order to assess the performance, a confusion matrix is built. Each row is the class to which the test images belong, the columns are the classes to which the classifier assigns the test images. Thus, in the intersection between the j-th row and the i-th column we find the following estimate:

$$P[outcome \in C_i \mid image \in C_j] = \frac{\text{nr. of items of } C_j \text{ classified as belonging to } C_i}{\text{total nr. of tested images belonging to } C_j} \tag{7.16}$$

In order to evaluate the overall performance we compute the error rate defined as,

$$ER = \frac{\text{nr. of not correctly classified test images}}{\text{total nr. of test images}} \tag{7.17}$$

Because not all the categories in our databases have the same number of images, we train and test on a uneven number of images for class. Then, we define a new error rate which is the normalized sum of single class error rates

$$ERp = \frac{1}{K}\sum_{j=1}^{K} \frac{\text{nr. of misclassified test images belonging to } C_j}{\text{total nr. of test images belonging to } C_j} \tag{7.18}$$

For example, when we consider the whole system for pollen recognition we will see that the classifier has to analyze also particles of junk. The ratio between pollen and junk particles is 1 out of 10. If we test 100 pollen patches and 1000 junk patches it is possible that the classifier has an ER = 10% which can be considered quite good. However, it is possible that most of junk particles are classified as junk and most of pollen particles are misclassified, the ER simply can not say if the less numerous classes are well classified. Instead when you consider also the

ERp you can check if the error is evenly or proportionally distributed among the categories.

Urine database

First, we consider the classifier using mixture of Gaussians with the different kinds of features studied.
During the tuning of parameters, we focused on data belonging to the training and validation set. Now, we show some results of experiments done in the following way:

1. training and test using the full data set available and with different number of images per class; we pay attention to put in the training set all the images belonging to the previous training and validation set and we choose randomly (from the complementary set) 10% of the total amount of images for test; the result will be the average of 10 experiments

2. we run 100 experiments on the full data set available; at each iteration we randomly extract about 10% of images for test purpose.

In Figure 7.15, Figure 7.14, Figure 7.16 and Figure 7.17 we show the graphical representation of confusion matrix using the first method for the four different kinds of classifiers based on MoG modeling.
Note that the numbers in the plot are in percentage with respect to the total number of images tested for a certain class. Moreover, we show the average result on 10 experiments.
The experiments with the classifier that combines the experts' outcomes, need a comment. We have to choose the subdivision of the training set for the first and second training. When we used 7/9 of the training set for the first training and 4/9 for the second one (so, there is a partial overlap of 2/9) we got an ER equal to 9.8%; a second time we took all the images of the training set for the first training and we extracted randomly from this set half of them for the second training and we got an ER equal to 8%. The trend was confirmed by the last experiment, shown in Figure 7.17, when we used for both trainings all the images available in the training set; in this way we got an ER of 7.7%. Even if the second training models the training outcomes (or the training errors), the general performance is improved.
The best result is achieved with the classifier using features based on local jets, its error rate is equal to 6.8% (the proportional error rate is 6.5%).

Finally, we show the average results of 100 experiments on the full data set taking randomly 10% of images for test, see Figure 7.18, Figure 7.19, Figure 7.20.

Why did we choose to perform 100 experiments? Because we want a reliable estimate of the average ER with a low standard deviation. Now, we give a brief overview of the theoretic study for the choice of the experiment number.
If x is a stochastic binary variable with alphabet $A_x = \{0, 1\}$ and $P[x = 1] =$

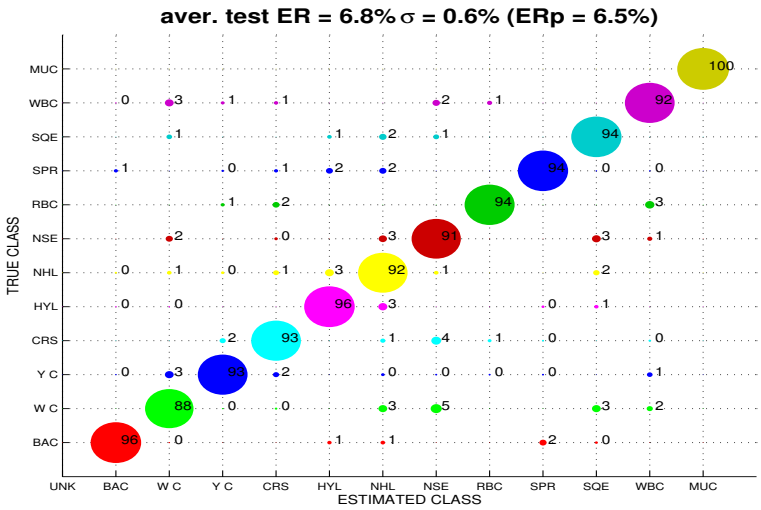

Figure 7.14: Classifier using MoG and feature based on local jets: averaged confusion matrix for experiments in which 90% of images in the full data set is used for training and 10% is randomly extracted for test; there is no overlapping between the test items and previous trained images.

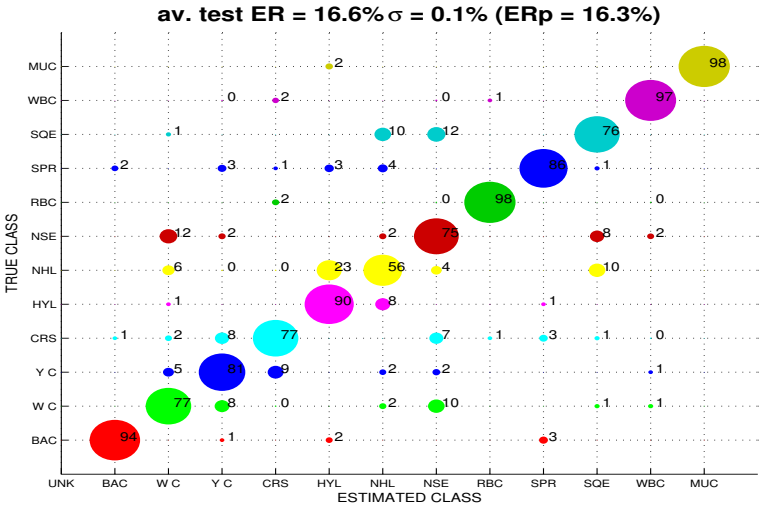

Figure 7.15: Classifier using MoG and feature based on image and spectrum principal components: averaged confusion matrix for experiments in which 90% of images in the full data set is used for training and 10% is randomly extracted for test; there is no overlapping between the test items and previous trained images.

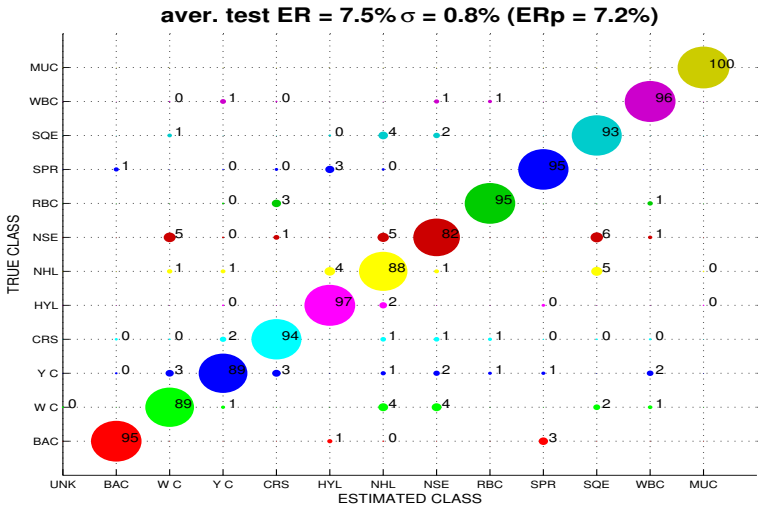

Figure 7.16: Classifier using MoG and feature combination in indep. hyp.: averaged confusion matrix for experiments in which 90% of images in the full data set is used for training and 10% is randomly extracted for test; there is no overlapping between the test items and previous trained images.

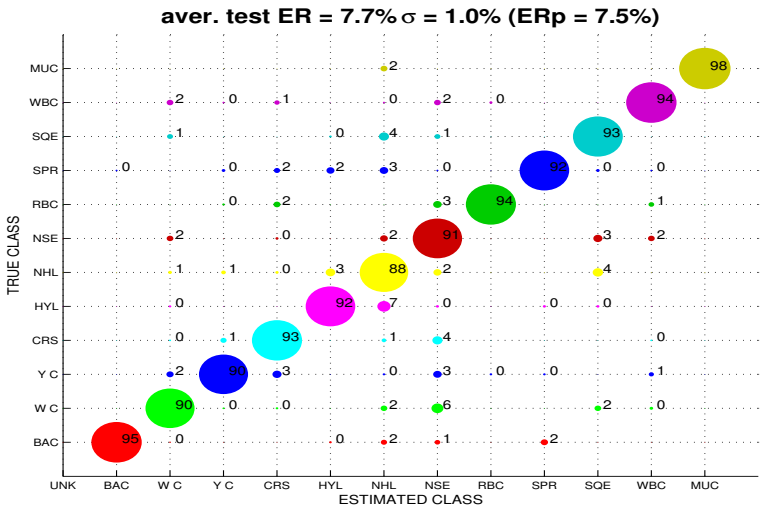

Figure 7.17: Classifier using MoG and making a combination of experts' response: averaged confusion matrix for experiments in which 90% of images in the full data set is used for training and 10% is randomly extracted for test; there is no overlapping between the test items and previous trained images.

$p(1) = p$ it is easy to find that the mean of x is $m_x = p$ and its variance $\sigma_x^2 = p(1-p)$. We can interpret this variable as the outcome of the following event: "the classifier takes the right decision on the test image".
If you consider n stochastic binary variables and all these variables have the same parameter p and are independent, we can define the sum variable $y = \sum_{i=1}^{n} x_i$ which is a binomial one with parameters n and p; its mean and variance are: $m_y = np = nm_x$, $\sigma_y^2 = np(1-p) = n\sigma_x^2$.
Let be $z = y/n$, then $m_z = m_y/n = p = m_x$, and $\sigma_z^2 = \sigma_y^2/n^2 = \sigma_x^2/n$. We can think that y describes the statistic of n decisions of the classifier on n test images, and z the performance when considering n test images. You can note that increasing n you can decrease σ_z^2.
In order to have a reliable result for the performance of our classifier we could average the results on many experiments. Given the (estimated) performance if we choose properly the number of images to test and the number of experiments, we can control the variability of the error rate.
Let be m the number of experiments we want to run and $w = \frac{1}{m}\sum_{i=1}^{m} z_i$, then it can be shown that $m_w = m_z = m_x$ and $\sigma_w^2 = \frac{1}{m}\sigma_z^2 = \frac{1}{mn}\sigma_x^2$.
Finally, we can approximately estimate the standard deviation of the ER in our experiment doing the following hypothesis: if the probability to misclassify an image is nearly $p = 0.1$ (even if it depends on the belonging class), m is equal to 100 and n is about 100*12 (in practice it is less), then

$$\sigma_w = \frac{\sigma_x}{\sqrt{mn}} \simeq \frac{\sqrt{9 \cdot 10^{-2}}}{\sqrt{12 \cdot 10^4}} \simeq 7 \cdot 10^{-3}$$

With this choice of parameters, we can be confident to find an ER with a standard deviation of about 0.7% (below 1%).
These result is confirmed by our experiments as you can check in Figure 7.18, Figure 7.19, Figure 7.20.

As you can see for example in Figure 7.18 and expect, the confusion matrix has an high symmetry with respect to the diagonal. For example, 2.5% of Hyal are classified as Nhyal and vice versa, 4% of NSE are classified as white cell clumps and 3.9% of these particles are classified as belonging to NSE class.

The best performance is again achieved using the classifier with features based on local jets, the error rate is equal to 7.6%. If you look at Figure 7.18, the best classified class is mucus with an ER equal to 2%; the worst classified particle is NSE. Most of errors are done between white cell clumps and NSE, white cell clumps and squame epithelius, hyal and nhyal.

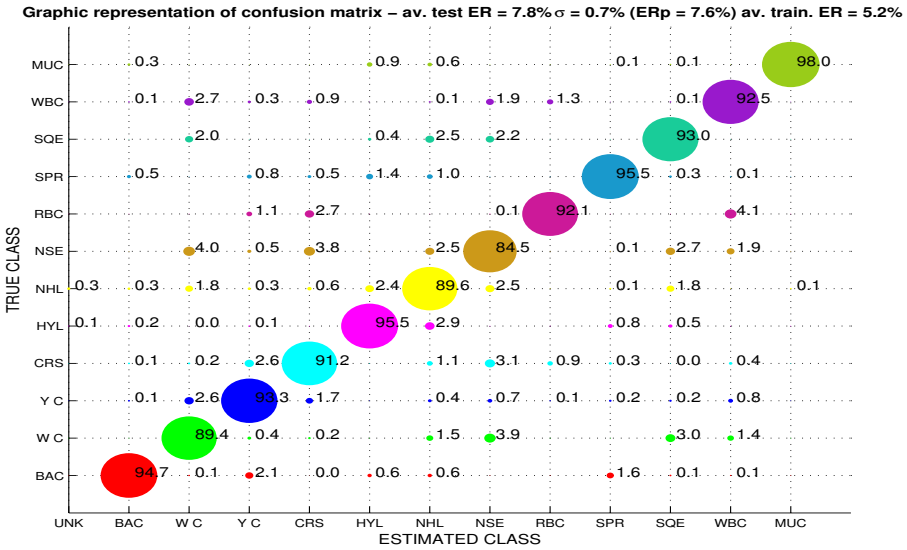

Figure 7.18: Classifier using MoG and feature based on local jets: averaged confusion matrix of test errors for 100 experiments in which 90% of images in the full data set is used for training and 10% is randomly extracted for test.

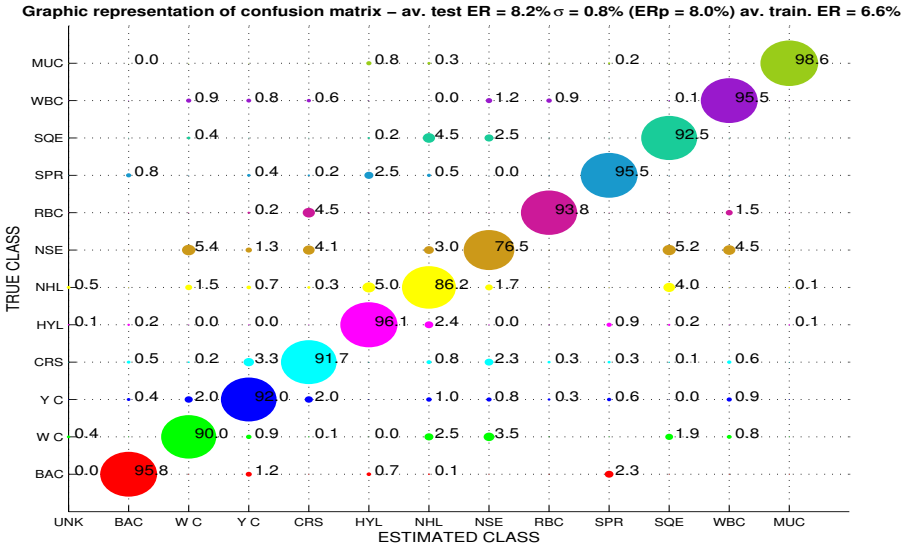

Figure 7.19: Classifier using MoG and feature combination in indep. hyp.: averaged confusion matrix of test errors for 100 experiments in which 90% of images in the full data set is used for training and 10% is randomly extracted for test.

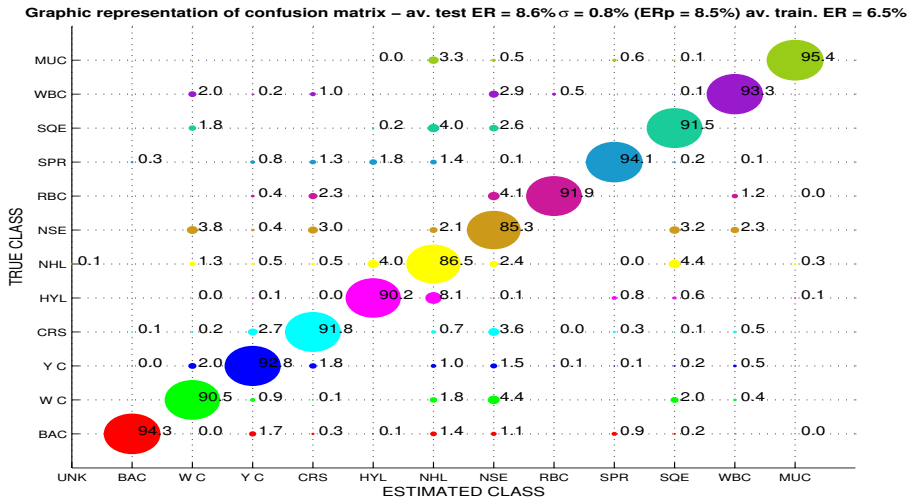

Figure 7.20: Classifier using MoG and making a combination of experts' response: averaged confusion matrix of test errors for 100 experiments in which 90% of images in the full data set is used for training and 10% is randomly extracted for test.

We now show the results of AdaBoost inspired algorithm. With the hypothesis found during the experiments of Figure 7.13, we run a test on 10% of images in the data set (not belonging to previous training or validation set). In Figure 7.21 and Figure 7.22, the averaged performance on 10 experiments is shown for the standard classifier (that is taking only the first hypothesis) and for the boosted one. As you can notice there is an improvement of 0.5% in the error rate.

Taking the best achieved performance on validation set, we run experiments using SVM following the methodology above-mentioned for AdaBoost. Unfortunately, we achieved an error rate of 12.2% in test and below 2% in training. This is caused by training data overfitting. We have to choose parameters for SVM to find a sort of balance between accuracy attained on a particular training set, and the capacity of the machine to learn the general properties of our data. With this choice of parameters, the system seems to have a little generalization. For this reason, we tried other "good" but sub-optimal values for the parameters and the best performance is reported in Figure 7.23. There is still a big gap between the performance on training and test set however there is an improvement of 0.5% and 1% in the absolute and proportional error rate with respect to the classifier using MoG.

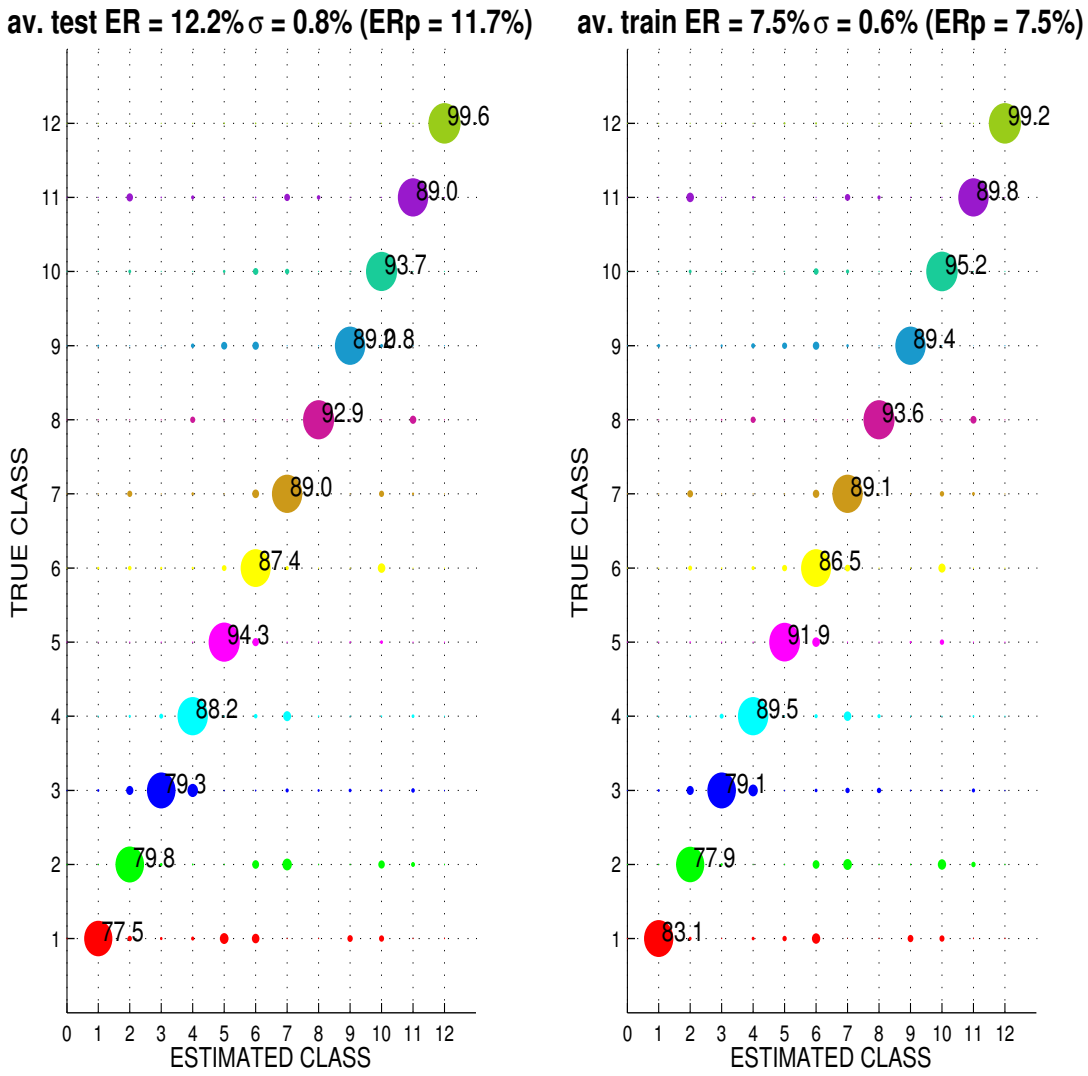

Figure 7.21: Test and training confusion matrices for the original classifier using MoG and local jet based features. The training is performed on 480 images and the test on 10% of full data set. The result is averaged on 10 experiments. In this figure and in the following ones, the classes are identified with numbers in accordance to Table 3.1. The numbers in the diagonals are the percentages of correct classification in each class.

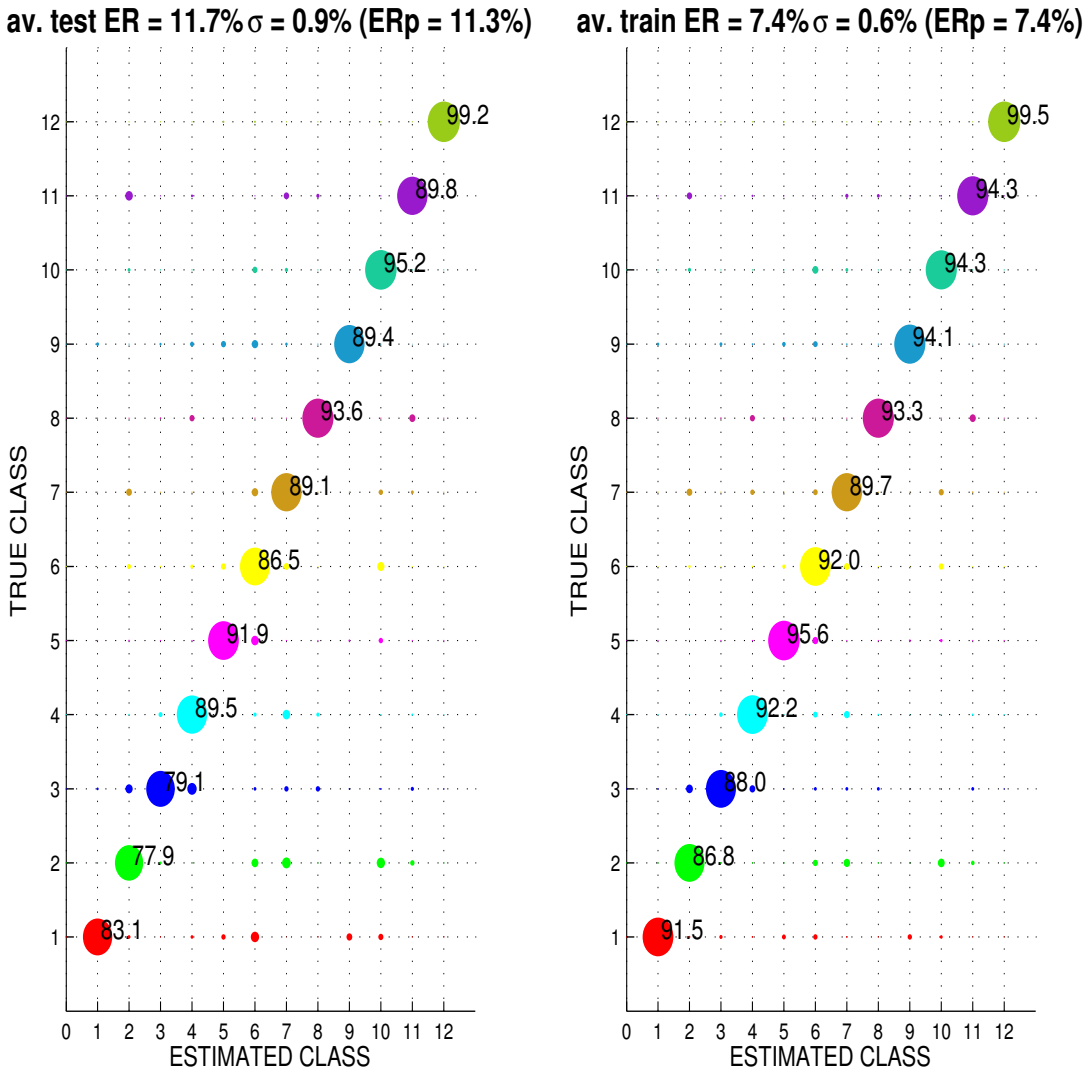

Figure 7.22: AdaBoost.M1: test and training confusion matrices. The training is performed on 480 images and the test on 10% of full data set. The result is averaged on 10 experiments.

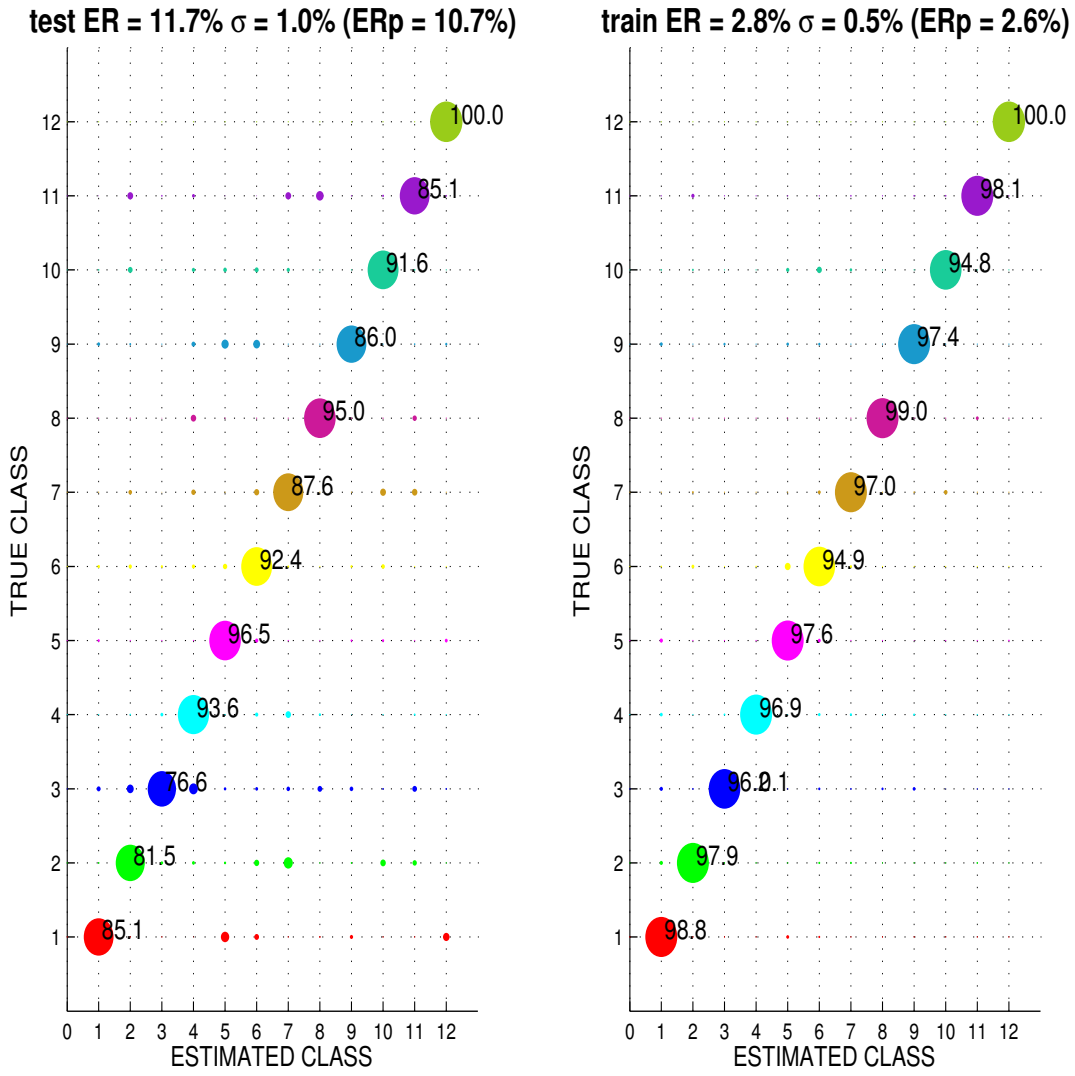

Figure 7.23: SVM with rbf kernel $C = 5$, $\sigma = 1$ in a 20 dimensional feature space: test and training confusion matrices. The training is performed on 500 images and the test on 10% of full data set. The result is averaged on 10 experiments.

Pollen database

We show the performance of classifier using MoG with feature based on local jets. The database we are considering is the "pure" pollen database and the six most numerous categories. These classes have more than 1000 images. It turns out from the tuning stage that the best modeling is achieved taking 2 full covariance matrix in each mixture and considering a 20 dimensional feature space. The tuning was done on 500 training images per class from which 30 images were extracted to build a validation set. Then, we run 100 experiments taking from each class the 10% of available images for test and the rest for training, see Table 3.2. We paid attention to avoid that images belonging to previous training and validation sets are selected in the current test set. The averaged test error rate is 10.2%, see Figure 7.24.

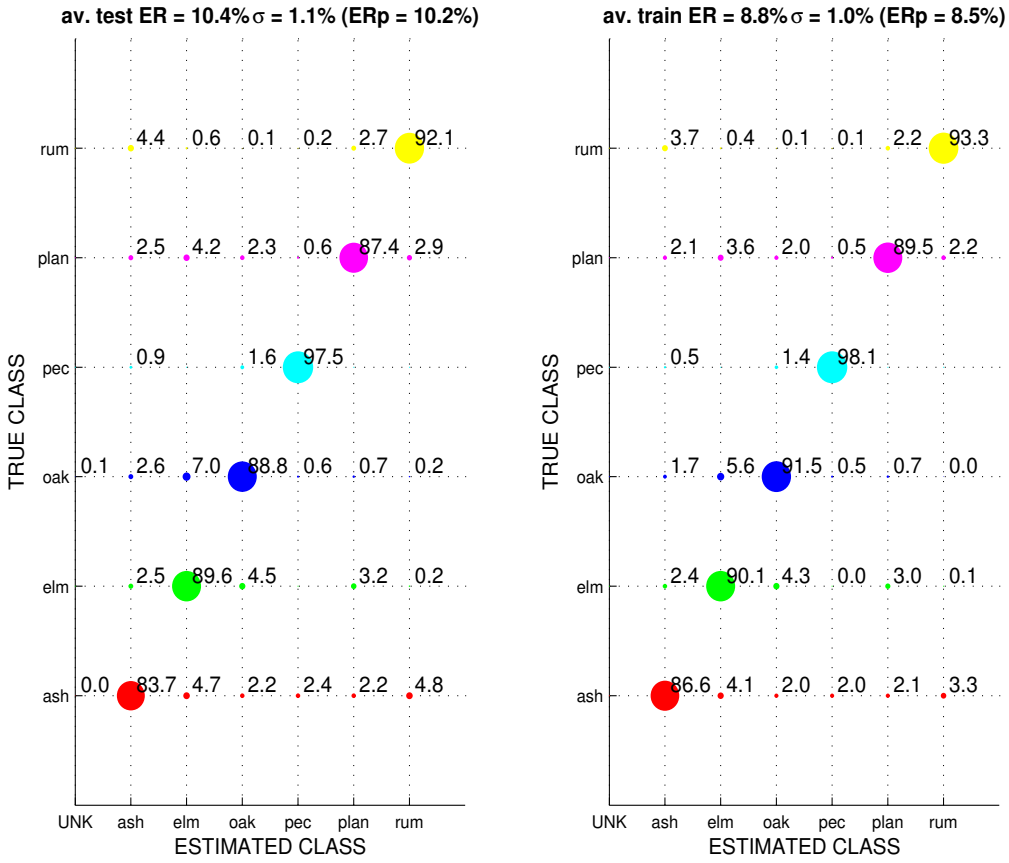

Figure 7.24: Test and training confusion matrix for the six most numerous categories of "pure" pollen. The result is averaged on 100 experiments (no overlapping between test set and current or previous training sets).

Analogously, we made an experiment taking the 13 most numerous classes in the "pure" pollen database (see Table 3.2), that is all the categories with more than 100 images and we got a proportional averaged test error rate around 19%,

see Figure 7.25.

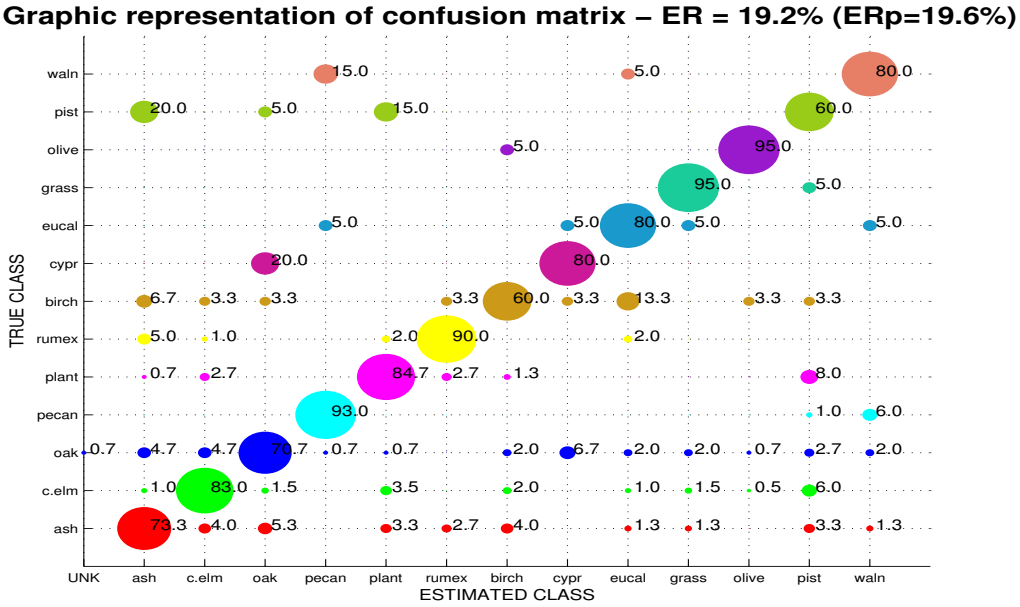

Figure 7.25: Test confusion matrix for the 13 most numerous categories of "pure" pollen. The result is averaged on 100 experiments (no overlapping between test set and current or previous training sets).

Is useful to test the classifier on "pure" pollen database? How should we read these results?
In order to answer to these questions, we describe an analysis of pollen database which will give a deep insight on how the "pure" pollen database is related to the air sampled pollen database.

We consider the classes of air sampled pollen database with more than 60 items. These categories are: ash, chinese elm and oak. In the "pure" pollen database these species have more than 1000 images, see Table 7.7 and Table 3.2. We make a test on a number of images that is the 10% of air sampled pollen database. The experiments done with the classifier using Mog and local jet based features are:

1. train and test on pollen grains captured by air sampler machine

2. train and test on "pure" pollen grains with a number of images equal to case 1

3. train on "pure" pollen grains and test on air sampler pollen grains using the same number of images of case 1

4. train and test on "pure" pollen grains using for training all the remaining part of images in the "pure" pollen database

5. train on the same "pure" pollen images of case 4 and test on the air sampled pollen grains of case 3

Class	training on few samples	training on many samples	test
ash	68	1275	7
chin. elm	112	1904	12
oak	60	1473	6

Table 7.7: Number of samples used in experiments for pollen database assessment.

For experiments with few training data, each mixture has two diagonal Gaussians while for experiments with more than 1000 images per class we chose to model the distribution of the data with a mixture of seven diagonal Gaussians. The results are shown in Figure 7.26 and Figure 7.27.

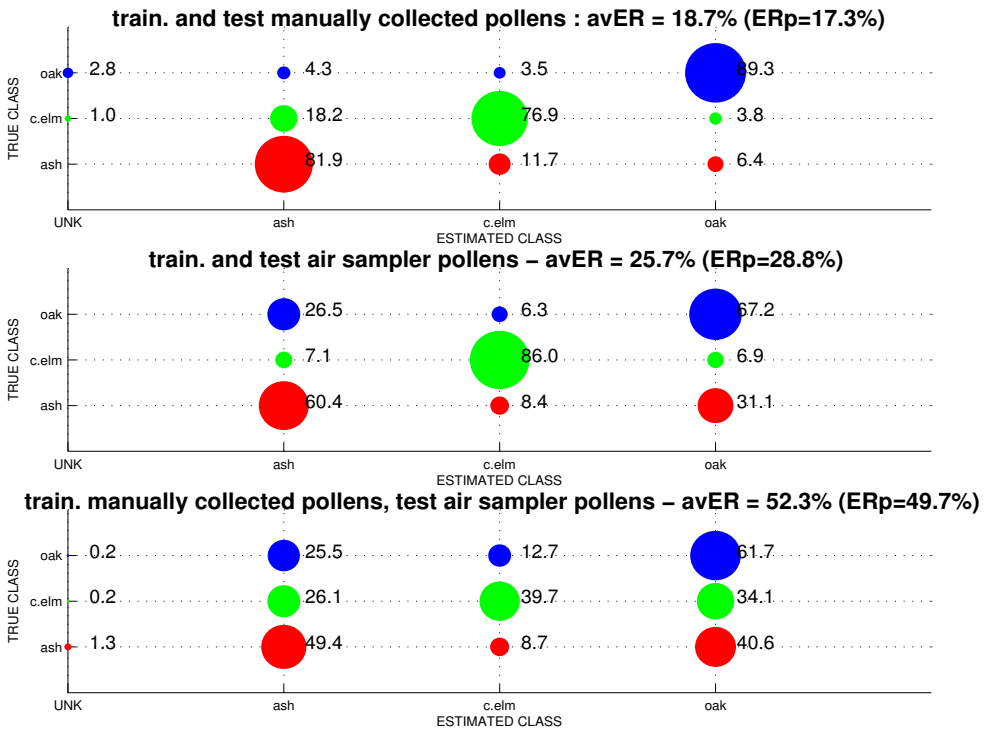

Figure 7.26: Pollen database: confusion matrix when training is done on few samples; the result is an average of 100 experiments

The aim of these experiments is also to find an estimate of the error rate for the same classifier when the training and test are done on air sampled pollen grains

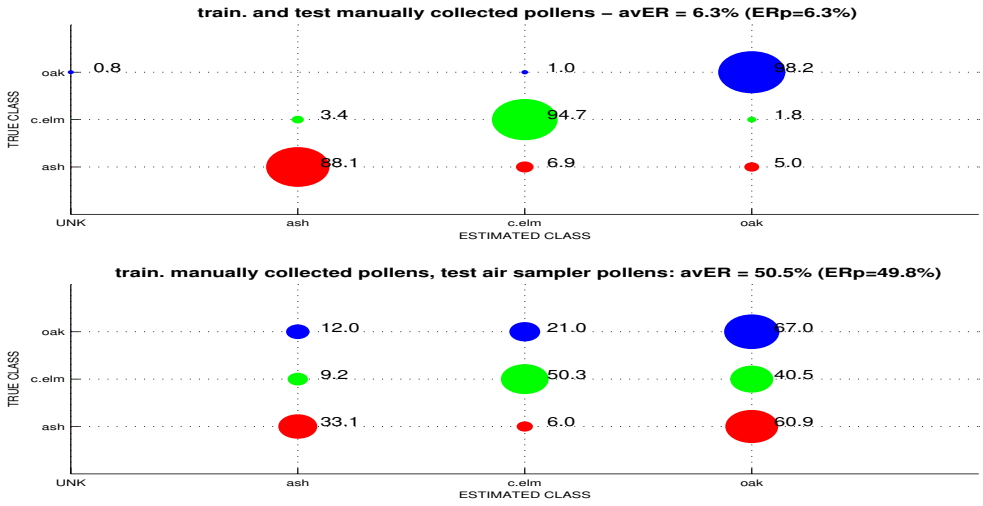

Figure 7.27: Pollen database: confusion matrix when training is done on many images (more than 1000); the result is an average on 100 experiments

and the training has available 1000 images for each class. Since our database of air sampled pollen particles does not have such a quantity of data (see Table 3.2), we linearly interpolate this error rate from the error rates found in the previous experiments; the promising result of 15% is found as shown in Figure 7.28.

Thanks to this analysis, we can claim that there is inconsistency between "pure" pollen and air sampled pollen database. It is not worth to train with the "pure" pollen images and then to test the air sampled pollen images because the former ones are without junk in the background, less variable in shape, texture and color.
However, training and test done on "pure" pollen database will allow to find a lower bound for the error rate of the classifier using only pollen captured by spore trap.

The system must be evaluated using air sampled pollen particles in order to have a realistic estimate of the performance of a measurement instrument. However, "pure" pollen images can give an idea of which kind of particles are most difficult to classify.

Moreover, we should observe how much the performance improves with the number of training images; as you can see in Figure 7.26 and Figure 7.27, the error rate decreases from 18% to 6% if more images for training are taken when using "pure" pollen images. This fact is also highlighted by the great gap between training and test error rate when few images are taken for training.

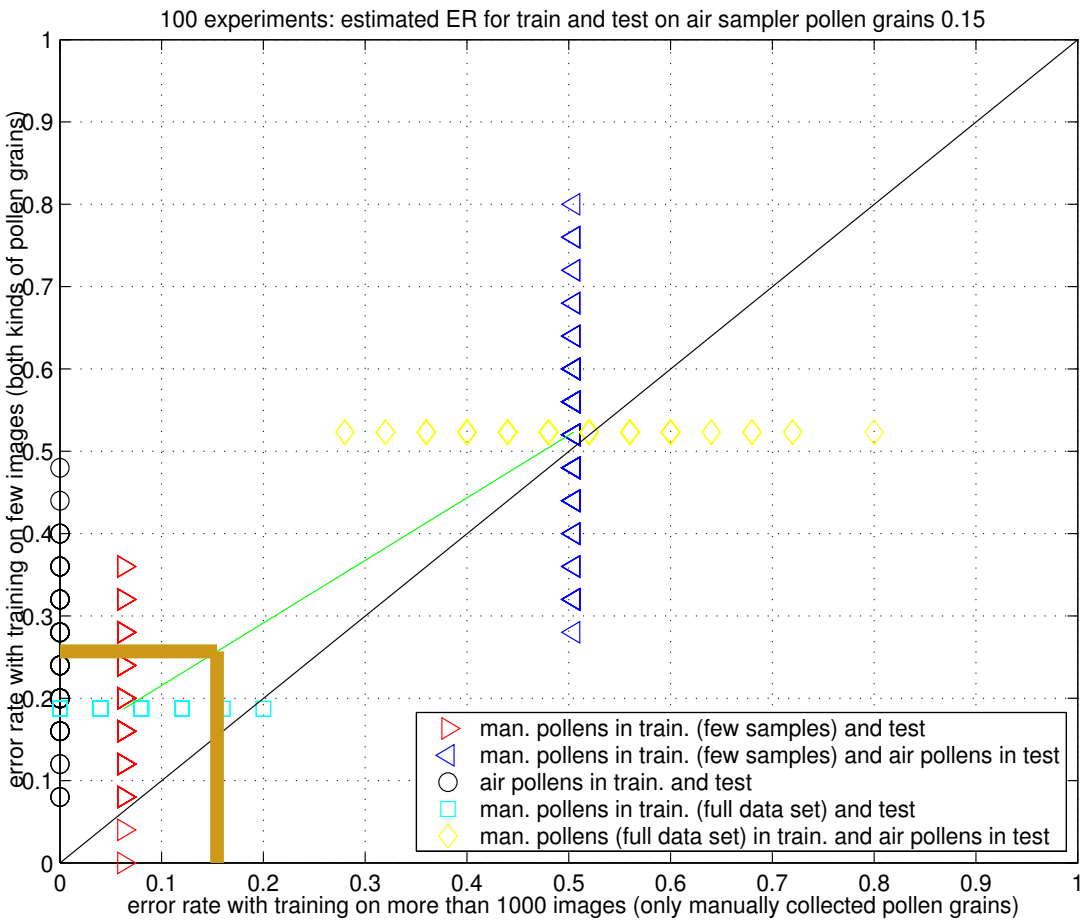

Figure 7.28: Pollen database: graphical estimate of error rate when the training is done using many (more than 1000) images of pollen grains captured by volumetric spore trap.

Chapter 8

Analysis of errors

In this chapter, we analyze errors made by detector and classifier. We aim to find where the mistakes are made and to understand why they are made. We conclude each section with some ideas to overcome these problems.

8.1 Detector

In this section, we will refer to detection of pollen in images of tape taken from a volumetric spore trap.

Detector based on DoG -see par. 5.1, is not able to detect all particles of interest because there is a quite big difference of dimension among particles belonging to different categories. For example, pine pollen maybe bounded by a square box of side greater than 200 pixels while eucalyptus by a square box of 40 pixel-wide side. So, the sample frequency and the variance of the Gaussian kernel will only be good for grains of a certain size. Moreover, some pollen particles have a very low contrast with respect to the background, because they have no texture. Thus, they can give low values of extrema in the DoG image even if their size is matched by the sample frequency and variance of the Gaussian kernel. Finally, there are a lot of particles in the background that are similar to pollen grains if you only consider information about size and shape as this detector does.

Focusing now on morphological detector, we show an example of missed detection in Figure 8.1 and Figure 8.2.

In this situation, the error was caused by the test on the mean gray level value of pixels fallen inside the region containing the pollen. Because the pollen is quite dark and is attached to a black junk, this region is skipped.
Generally, the kinds of situation that make the detector fail are:

- pollen has very low contrast and edge detector is not able to find its contour
- pollen is close to dark junk and the found region contains both of them
- pollen has dimension or contrast out of range with respect to the fixed thresholds

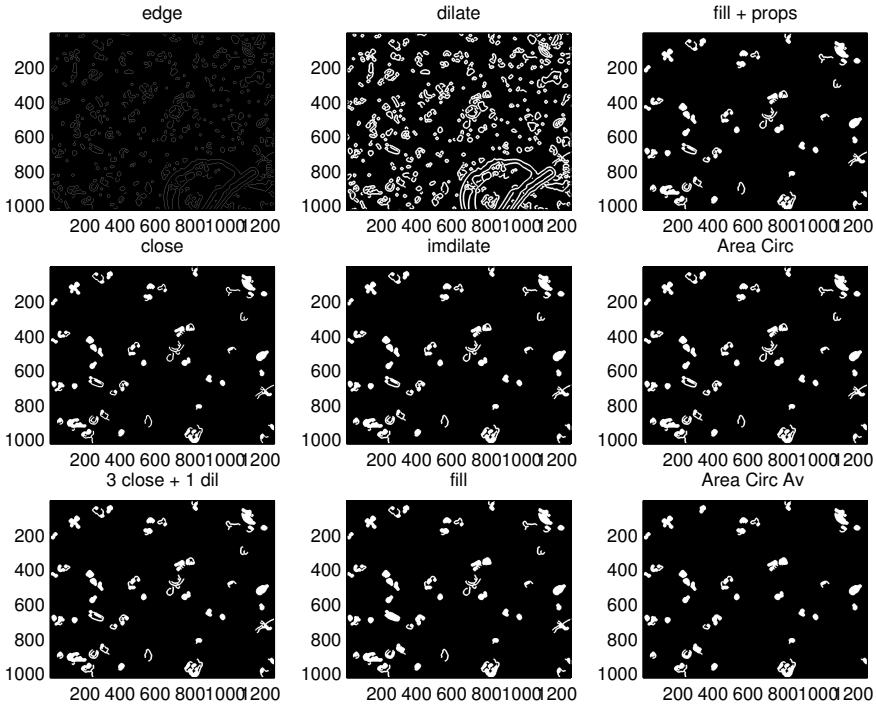

Figure 8.1: Mask computation performed by morphological detector.

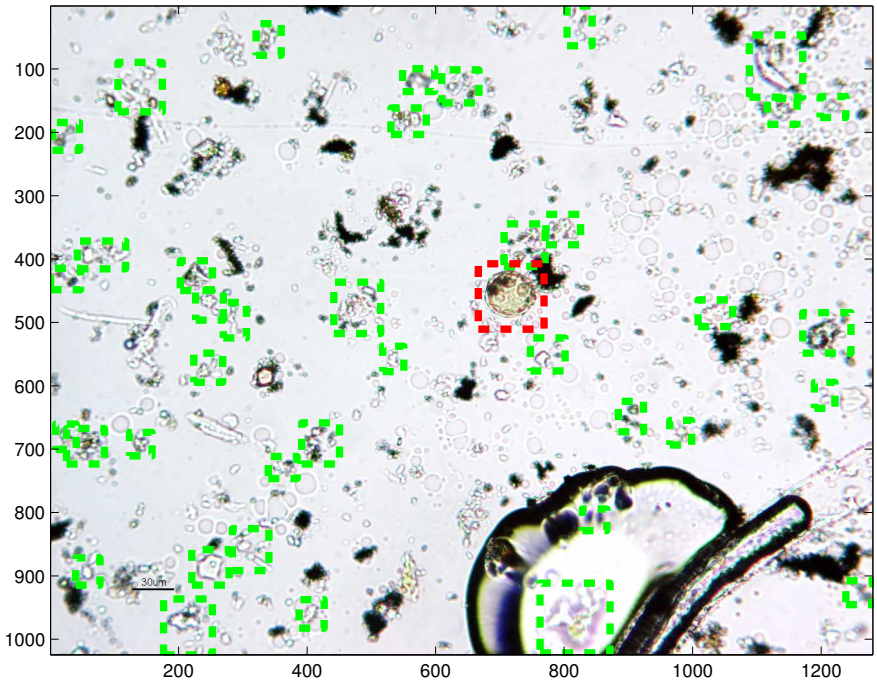

Figure 8.2: Errors of morphological detector: the green boxes are the automatically detected patches, the red box was selected by the expert.

The main cause of missed detection is the second one.

False alarms are due to the high number of particles in the images with similar statistics to pollen particles. False alarms are typically round objects with the same pollen size but with different texture.
Their number could be indirectly reduced increasing the spatial resolution of images, that is, making the wheel of the air sampler machine to rotate faster.

In conclusion, the detector based on DoG seems to be intrinsically limited in its performance because of the high variability in dimension and contrast of pollen grains. The morphological detector could be further improved considering texture inside the regions of interest.

8.2 Classifier

In this section, we will refer to experiments done on urine database. The classification errors will be analyzed with reference to the Bayesian classifier using feature based on local jets.
In particular, we refer to experiments done on full data set taking 10% of images for test. These images are randomly extracted by a set never used for training and validation.

In Figure 8.3, we show the misclassified images with the estimated class and the assigned probability (in percentage). This probability is the probability of the estimated class given the extracted feature vector. We note that for most of these images the probability is below 90%. This is a good point because in a real application we could assign these items to an unknown class for further analysis.

Let us try to give a deeper insight on the previous misclassification. In Figure 8.4, we show a collage in which in the central column there are some (misclassified) images of Figure 8.3 with assigned high probability. In the first three columns there are images belonging to the true class that are the nearest to the one in central column in the euclidean norm of the feature space (after the projection on FLD). In the last three columns, there are images belonging to the estimated class that are the nearest in the same feature space.
If you follow a row you can see the smooth transition in the features space from one class to the other; with this interpretation the misclassified image is on the boundary between the two classes and it can be thought like a transition item.

We note that some errors could be avoided by considering features with information on shape. For example, in the second row of Figure 8.4, it seems clear that the average of local jets doesn't allow to separate clearly the image on the fourth column from the image in the fifth column but we should overcome this difficulty considering shape and texture of these two images.

On the other hand, there are images which are really hard to distinguish because of a certain intrinsic ambiguity of the database.
What is the difference between the images on the fourth and fifth columns in the intersection with the fifth, sixth, tenth and eleventh row? It is an embarassing

question, which was also posed to the experts who provided us this database, and they could not say it! This intrinsic ambiguity will constitute a lower bound for the error rate of any classifier on this data set and this bound could be found with a test on the human (expert's) error rate on this database.

Analogous analysis can be done on pollen database. Errors are made because our features do not capture all the essence of texture in particles and because we are not using color information.

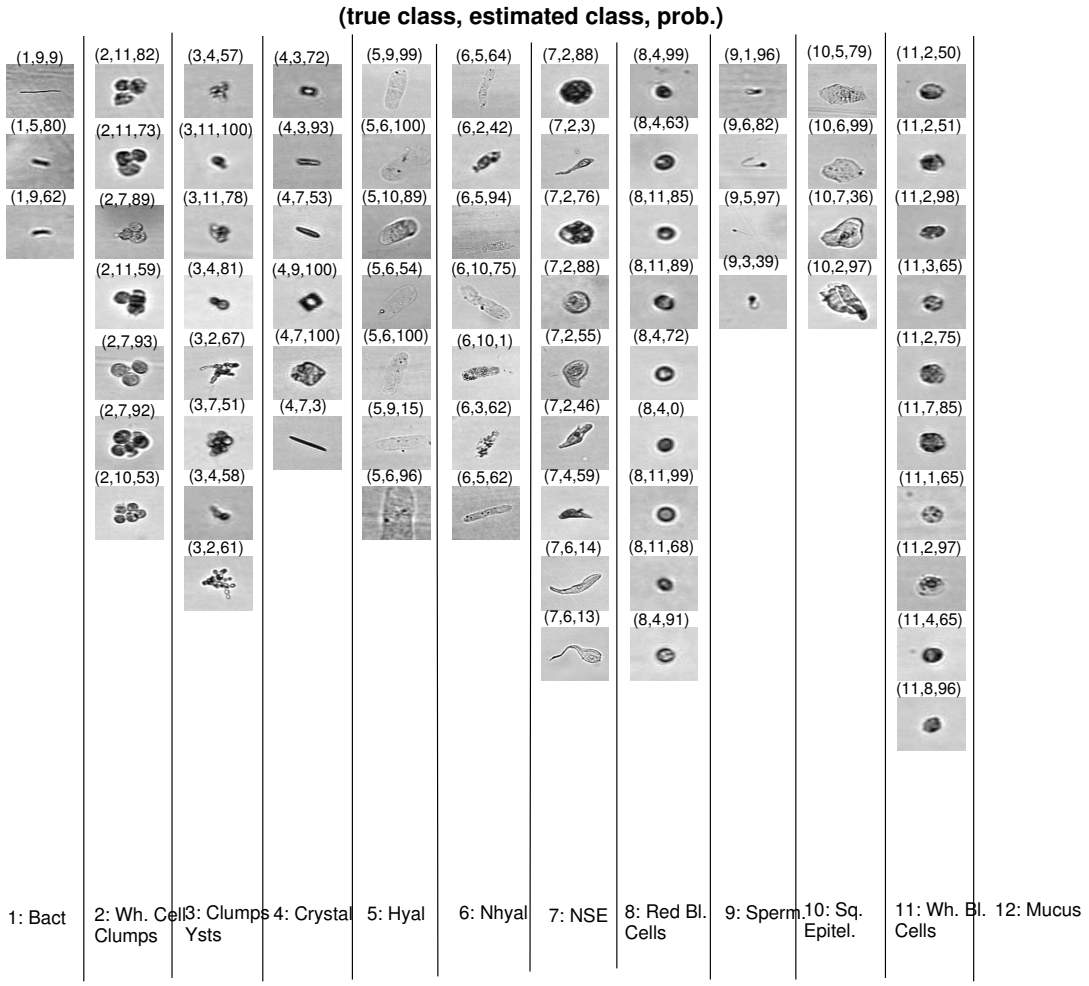

Figure 8.3: Analysis of classification errors: misclassified images by Bayesian classifier using features based on local jets.

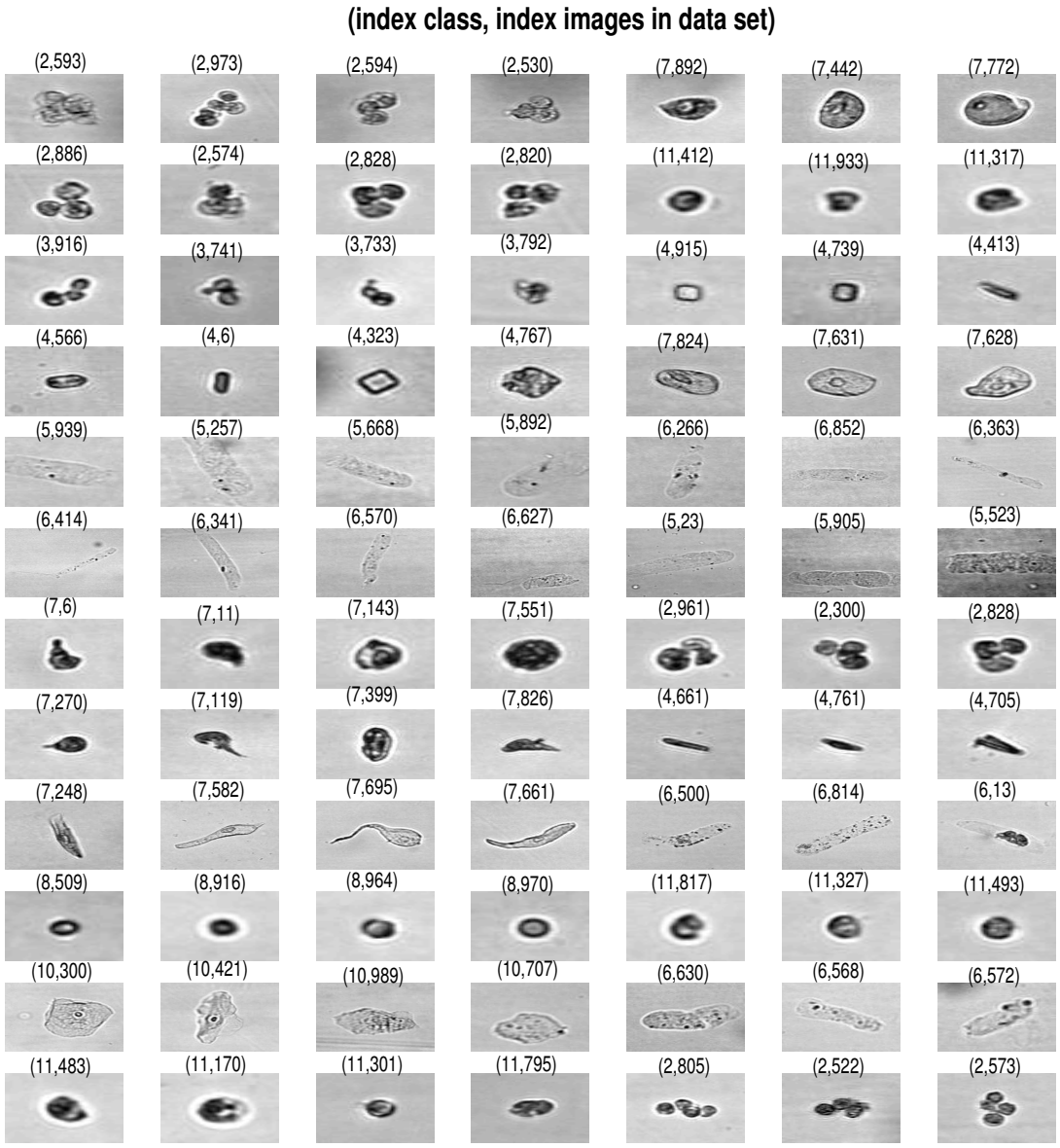

Figure 8.4: Analysis of classification errors: nearest images in the euclidean norm of the feature space. In central column the misclassified images, in the first three columns the closest images belonging to the true class, in the last three columns the closest images belonging to the estimated class; each row is referred to the image in its central column. Above each image, there is the class number and its index in the database.

Chapter 9

Whole system

This chapter has for its main aim to combine detector and classifier in order to assess the performance of the whole system.
We can identify particles only in the database of pollen captured by spore trap and so, we will refer to this database throughout the following discussion.

We consider the morphological detector because it gave good results and it is able to do a good segmentation of the object of interest. We assume that for each found pollen there are 10 false alarms (see Table 5.2).
The first step is to build a database with those patches individuated by this detector. Basically, we run the detector on all images with pollen grains captured by air sampler machine and each detected patch is put in the proper folder according to the experts' reference list. We add a new class, called "*unknown2*", to gather the false alarm patches. Note that during classification we use also class "*unknown1*". This is the class where we put the images which do not pass the test of eq. (7.8).
In Table 9.1, you can find the number of patches in each category and in Figure 9.1 we show some patches of this database.

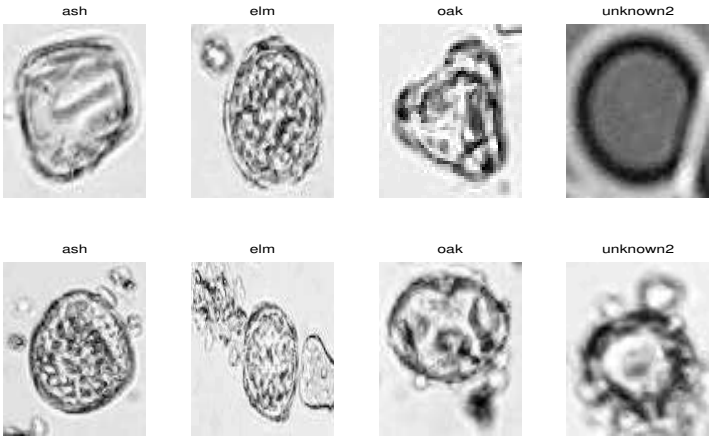

Figure 9.1: Example of patches in database built by detector.

We apply the Bayesian classifier using features based on local jets. This

GENUS	NUMBER OF ITEMS
ash	72
chin. elm	119
oak	67
pecan	5
cypress	32
eucalyp.	3
grass	1
olive	10
walnut	17
pine	32
liq. amber	19
alder	13
asteraceae	3
c. myrtle	3
chenopod	19
ginkgo	3
mulberry	36
palm	21
plane t.	7
poplar	5
sycamore	17
umbellif.	4
false alarms	8922

Table 9.1: Pollen database built by morphological detector. Number of patches in each class.

CLASS	TRAIN.	TEST
ash	65	7
chin. elm	107	12
oak	61	6
unk. 2	2330	250
total	*2563*	*275*

Table 9.2: Number of samples used in training and test to assess the performance of the whole system.

classifier is one of the best we have found but it needs a lot of images to estimate parameters in the MoG. For this reason, we consider only categories with more than 50 images, namely: ash, elm, oak and obviously "unknown2". We extract from the "unknown2" set a number of images that is coherent with detector performance. The total number of pollen patches is 258, thus we consider 2580 patches of unknown particles. From each class set we take randomly the 10% of images for test, the rest is for training. To summarize, we test 7 images of ash, 6 of oak, 12 of chinese elm and 250 of "unknown2" class, see Table 9.2.

We can choose to model the "unknown2" class or to model only the pollen categories. In our experiments we try both solutions.

Test stage in the classifier is modified to take into account the analysis of "unknown2" particles. Precisely, besides the test on resolution of eq. (7.8), there is a test on the estimated probability of the class given the image. If this value is too low, then the classifier puts the image in class "unknown1", the same happens if the image resolution is out of the range of every class, see eq. (7.8).

In the next sections, we will describe the experiments done to tune the classifier and then, we will show the final results.

9.1 Tuning

We consider two systems: the first one models only the three pollen categories, the second one models also the "unknown2" class. For each of these, we have to find:

- number of components in the mixture and structure of their covariance matrix
- initial conditions for random number generator used to initialize EM algorithm
- threshold on probability to decide if an image has to be put in "unknown1" class

When we make the optimization of parameters for pollen categories we consider only the case of spherical or diagonal structure for the covariance matrix because we do not have enough data to estimate all parameters of a MoG with full covariance matrix components. On the other hand, in the optimization of "unknown2" class we only consider full covariance structure and we compute a more complex model for this class because we have available a lot of images and because this class has presumably a statistics quite broad and complex. In other words, it is likely that points belonging to this class "fill" all the feature space and do not gather in a single cluster. Figure 9.2 and Figure 9.3 show the proportional error rate as a function of the number of parameters when you do not model the "unknown2" class and when you do. In the latter case, we changed only the number of Gaussians in the mixture which model the "unknown2" class

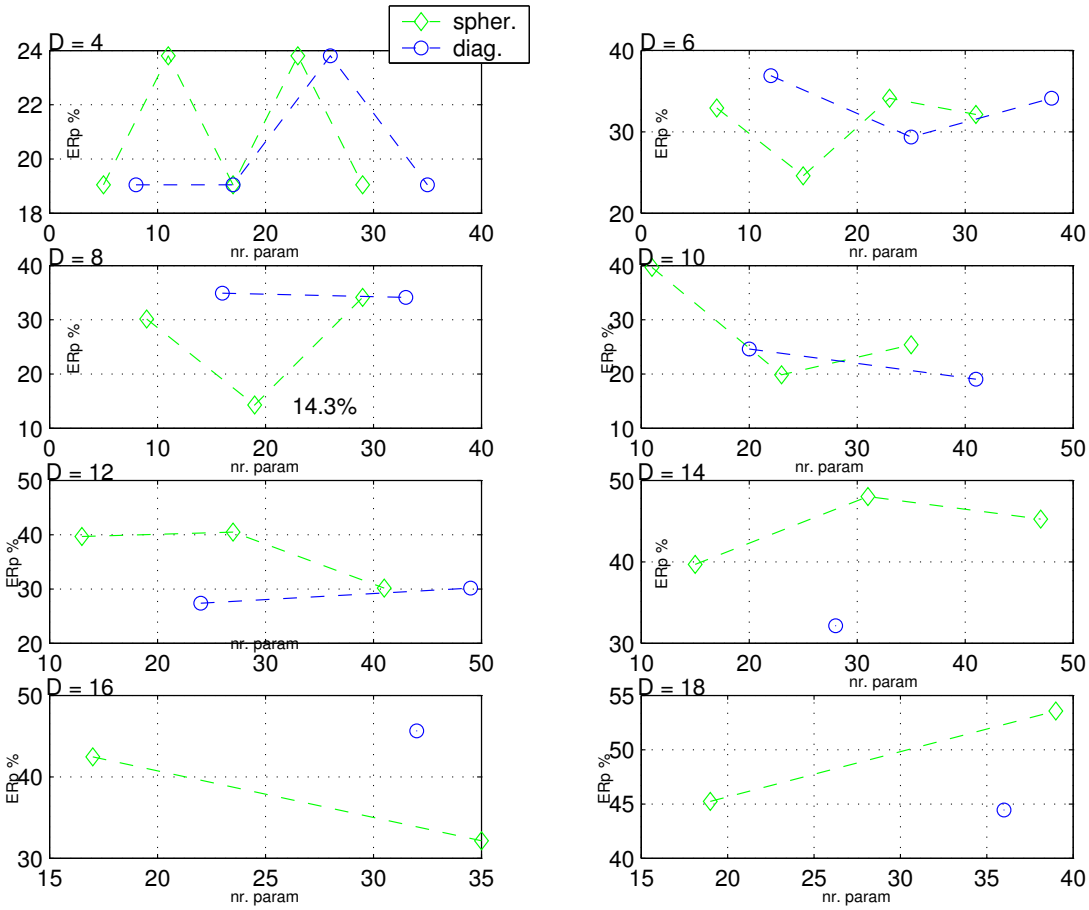

Figure 9.2: Proportional error rate as a function of the number of parameters. The Bayesian classifier using features based on local jets does not model the "unknown2" class.

and the pollen categories are described by mixtures with 2 spherical Gaussians. In Table 9.3, we show the chosen parameters.

Note that throughout this chapter, the proportional error rate is our reference point differently from the previous chapters because of the great difference in the number of test images belonging to different categories. Moreover, we consider that an image belonging to "unknown2" class is correctly classified when it is assigned both to class "unknown1" and, if the model exists, to class "unknown2". Looking at Figure 9.3 and to the absolute error rate here not reported, we observe that increasing the dimensions of feature space causes a better classification for the junk class but a worse classification for the pollen categories. Proportional error rate allows to weight more errors on pollen categories that have less test samples.

Once also the best initial conditions have been found applying the same method described in par. 7.5.1, we are ready to estimate the optimal threshold of probability. With the previous optimal parameters found, we run 10 experiments for each choice of threshold; the error rates shown in Figure 9.4 and Figure 9.5

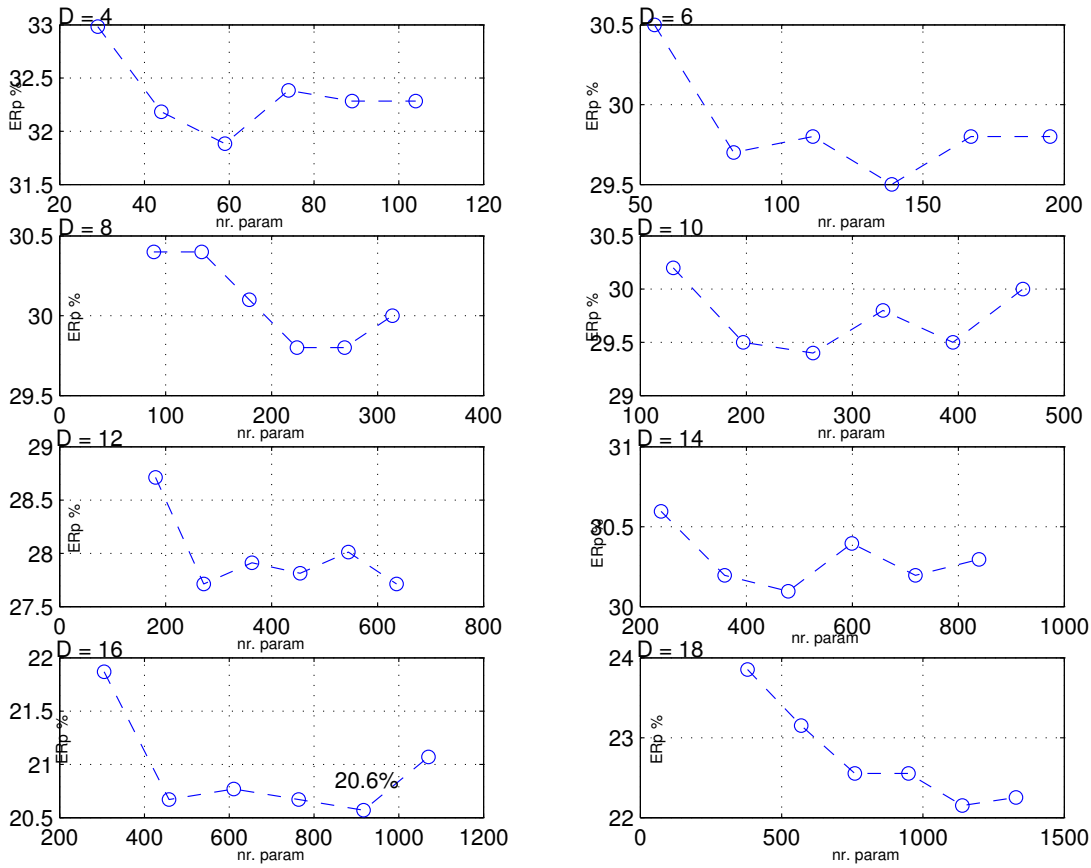

Figure 9.3: Proportional error rate as a function of the number of parameters. The Bayesian classifier using features based on local jets models the "unknown2" class. In these experiments, only the model for this class was changed, namely the number of components in the MoG was varied at each iteration. The pollen classes were modeled with MoG having 2 spherical Gaussians.

are the averaged values. When the system does not model the junk class, the pollen classification is not influenced by the threshold of probability (the blue line is nearly constant) while the junk class is obviously better identified by an high threshold (the red line is strongly related to the classification of this class). Indeed in chapter 8, we noticed that the classifier is most often wrong when the probability assigned to an image is below 90% and on the other hand, correctly classified images have high probability.
Instead, Figure 9.5 shows a behavior more independent from the threshold choice.

From this analysis, we deduce that it is better to model the "unknown2" class. In Figure 9.4, we see that most of junk particles are misclassified while in Figure 9.5 we note that this trend is corrected because the absolute error rate, which mainly depends on junk images, is much less than the proportional error rate. This observation will be confirmed by the final results. Table 9.3 summarize the choice of parameters.

CLASSIF.	DIMENS.	ng_1	$type_1$	ng_2	$type_2$	Thres.
only 3 pollen classes	10	2	spher.	\	\	0.7
3 pollen classes and unk.	16	2	spher.	6	full	0.5

Table 9.3: Parameter chosen for the Bayesian classifier using MoG; the first row is referred to the classifier that does not model junk class. The dimension of feature space, the number of components and their covariance matrix structure is shown for the pollen models (subscript 1) and for the junk class (subscript 2).

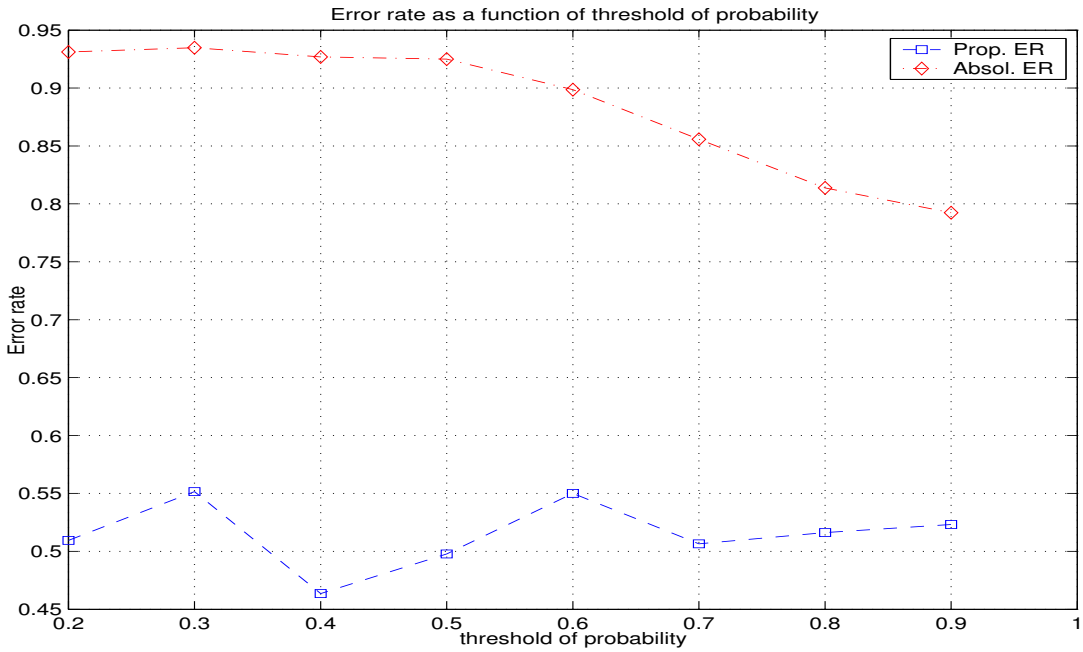

Figure 9.4: Error rate as a function of the threshold on probability. Plot referred to classifier which does not model junk class.

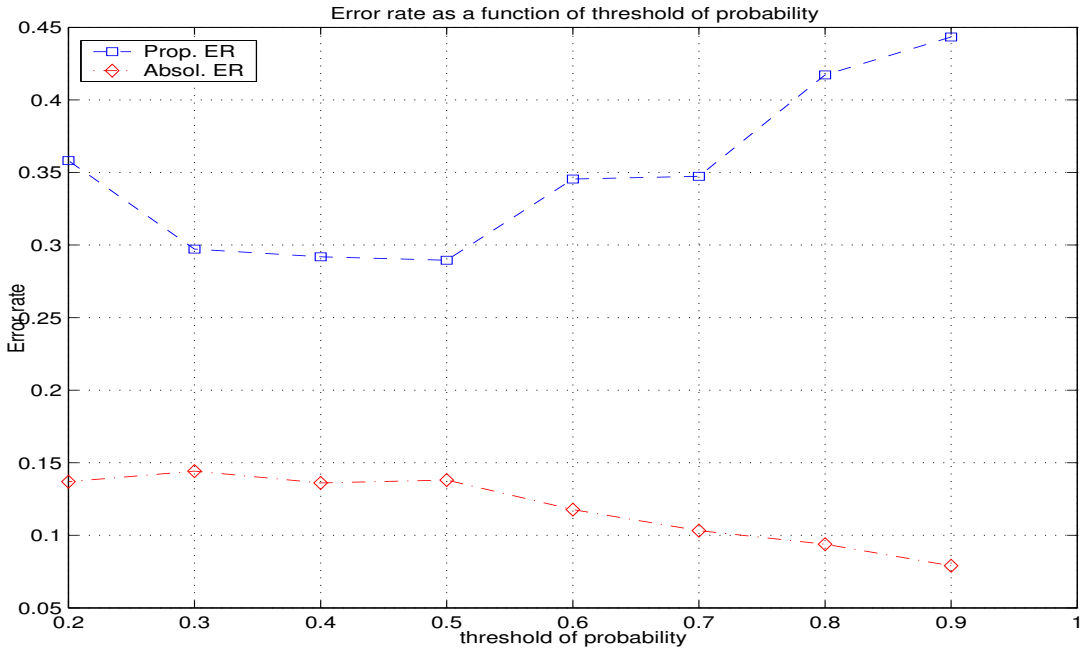

Figure 9.5: Error rate as a function of the threshold on probability. Plot referred to classifier which models junk class.

9.2 Final Experiments

Because of the shortage of images in our database, we could not divide it in training, validation and test sets. Each time we took randomly 10% of images for test and the rest for training. In order to evaluate the performance of the system, we made an average of the results of 100 experiments. The confusion matrices are shown in Figure 9.6 and Figure 9.7.

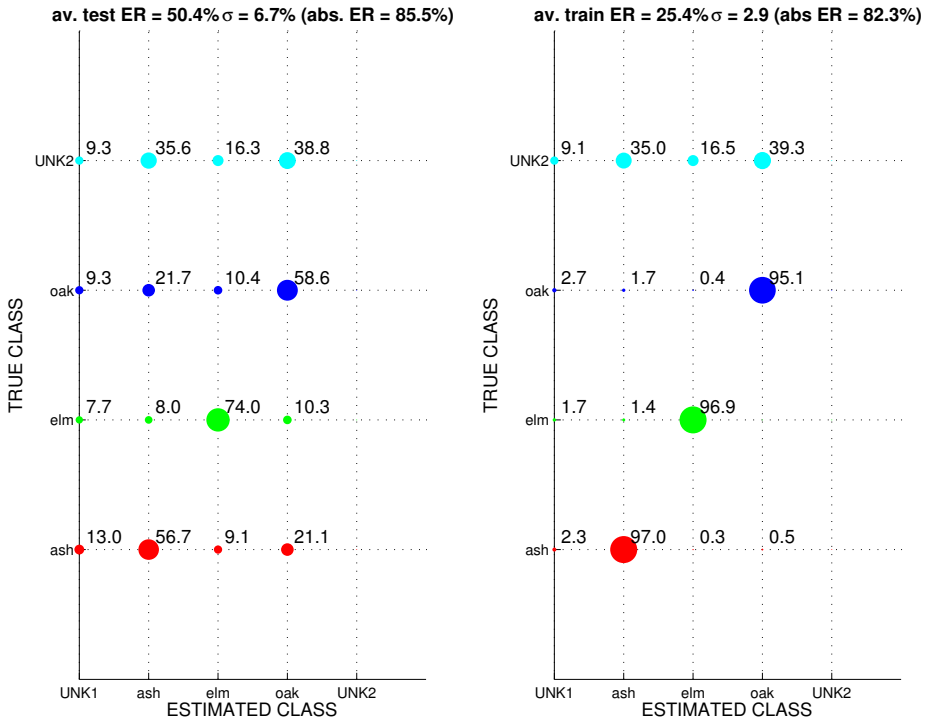

Figure 9.6: Test and training confusion matrix, left and right respectively. The classifier does not model the junk class. Note that almost all junk particles are classified as pollen.

The performance of the system which models the junk class is much better. In this system, most of false alarms fall in either "unknown1" or "unknown2" classes. Note that the error rate has about the same value of the error rate found in par. 7.5.2 when we tested on air sampled pollen grains with patches selected by the human expert and without the false alarm class. This is possible because our detector is able to do a segmentation comparable to the expert's one and we have a good model for the false alarm category.

The variance of the error rate is quite high, around 7%. For example in the experiments of Figure 9.7, the minimum error rate was about 12% while the maximum 48%. This should be interpreted as a lack of reliability of our result because of the shortage of images used in test and in training.

You should note also the gap between training and test error rate. This means that we are using too few images for training and we are overfitting the training

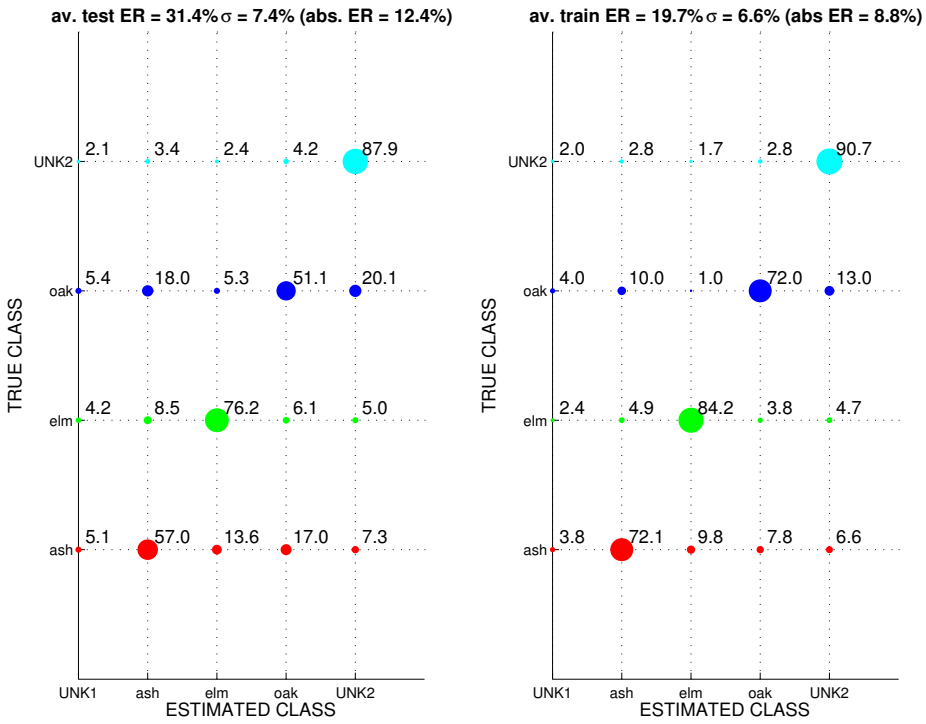

Figure 9.7: Test and training confusion matrix, left and right respectively. The classifier models the "unknown2" class.

data. On the other hand, we are confident that using more images for training this gap will decrease until nearly zero and the final performance will be around or below 10% as predicted by the reasoning done for Figure 7.28.

9.3 Conclusion

In this chapter it was described the performance of the whole system on images of pollen captured by spore trap. The detector is able to detect with probability of 9/10 all pollen grains but it detects also for each pollen ten other particles. With the spatial resolution of our images this result is quite good.

The next stage is classification. When the system learns to classify using few images for training and it models also the junk class the error rate is about 30%. This result confirms the performance of the same classifier when the expert's patches were used thus, we deduce that the automatic segmentation is really good. Moreover, this time we deal also with the false alarm class but thanks to a more complex model, we achieve on this category the best correct classification rate: nearly 90%.

Looking at the training error rate and to the estimate done in Figure 7.28, we are confident that this system will be able to achieve an error rate of 10% when it will be fed with more images because we will be able to estimate more complex models and the system will have a better generalization of training data.

The experiments are done in conditions which are very close to a real situation. Particularly, we keep the ratio between pollen and junk particles at one out of ten and the classifier receives objects in the right proportion. In this way, we overcome the difficulty to select images for training and to classify pollen particles that are not modeled because their number is too low.

To give an idea of the current performance we now give an example. Suppose the system receives 50 images with 100 pollen grains. Then 90 of them will be detected and 1000 false alarms will be generated. The classifier receives 1090 patches and will correctly identify nearly 70% of pollen particles. This means that at the end 63 pollen grains will be correctly recognized by our system.

Chapter 10

Conclusion

In this thesis, it was discussed a system for visual recognition of biological particles. Our interest is justified by the need to automatically do microscopic analysis. This is because manual analysis is slow, expensive, not precise and not standardized. We worked on two databases: the first one is a collection of particles in urine, the second one is a collection of sticky tape images containing many genera of pollen.

The recognition system can be divided into two stages: detection and classification. Detection aims to find points of interest in an image, in which it exhists at least a small probability of a useful particle presence represented by those spots. Classification receives patches from the detector; particularly, it has to skip particles that are not of interest and for the rest to determine their category.

We developed a detector based on morphological operations which gave very good results on pollen database. It is able to detect with probability 9/10 the 23 species of pollen in sticky tape pictures taken by light microscope. The percentage of false alarm is about 1000%. Looking at the images in our database, this performance seems very good. Even an expert has to focus his attention on nearly 10 points in each image to establish the presence of a pollen. On the other hand, this approach is not general and reprogramming is needed to apply this detector to another database. Furthermore, this technique is quite slow compared to other ones based on filtering, the analysis of one image takes up 10 seconds on a current 2.5GHz Pentium processor computer.

The simplest classifier with the best performance is the Bayesian classifier using mixture of Gaussians to model the training data. We developed a new kind of features based on local jets [9]; these features prove to capture almost all the essence of input images because we were able to achieve an error rate of about 7.6% on urine database and 10% on 6 kinds of "pure" pollen. This approach is interesting because it is segmentation free, very general and able to handle very low contrast particles.

On the other hand, the system could be further improved using more complex technique, which extracts from points in foreground information about texture, shape and color.

Moreover in a real application, the system often has to handle particles that are

not of interests, for example in pollen recognition most of the patches contain junk particles. This class should be very well classified if we admit an high number of false alarms in detection. This is a challange to consider in the design of a good classifier, and in our experiments we took into account this class when we considered the pollen classification task.

Our contribution in classification of urine particles relies on the definition of a new set of powerful features that are able to extract information from patches of about 60x60 pixels without any segmentation. Thanks to the simplicity of our system, we are able to classify very quickly particles; nearly 10ms are required to analyze a particle on a current 2.5GHz Pentium processor computer.

In pollen recognition, our work is the first research towards a feseable system for real-time pollen count in which detection and classification are combined to recognize several kinds of pollen.
We used images taken with a common light microscope and our database is built using the common equipment for pollen collection, namely the volumetric spore trap. Unfortunately, the collection of airborne pollen grains is very slow and the available database is still very small. This makes not very reliable our results and poor our performance. A larger database would allow a better modeling of data and improve our performance. However, the first results showed throughout this work seem very promising. We proved experimentally the importance to use pollen particles captured by spore trap instead of "pure" pollen grains, that is pollen grains taken directly from flowers. Indeed, the former ones are much more variable in size, shape and texture.

In our opinion, urinalysis could be improved in the future if a general and segmentation free approach is applied, and if we reserve customized operations only in a second stage for the most difficult samples.
Pollen recognition needs further research but several steps have been made in the right direction. We think that in the next months a new software could be written based on this work to detect pollen particles and make hypothesis of classification. This should be a tool to help experts, who are building their current database and speed-up the process of labelling. It is reasonable to foresee that in the next few years a completely autonomous system for automatic and reliable recognition of pollen could be built using as input the sticky slides of volumetric spore trap. In the future, a new kind of collection technique able to produce input images with less debris is also possible, and will certainly improve the performance of the visual recognition system. This will yield to a real-time and low cost measurement instrument for pollen count which will definitely make easier and better the life of many allergic people.

Bibliography

[1] http://www.aaaai.org.

[2] http://medlib.med.utah.edu/WebPath/TUTORIAL/URINE/.

[3] http://web.engr.oregonstate.edu/ tgd/software/ecoc-codes.tar.gz.

[4] http://www.cis.tugraz.at/igi/aschwaig/software.html.

[5] The iq200 automated urinalysis system. Brochure IRIS.

[6] C.M. Bishop. *Neural Networks for Pattern Recognition.* Oxford Univ. Press, 2000.

[7] C.J.C. Burges. A tutorial on support vector machines for pattern recognition. *Data Mining and Knowledge Discovery*, 2(2):121–167, 1998.

[8] M.C. Burl, L. Asker, P. Smith, U. Fayyad, P. Perona, L. Crumpler and J. Aubele. Learning to recognize volcanoes on venus. In *Machine Learning*, volume 30, pp. 165–194, Boston, Feb-Mar 1998. Kluver Academic Publisher.

[9] R. Mohr C. Schmid. Local grayvalue invariants for image retrieval. *IEEE Trans. on Pattern Analysis and Machine Intelligence*, (19(5)):530–535, 1997.

[10] N. Cristianini and J. Shawe-Taylor. *Support vector machines and other kernel-based learning methods.* Cambridge University Press, 2000.

[11] J. Dahmen, J. Hektor, R. Perrey and H. Ney. Automatic classification of red blood cells using gaussian mixture densities. In *Proc. Bildverarbeitung für die Medizin*, pp. 331–335, Munich, Germany, 2000.

[12] T.G. Dietterich and G. Bakiri. Solving multiclass learning problems via error-correcting output codes. *Journal of artificial intelligence research*, 1995.

[13] R.O. Duda and P.E. Hart. *Pattern classification and scene analysis.* Wiley, New York, 1973.

[14] I. France, A.W.G. Duller, H.F. Lamb and G.A.T. Duller. A comparative study of approaches to automatic pollen identification. BMCV, 1997.

[15] Y. Freund and R.E. Schapire. A decision-theoretic generalization of on-line learning and an application to boosting. In *European Conference on Computational Learning Theory*, 1996.

[16] K. Fukunaga. *Introduction to Statistical Pattern Recognition.* Academic Press, second edition, 1990.

[17] J.J. Koenderink and J. van Doorn. Representation of local geometry in the visual system. *Biological Cybernetics*, (55):367–375, 1987.

[18] M. Langford. *Some applications of digital image processing for automation in palynology.* Ph. D. Thesis, University of Hull, 1988.

[19] M. Langford, G.E. Taylor and J.R. Flenley. The application of texture analysis for automated pollen identification. Conference on identification and pattern recognition, 1986.

[20] D.G. Lowe. Object recognition from local scale-invariant features. In *International conference on computer vision*, Corfù, Sept. 1999.

[21] D.G. Lowe. Distinctive image features from scale-invariants keypoints. submitted for pubblication, June 2003.

[22] J.R. Flenley M. Langford, G.E. Taylor. Computerised identification of pollen grains by texture. *Review of paleibotany and palynology*, 1990.

[23] P. Perona. Note on fisher linear discriminants, 2000.

[24] O. Ronneberger, U. Heimann, E. Schultz, V. Dietze, H. Burkhardt and R. Gehrig. Automated pollen recognition using gray scale invariants on 3d volume image data. Vienna, Austria, Sept 2000. Second European Symposium on Aerobiology.

[25] R.E. Schapire. Using output codes to boost multiclass learning problems. In *Machine Learning: Proceedings of the Fourteenth Conference*, 1997.

[26] R.E. Schapire. The boosting approach to machine learning an overview. In *MSRI workshop on nonlinear estimation and classification*, 2002.

[27] E. Grant Smith. *Sampling and identifying allergenic pollens and molds.* Blewstone Press, San Antonio, Texas, 2000.

[28] A. Torralba and A. Oliva. Statistics of natural image categories. *Network: Computation in neural systems*, (14):391–412, 2003.

[29] E.L. Vezey and J.J. Skvarla. Computerised feature analysis of exine sculpture patterns. *Review of paleibotany and palynology*, 1990.